Graduate School of Technology and Science

Utilization of kenaf fibers as a flexible support for indium zinc oxide thin films and as a sacrificial template of nanostructured tubular TiO2 through dip-coating method

Edynoor bin Osman

Doctor of Philosophy

2018

UTILIZATION OF KENAF FIBRES AS A FLEXIBLE SUPPORT FOR INDIUM ZINC OXIDE THIN FILMS AND AS A SACRIFICIAL TEMPLATE OF NANOSTRUCTURED TUBULAR TIO_2 THROUGH DIP-COATING METHOD

EDYNOOR BIN OSMAN

A thesis submitted

in fulfillment of the requirements for the degree of Doctor of Philosophy

Department of Chemical Science and Technology
Graduate School of Technology and Science

TOKUSHIMA UNIVERSITY

2018

DECLARATION

I declare that this thesis entitled "Utilization of kenaf fibres as a flexible support for indium zinc oxide thin films and as a sacrificial template of nanostructured tubular TiO_2 through dip-coating method" is the results of my own research except as cited in the references. The thesis has not been accepted for any degree and is not concurrently submitted in candidate of any other degree.

Signature : ……

Name : Edynoor bin Osman

Date : 7 September 2018

APPROVAL

I hereby declare that I have read this thesis and in my opinion this thesis is sufficient in terms of scope and quality for the award of Doctor of Philosophy.

Signature	: ……..……
Supervisor Name	: Prof Toshihiro Moriga
Date	: 7 September 2018

ABSTRACT

The novelty of this study is the investigation of the electrical conductivity of the indium zinc oxide-modified kenaf fibre (KF-IZO) with emphasis on its morphology and the dipping rate as required for dip-coating and annealing process applications. The KF was alkalized using a 5% solution of sodium hydroxide (NaOH) whereas the dipping rate was varied from 1 to 30 mm/s. Next, the KF-IZO was annealed at 150, 175 and 200 °C for 2, 4, 6, and 8 hours. A modified four-probe method employing a copper metal attachment plate was used to evaluate the electrical properties of KF-IZO. A dipping rate of 5 mm/s at 150 °C annealed temperature, which yielded the highest electrical conductivity of 11.81 S/mm, was the observed optimum. Furthermore, the electrical resistivity of KF-IZO at 4 hours of annealing time showed the lowest resistivity of 0.12 Ω.mm. However, the highest resistivity of 12.62 Ω.mm was obtained at 16 hours of annealing time. Scanning Electron Microscope/Energy Dispersive X-Ray (SEM-EDX) analysis of KF-IZO revealed the IZO film was uniformly coated on the KF substrates without significant thermal damage. KF-IZO showed potential for application in smart textiles, electrostatic discharge protection, and as reinforcement in composites. The second novelty of this study was the production of tubular TiO_2 using kenaf natural fibre as a sacrificial template. The tubular TiO_2 nanostructures were synthesised in a single step by depositing titanium (IV) isopropoxide precursor on kenaf fibres. In the calcination temperature range 500–700 °C, the synthesized tubular TiO_2 predominantly contained the anatase phase. X-ray diffraction studies were performed to examine the crystallinity and crystallite size of the tubular TiO_2 synthesized while its photocatalytic activity was examined by monitoring the degradation of methylene blue (MB) under ultraviolet irradiation. The results showed that tubular TiO_2 formed at 500 °C exhibited the smallest crystallite size of 9.27 nm and fastest photocatalytic oxidation rate. In summary, KFs can serve as an effective, abundant, and inexpensive template material for the synthesis of nanostructured tubular TiO_2 with a high surface area.

ACKNOWLEDGEMENT

First, praises and thanks to Allah S.W.T, for giving me infinite grace and blessings throughout my journey of study. Generously would like to take this opportunity to express my heartfelt appreciation and thanks to my principal supervisor, Professor Dr. Toshihiro Moriga for his continuing guidance, encouragement, supervision, advice and effort throughout the study. I would like to thank, Associate Professor Dr. Kei-ichiro Murai for his thoughtful, assistance and knowledge with the testing and analysis done in this study. Not to forget Associate Professor Dr. Mohd Warikh for his support and constructive feedbacks during the study. I also thank all the students at C1 and C2 Chemical Laboratory (Ikenaga, Minakata, Koji, Faiz, Masaru, Takeuchi, Narendra and others), Department of Chemical Science and Technology, Tokushima University for their kind-heartedness and helpful.

Special thanks to Associate Professor Dr. Toshihide Horikawa for BET analysis and Ueki-san as technical staff for FIB and SEM-EDX analysis. In addition, I am thankful to Dr. Mohd Edeerozey for his assistance for the journal published.

Sincere thanks to all involve in this study direct or indirectly in assistance me for conducting the experimental work. For my wife (Hazlinda), sons (Muhammad Daniel Haikal and Muhammad Daffy Danish), daughter (Nourish Zara Aleesya) and all family members, no amount of gratitude could reply your kindness of being there as well as the patience to put with my whim. My deepest gratitude in meant for all of you. Last but not least, the financial support by Majlis Amanah Rakyat (MARA) is hereby acknowledged.

TABLE OF CONTENTS

LIST OF TABLES

LIST OF FIGURES

LIST OF ABBREVIATIONS

TCO	-	Transparent Conducting Oxide
KF	-	Kenaf Fibre
XRF	-	X-Ray Fluorescent
IZO	-	Indium Zinc Oxide
KF-IZO	-	Indium Zinc Oxide modified Kenaf Fibre
XRD	-	X-Ray Diffraction
SEM/EDX	-	Scanning Electron Microscope/Energy Dispersive Using X-Ray
TGA	-	Thermogravimetric Analysis
BET	-	Brunauer–Emmett–Teller
ESD	-	Electrostatic Discharge
EMI	-	Electromagnetic
EDS	-	Energy dispersive spectroscopy
WDS	-	Wavelength dispersive spectroscopy
DSSC	-	Dyed-synthesized solar cell
TTIP	-	Titanium (IV) Isopropoxide
MB	-	methylene blue
UV	-	ultraviolet
FIB	-	Focused Ioned Beam
C	-	Carbon
O	-	Oxygen
Ti	-	Titanium
In	-	Indium
Zn	-	Zinc
Cl	-	Chlorine

LIST OF SYMBOLS

$Å^2$	-	angstrom
N_2	-	Nitrogen
K	-	Kelvin
S	-	Siemens
Ω	-	ohm
B	-	full width at half maximum (FWHM)
k	-	constant equal to 0.94
λ	-	wavelength of X-ray radiation (Cu Kα = 0.15406 nm)
s	-	crystallite size
θ	-	diffraction angle
g	-	grams
C_o	-	initial concentration of MB, and
C	-	concentration of MB after irradiation
psi	-	pounds per square inch
ρ	-	Resistivity
σ	-	Conductivity
R	-	Electrical resistance (ohm)
L	-	Length of the sample (mm)
A	-	Cross-sectional area of the sample (mm^2)

LIST OF PUBLICATIONS

Journals

[1] "Study of morphology and electrical properties of indium zinc oxide-modified kenaf fibre"

Edynoor bin Osman, Toshihiro Moriga, Kei-ichiro Murai, Mohd Warikh bin Abd Rashid, *Journal of Industrial Crops and Product*, 100, Page 171–175, 2017, Published

[2] "Photocatalytic activity of nanostructured tubular TiO2 synthesized using kenaf fibres as a sacrificial template"

Edynoor bin Osman, Toshihiro Moriga, Kei-ichiro Murai, Mohd Warikh bin Abd Rashid, Mohd Edeerozey Abd Manaf, Toshihide Horikawa *Journal of Industrial Crops and Product*, 113, Page 210–216,2018, Published

[3] "Effect of annealing time on resistivity of kenaf fibre modified indium zinc oxide prepared via dip coating process"

O. Edynoor, A.R.M. Warikh, T, Moriga, K. Murai, E. Mohammad and M.R. Salleh *Journal of Advanced Manufacturing Technology (JAMT)(Special issue (TMAC) Symposium 2017)* Page 139-150, Published

[4] "Transparent coating oxide – indium zinc oxide as conductive coating: A review"

O. Edynoor, A.R.M.Warikh, T. Moriga, K. Murai and M.E.A. Manaf *Rev.Adv. Mater. Sci. (Reviews on advanced materials science)* 49, Page 150 – 157, Published

[5] "Hygrothermal effect on mechanical and thermal properties of filament wound hybrid composite"

Osman, E., Rashid, M.W.A., Manaf, M.E.E., Mohamad, E., Salleh, M.R., Ito, T. and Moriga, T., 2016. *Journal of Advanced Manufacturing Technology* (JAMT), pp.1-12

Proceedings

[1] "Effect of Annealing Temperature towards Electrical Properties of Indium Zinc Oxide Modified Kenaf Fibre through Dip-coating Method"

O.Edynoor, T. Moriga, K. Murai, A.R.M. Warikh, *Proceedings of Mechanical Engineering Research Day 2017*, pp. 375-376, March 2017, Indexed in Goggle Scholar, Published.

[2] "Photocatalytic activity of titania modified kenaf fibre as methylene blue purification process**"**

O. Edynoor, T. Moriga, K. Murai, A.R.M. Warikh

Proceedings of Innovative Research and Industrial Dialogue'16, pp. 109-110 (May 2017), Published. *(**Best Poster Award**)

CHAPTER 1

INTRODUCTION

1.1 Background of the study

The demand for natural resources has tremendously evolved as researchers seek for commercial applications. Recently, researchers have become concerned about the development of natural fibres for industrial applications in composite materials and coating technology. As such, the focus has been on developments in cost efficiency, eco-friendliness, renewability and ease of the manufacturing process. Among the many different types of natural resources, kenaf plants have been extensively exploited by researchers. Kenaf fibres are attractive natural resources with good mechanical and physical properties that can be cultivated in abundant quantities. The manufacturing applications of kenaf fibres include high-performance materials such as automobile parts. In this study, the kenaf fibres are developed as functionally driven flexible support and sacrificial template for industrial applications such as conductive materials.

1.2 Problem statements

In recent years, transparent conducting oxides (TCO) have been successfully applied as conductive materials in various industries as electronics and semiconductors. Earlier, glass, sapphire and polymer materials were substrates used for TCO. However, there is no available data on the development or utilization of natural fibres for TCO despite its environmental friendliness, reproducibility, and economic advantages. The

drawbacks of natural fibres include low degradation temperatures (~200 °C) which limit processing at high temperatures (Sgriccia et al., 2008). However, the modification of natural fibres with TCO improves its suitability for materials applications in electrostatic (charge) dissipation and bio-composite reinforcements, which require mechanical integrity and biocompatibility. Therefore, the low processing of TCO with natural fibres is selected for consideration as composite or hybrid materials. One of the most recognized TCO that can be processed at low temperature is indium zinc oxide (IZO). In practice, indium is used as a dopant material in IZO, instead of titanium. Moreover, IZO is one of the best materials due to its low resistivity, high mobility, and good transparency in the visible range (Lee and Park, 2003; Dehuff et al., 2005; Craciun et al., 2014). However, the use of indium as a dopant material has drawbacks such as high costs, scarcity, and low usability (Ellmer, 2012). Therefore, the transparent coated oxide-indium zinc oxide (TCO-IZO) modified with kenaf fibre enhances the usability of kenaf fibre. Besides, the commercial use of TiO_2 as a photocatalyst is becoming widespread in the areas of water purification, air purification, and sterilisation/disinfection.

Other areas include systems involving applications of the recently reported superhydrophilic effect (Bozzi et al., 2005). One such application involves using TiO_2 as a photocatalytically active material with properties that can be triggered by light irradiation. Due to its low cost, non-toxicity, and high stability, TiO_2 has many advantages over other photocatalytic materials (Chen and Mao, 2007). According to previous studies (Macwan et al., 2011; Behnajady et al., 2011; Bagheri et al., 2013), the sol-gel method is the most common technique for the synthesis of TiO_2 photocatalyst. This is because it facilitates the synthesis of nanosized crystallized TiO_2 powder with high purity at relatively low temperatures.

In the last two decades, considerable efforts have been spent on the development of suitable synthetic strategies for nanomaterials with controlled shapes, sizes, compositions, and latitudinal arrangements. Template-assisted synthesis is a widely effective technique for achieving a relatively high degree of control over the reaction parameters. This approach has many advantages over the syntheses conducted without a template. Various studies have been performed to identify available, environmentally friendly, and cost-effective templates for the efficient synthesis of nanomaterials (Liu et al., 2013). Although some studies have identified nanostructured TiO_2 materials, the use of natural resources like kenaf fibres as a sacrificial template is non-existent in literature. This study will emphasise kenaf fibre as a sacrificial template to synthesize high surface area nanostructured tubular TiO_2. This will replicate the fibre shape (hollow tubes) and its effect on the performance of a photocatalytic activity under UV light using methylene blue (MB) dyes.

1.3 Objectives of the study

i. To synthesize indium zinc oxide-modified kenaf fibre (KF-IZO) by dip-coating.

ii. To investigate the electrical properties and morphology of the synthesized KF-IZO.

iii. To synthesize high surface area nanostructured tubular TiO_2 using kenaf fibre as sacrificial templates.

iv. To characterise the tubular TiO_2 and its photocatalytic activities under visible light.

1.4 Scope of the study

Firstly, the potential of kenaf fibre as flexible support for indium zinc oxide thin films that conduct electrical charge was concealed. Therefore, the study of the morphology and electrical properties of KF-IZO was conducted. Initially, the kenaf fibre was processed by alkalization and material characterisation through thermogravimetric analysis (TGA) to determine the criterion of the fibre. Next, the IZO precursor solution was prepared for the dip coating process. The coating synthesis of KF-IZO was conducted by dip-coating. The investigation of the properties and morphology of KF-IZO was conducted. The parameters examined in the study are dipping rate and annealing process (temperature and time) towards its electrical properties (conductivity and resistivity). The electrical properties of KF-IZO were measured by a four-probe method using a copper metal attachment plate. A focused ion beam was used to cut the KF cross-section, which was scanned by Scanning Electron Microscope/Energy Dispersive X-Ray (SEM/EDX) for qualitative measurements.

Secondly, additional promising applications of synthesised high surface area nanostructured TiO_2 using kenaf fibre include sacrificial templates. The TiO_2 precursor solution was prepared through the sol-gel method. To perform TiO_2 coating, a KF mat was dipped in the precursor solution before pressing at an applied force. Next, the treated KF mat was dried followed by stepwise heating to remove residual kenaf fibres completely. Therefore, the study parameters are the calcination temperatures; 500, 600, 700, and 1000 °C. The resultant tubular TiO_2 were further characterized by XRF, TGA, SEM–EDX, XRD and Brunauer–Emmett–Teller (BET) analysis techniques. As for the tubular TiO_2 performance test, photocatalytic activity has been tested for the purification of methylene blue (MB) dyes.

1.5 Motivation of the study

The study on the utilisation of kenaf fibres as a flexible support and sacrificial templates for the synthesis of high surface area nanostructured TiO_2 presents novel avenues for industrial applications. It will also offer an easy, alternative, and economical processes for production. It is well known that kenaf fibres possess good mechanical strength and high flexibility. Therefore, KF is suitable flexible support for an electroconductive thin film with high electroconductivity. Furthermore, KF is carbon neutral under air combustion. Non-woven kenaf possesses uniform diameters of several micrometres wide. Therefore, it is considered a sacrificial template for nanostructured tubular materials. The dip-coating method was applied to form the surrounding structure around the kenaf fibres and control its crystallinity. Other benefits of applying the dip-coating method are low-temperature control which is suited with the material properties of kenaf fibres.

Firstly, a study of the morphology and electrical properties of KF-IZO provides information and ideas for coating IZO on kenaf fibre surfaces through dip coating. In general, amorphous IZO exhibits good conductivity for low-temperature processing. Hence, it can be attached on the kenaf fibre as a thin film coating. Furthermore, the KF-IZO can be applied to eliminate electrostatic charge and other products that require electrical conductivity. Other applications of KF-IZO include; smart textile, composite technology (such as EMI shielding, as reinforcement material in composite technology), bioelectronic electromagnetic and electrostatic discharge (ESD) protection.

Secondly, the photocatalytic activity of nanostructured tubular TiO_2 synthesised with kenaf fibres as a sacrificial template is a remarkable discovery in nanomaterials technology. It offers environmentally friendly, cost-effective, and abundant templates for the efficient synthesis of tubular nano-wall tube materials. As a result, synthesized tubular

TiO_2 has applications in high hydrophilic environments for moisture reduction. Lastly, the high surface area of TiO_2 tubes can accelerate the process of photocatalysis

1.6 Thesis outline

Chapter 2 presents a comprehensive literature review relevant to the study. It is based on three (3) major issues including; kenaf fibre, transparent conducting oxides (TCO), and lastly, TiO_2 and its photocatalytic activity. The first part reviews the kenaf fibre (KF) as a natural resource and its background, application, fibres properties and chemical treatment. Secondly, the concept of transparent conducting oxide (TCO) with the zinc oxide material was explained. The deposition techniques, coating parameters and its properties were further elucidated. Thirdly, the background and properties of TiO_2, template synthesis of nanostructured materials, a sol-gel technique in addition to the photocatalytic activity and its mechanism were also reviewed and explained.

Chapter 3 describes the detailed methods, processes, testing and analyses involved in this study. The preparation of indium zinc oxide (IZO) and TiO_2 solutions was described in detail. The prepared solution, IZO and TiO_2 were used to synthesize KF coated IZO, and KF coated TiO_2 (KF acts as a sacrificial template for tubular TiO_2) via dip-coating method. For the KF-IZO, different dipping rates and annealing processes were further examined to investigate the effect of the IZO thin film attached on KFs. Next, the surface morphology of KF-IZO was analysed to examine the coating condition and reveal any imperfections. Furthermore, electrical property tests were performed to reveal the function, conductivity, and resistivity properties of IZO thin films with KF. Meanwhile, tubular TiO_2 which replicated the fibre shape of KF at different calcination temperatures was further analysed and tested. The surface morphology of TiO_2 tubes was analysed to examine its effect on photocatalytic activity.

Chapter 4 reports and discusses the study of KF-IZO. Firstly, the effectiveness of alkalization towards KF was revealed. The surface morphology of KF-IZO was discussed at different dipping rates and annealing process parameters (temperature and time). The four-probe method with line contact attachment (copper metal plate) was used to determine the electrical properties of KF-IZO. Lastly, the efficacy and performance of KF-IZO were revealed.

Chapter 5 discusses the decomposition and degradation of KF coated TiO_2 by thermal analysis. The surface morphology analyses including point area and elemental mapping were reported for the determination of tubular TiO_2. Furthermore, the XRD and BET analyses were also reported to reveal the characteristics of tubular TiO_2. Lastly, the photocatalytic activity of tubular TiO_2 on methylene blue (MB) under UV light was explained and discussed.

Chapter 6 summarises the results of the study. Furthermore, the conclusions and future recommendations for future improvements related to the current study were presented.

CHAPTER 2

LITERATURE STUDY

2.1 Introduction

In this chapter, the background, properties, and applications of kenaf natural fibres are presented. Next, two (2) issues related to kenaf utilisation are concisely elaborated. The first issue is the transparent coating oxide-indium zinc oxide (TCO-IZO) and related topics. The second issue is the photocatalytic activities of high surface area TiO_2 and related topics.

2.2 Natural fibres

In theory, natural fibres are classified according to their origin namely; plants, animals, or minerals. For plant fibres (lignocellulosic), it is composed of cellulose, hemicellulose, and lignin along with minor amounts of pectin, waxes, and water-soluble substances (Gassan and Bledzki, 1999). Recently, natural fibres have attracted significant attention in manufacturing industries from the viewpoint of sustainability and environment issues. Hence, natural fibres like kenaf, jute, sisal, hemp, and bamboo are widely used in the manufacturing industries. Like wood and bamboo, kenaf is a traditional third-world crop which is now poised for introduction as a new, annually, renewable resource for industrial purposes (Khalil et al., 2010).

2.2.1 Kenaf fibre background

Kenaf (*Hibiscus cannabinus*) is a plant in the *Malvaceae* family also called Deccan hemp or Java jute. *Hibiscus cannabinus* is in the genus Hibiscus which is native to southern Asia, although its exact origin is unknown. The name also applies to the fibre obtained from this plant. Furthermore, kenaf is one of the allied fibres of jute and shows similar characteristics. Kenaf plants have been extensively used (compared to other natural resources) due to their low cost and rapid ability to grow under various climatic conditions (Aziz and Ansell, 2004; Ramesh, 2016). The plant can grow to a height of 2.4 m – 6 m at an average of 150 days (Mohanty et al., 2005; Ashori et al., 2006). Kenaf has advantages as regards to its resistance to extreme climates, pests or diseases (Holbery and Houston, 2006). An attractive feature of kenaf is that up to 40% of the stalk yields usable fibre, roughly twice that of jute, hemp, or flax, which makes the fibre very economical.

The kenaf plant possesses three basic useful components. These components are the seed, leaf, and stem (Webber III and Bledsoe, 2002). The derivatives of these components include; fibre strands, proteins, oils, and allelopathic chemicals. Figure 2.1 presents a photograph of the kenaf plant, stem and fibre (Babatunde et al., 2015). In theory, kenaf fibre is comprised of the bast (outer) and core (inner) fibres of the kenaf plant. Some researchers reported that the chemical composition of kenaf fibres consists of cellulose (56–64 wt. %), hemicellulose (21–35 wt. %), lignin (8–14 wt. %) and small amounts of extracts and ash (Mazuki et al., 2011; Davoodi et al., 2010).

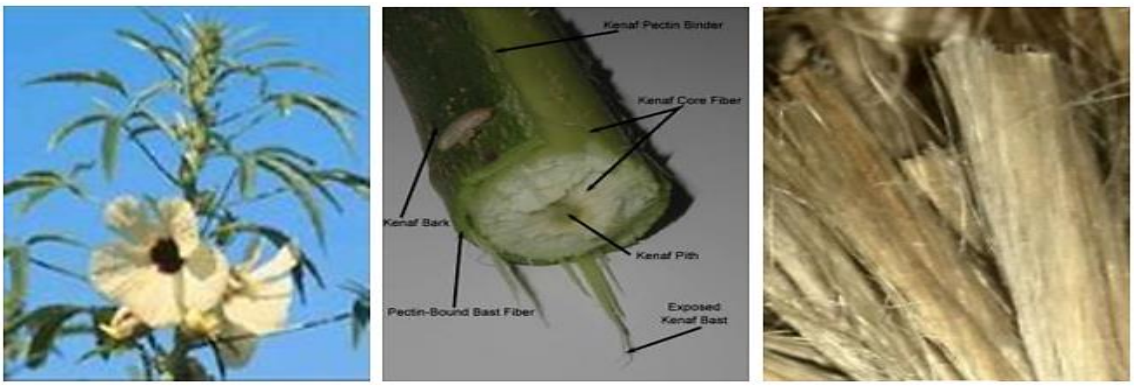

Figure 2.1: (a) Kenaf plant (b) Cross section of kenaf plant stem (c) kenaf fibre (Babatunde et al., 2015).

2.2.2 Kenaf fibre properties

Kenaf fibre is a cheap, low-density material that possesses good mechanical properties and recyclability (Raman et al., 2015; Mohanty et al., 2000). Kenaf bast fibre reportedly has superior flexural strength combined with excellent tensile strength that makes it the material of choice for a wide range of extruded, moulded, and non-woven products (Aji et al., 2009). Table 2.1 presented some compiled properties of kenaf fibre from different sources.

Table 2.1: Some compiled properties of kenaf fibre.

Density (g/m^3)	**Tensile Strength (MPa)**	**Tensile Modulus (GPa)**	**Elongation (%)**	**Source**
1.45	930	53	1.6	Akil et al., 2011; Mahjoub et al., 2014
1.50	300-600	40	2.5-3.5	Cheung et al., 2009

2.2.3 Applications of kenaf fibre

There are currently various novel applications of kenaf including paper products, building materials, absorbents and animal feeds. Other applications explored to utilise kenaf fibre include insulation boards and reinforcement in polymer composites (Ramesh, 2016). Nishino et al. (2003) revealed the mechanical strength and thermal properties of kenaf composite are superior to other natural fibre composites which are suitable for high-performance applications. Hence, kenaf composites can eventually supplement or substitute petroleum-based composite materials in many industrial applications. This presents significant prospects for innovative environmental, agricultural, manufacturing formulation methods which enhance consumer profits (Krishnaprasad et al., 2009; Han et al., 2008; Elsaid et al., 2011). Other possible applications of kenaf fibre with synthetic polymers in composites include automotive interior lining, wallboards, ceilings and furniture as well as bio-engineering and bio-medical devices (Namvar et al., 2014; Pang et al., 2015). Similarly, Juliana et al. (2012) found that kenaf fibres are widely considered as suitable biological resources and a potential substitute for fossil fuels and wood-pulps. According to Mossello et al. (2010) with the possibility of planting twice a year, kenaf has great potential as an alternative source of fibres for medium density fibreboard (MDF) and particleboard manufacturing.

2.2.4 Chemical treatment of kenaf fibre

It is well known that natural fibres require some chemical treatments. Although, this can increase the price of the fibres, it also enhances the interfacial adhesion between the fibre and the matrix, which reduces the water absorption characteristic of the fibre. Therefore, chemical treatments reportedly enhance the quality of fibre. A few of the available chemical modification processes are alkaline treatment, silane treatment,

acetylation of natural fibre, benzoylation treatment, acrylation and acrylonitratrile grafting, maleated coupling agents. Other treatment methods include permanganate treatment, peroxide treatment, isocyanate treatment, etherification of natural fibres and plasma treatment (Haniffah et al. 2015).

Like other natural fibres, kenaf is hydrophilic. Hence, it is necessary to treat the fibres to enhance compatibility with hydrophobic materials (Aziz et al., 2005). Previous researchers agree that alkaline treatment, also known as mercerization, is one of the most acknowledged treatments. It is also the easiest surface treatment technique for most natural fibres including kenaf (Gassan and Bledzki, 1999; Mohanty et al., 2000; Ray et al., 2002; Xia et al., 2016). The process of mercerisation is performed using NaOH, KOH, or LiOH which typically decrease the hydrogen content of the cellulose. Similarly, the process increases the amount of amorphous cellulose at the expense of crystalline cellulose. The chemical treatment cleans and creates a rough surface on the fibre which is important for interfacial bonding of the polymer and kenaf fibre. The surface of the untreated fibre is covered with hemicellulose, lignin and wax which can be removed by chemical treatment. Consequently, the treated fibre has a rough surface that provides better interlocking between the polymer and fibre.

However, high concentrations of alkali may depolymerise the native cellulose and delignify the fibre excessively, adversely affecting the strength of the fibre. The alkaline treatment of kenaf fibre affects not only the surface but also the texture of fibre resulting in the variation of the mechanical and physical properties. Therefore, Ramesh (2016) reviewed the effects of alkaline treatment with different NaOH concentrations and immersion times, as reported by various researchers. The concentration of NaOH solution, treatment times, and treatment temperature play a vital role in achieving the optimum efficiency of the fibre as far as the adhesive characteristics of the fibres are concerned

(Mohanty et al., 2001). It was observed that by increasing the NaOH concentration, cleanness, and roughness of the fibre surface was improved. It was also reported that 6% NaOH yielded the optimum concentration of NaOH for the chemical treatment of kenaf fibre, as higher concentrations could damage the fibres and reduce the fibre strength (Edeerozey et al., 2007). This treatment removes a certain amount of lignin, wax, and oils covering the external surface of the fibre cell wall and depolymerises the native cellulose structure exposing its short length crystallites. The optimum alkali treatment is both an effective surface modification and low-cost treatment of natural fibres. Furthermore, moisture absorption is decreased by modification of the most water-absorbing fibre components, which is hemicellulose, through mercerisation (Ibrahim et al., 2016). The reaction of NaOH with natural fibre (Cell–OH) is understood to occur as shown in Eq. 1 (Ramesh, 2016):

$$Cell - OH + NaOH \rightarrow Cell - O^{-} Na^{+} + H_2O + \text{Surface impurities} \quad \text{(Eq. 1)}$$

2.3 Transparent conducting oxide (TCO)

The TCO and its mixtures have extensive applications in flat panel screens, in-touch panels, solar cells, and other future devices capable of transporting electrical charge and transmitting visible photon. Essentially, these are also used in electrochromic windows, oven windows, and energy-efficient windows that trap and release heat during winter and summer. TCO is a useful material for transparent optoelectronic application due to its unique features of optical properties in the visible light region such as high optical transmittance over ~85%. Furthermore, it has a wide optical band gap above 3 eV and controllable electrical conductivity with carrier concentrations of at least 1020 cm^{-3} and resistivity of about 10^{-4} Ω.cm. It combines two important properties which are good electrical conduction and high transmission in the visible light region (380 – 780 nm).

Achieving high electrical conductivity and good optical transmission in TCO materials is crucial for most applications (Rezaee Roknabadi et al., 2009).

Most of the TCO materials are n-type semiconductors, but p-type TCO materials have also been researched and developed. Such TCO includes ZnO:Mg, ZnO:N, IZO, NiO, NiO:Li, $CuAlO_2$, Cu_2SrO_2, and $CuGaO_2$ thin films. Currently, these materials have not yet found a place in actual applications. The coating properties of TCO can be improved by investigating new materials that consist of ternary oxide compounds based on ZnO. For example, ternary oxides such as In-doped ZnO (IZO), Al-doped ZnO (AZO), Ti-doped ZnO (TZO), and Si-doped ZnO (SZO) have attracted considerable attention as alternative materials for ITO. Indium-tin oxide (ITO) films are the most extensively studied and commonly used TCO based films. This is due to the high electrical conductivity and high transparency of the films, in addition to, the ease of fabrication on glass substrates at temperatures above 473 K. However, over time amorphous ITO films exhibit lower electrical conductivity, along with poor optical transparency and chemical stability. These problems can be solved by using IZO films deposited by various techniques which enhance excellent chemical stability, high electrical conductivity, and optical transparency (Meng and Dos Santos et al., 1997; Song et al., 1999; Kim et al., 2003).

Recently, zinc oxide or impurity (B, Al, Ga, In, and Zr) doped zinc oxide films have been investigated because of its nontoxicity, inexpensiveness, and availability. The development of IZO coating on low processing temperature materials such as natural fibres is challenging, yet promising, but has not been explored by the previous researchers. The recent increased demand and emerging interest in the development of electrically conductive polymer composites make the prospect of IZO coating on natural fibre very interesting, due to its potential for application as conductive fillers or reinforcements.

2.3.1 TCO materials – Zinc Oxide (ZnO)

ZnO has direct semiconductor bandgap of 3.27 eV. Therefore, it has been recognised for its promising applications in blue/UV optoelectronics, spintronic devices, surface acoustic wave devices and sensor applications. El Yamny and Rafea (2012) reported that undoped ZnO thin films are unstable at high temperatures but can be improved by introducing impurities into the ZnO host lattice, which dramatically reduces this disadvantage. The doping of ZnO with elements of Group XIII such as B, Al, In, Ga increases the conductivity of the ZnO thin films. The doping process is performed by replacing Zn^{2+} atoms with an impurity of higher valence. It is worth mentioning that the efficiency of the dopant element depends on its electronegativity and difference in the ionic radius compared to zinc. Aluminum and indium are well-known dopants for n-type ZnO and have been studied to some extent (Matsubara et al., 2004).

Transparent conducting electrodes for thin solar cells have identified zinc oxide as one of the best options due to its high chemical stability against reducing environment (Ortiz et al., 1988). Furthermore, the simultaneous concurrence of high transparency in the visible region and highly conductive textured surface are advantages. Other benefits are the wide availability of the material, non-toxicity, and easy handling which make ZnO suitable for wide-ranging applications (Patil, 1999).

In comparison, indium tin oxide (ITO) has been mainly used as TCO anode because of its high conductivity, large work function, and transparency over the visible range (Kim et al., 1999). However, pure ZnO is a well-known n-type semiconductor with high resistivity. Therefore, the addition of indium impurity will substitute Zn because of the similarity in ionic radius. Since Indium has one more electron than Zn, it acts as donor impurity and creates an n-semiconductor (Rezaee Roknabadi et al., 2009). The doping directly affects the carrier concentration thereby influencing its conductivity. Although

introducing impurities is necessary, the concentration has a limitation otherwise a very high doping level will result in problems. These include high free carrier absorption, high plasma resonance reflectivity, and low visible wavelength transparency. Nonetheless, IZO has attracted significant attention as transparent electrodes due to its good electrical conductivity which occurs in the high visible transmittance range of 400 to 900 nm. Other advantages of IZO include a large work function, excellent surface smoothness, and low-temperature deposition (Kim et al., 2009).

The indium-doped zinc oxide film was deposited from the mixed precursor of indium and zinc salts in the atomic per cent ratio, In/Zn = 1% – 9 % using dip coating method. Consequently, the doping range from 1% to 5% demonstrated the lowest electrical resistivity. This indicates an increase in donor concentration, which is attractive for many optical and electrical applications. The donor action of indium compensated for the grain boundary scattering leading to a decrease in film resistivity. However, as the doping concentration increased, the grain size decreased due to deformation. Although the carrier concentration is expected to increase by indium doping, the smaller grain size enhances the grain boundary scattering. This ultimately leads to an increase in the resistance at higher indium content (El Yamny and Rafea, 2012). Furthermore, an increase in dopant to more than 6 wt.% changed the n-type semiconductor to p-type (Rezaee Roknabadi et al., 2009) as previously studied at 2, 4, 6, 8, 16 and 32 wt.% dopant concentration. The study by Rezaee Roknabadi et al. (2009) revealed that higher impurity (above 6%) converts n-type to p-type semiconductors. It was discovered that conductivity initially decreased after the n-type to p-type semiconductor conversion, thereby decreasing the carrier concentration. However, following the increasing impurity, the carrier concentration increases so that the lowest resistivity was observed with an impurity of 32% (Rezaee Roknabadi et al., 2009).

Recently, transparent conductive films have been prepared on numerous different substrates such as glass, sapphire, and polymer as studied by previous researchers (Rezaee Roknabadi et al., 2009; Do-Hoon et al., 2009; Biswal et al., 2014; Lee et al., 2012). Each substrate has its specific properties that may cater to different needs. For example, glass substrates are heavy and brittle, whereas polymeric substrates such as polyethylene terephthalate (PET) are lightweight, unbreakable, and conveniently portable. The nature of the substrates may affect the microstructure, crystallisation, morphology and electrical properties of films.

The rapidly growing interest in natural fibres is based on either fundamental research or industrial applications. The fibres are renewable, cheap, biodegradable and can be completely or partially recycled. Plant-derived natural fibres consist of cellulose, hemicelluloses, lignin, pectin and waxy substances. Cellulose gives strength, stiffness, and structural stability to the fibre. The geometry of the cell determines the mechanical properties of natural fibres. In addition, the availability, renewability, low density, and price, as well as satisfactory mechanical properties, make natural fibres an attractive ecological alternative to glass, carbon, and man-made fibres used in manufacturing composites (Dagade and Shaikh, 2015). However, there are several challenges presented by natural fibres such as large variability of mechanical properties (Eichhorn et al., 2001; Sydenstricker et al., 2003). Other drawbacks include low ultimate strength and elongation along with problems with nozzle flow in injection moulding machines and bubbles in the final product (Toriz et al., 2002). Furthermore, most natural fibres have low degradation temperatures (~200 ^{o}C), resulting in incompatibility during curing or other high-temperature processes. This restricts natural fibre composites to relatively low-temperature applications (Sgriccia et al., 2008).

2.3.2 TCO deposition technique

There are various techniques used for TCO deposition such as dip coating, sputtering, chemical vapour deposition, and electron beam evaporation (or spray pyrolysis). Other techniques include RF magnetron sputtering, sol-gel process, electrochemical deposition, molecular beam epitaxy (MBE), pulsed laser deposition (PLD), and metal organic chemical vapour deposition (El Yamny and Rafea, 2012). Due to the very high deposition rate, electron beam evaporation method has a potential industrial application (Keshavarzi et al., 2011). Sputtering can be used for rapidly coating large areas of a substrate at competitive costs compared to other methods (Lee, 2008).

TCO based on indium-doped zinc oxide films in the nanoscales have been successfully prepared by a combination of dip coating and thermal decomposition processes (El Yamny and Rafea, 2012). Therefore, the deposition on organic substrates such as polyimide (PI) and even on flexible organic substrates such as polypropylene adipate (PPA) is possible (Hao et al., 2002). Reactive radio frequency sputtering (rf MS) is commonly utilised for the sputter deposition of TCO materials (Gorley et al., 2005).

In other research, Rezaee Roknabadi et al. (2009) applied the sol-gel method to produce indium doped zinc oxide on a glass substrate due to its high purity, homogenous and large area film at low temperatures. Thamarai et al. (2014) claimed that dip coating method is extremely attractive due to its advantageous features over other thin film deposition technique. These include its simple low temperature, low cost, ease of coating on large surfaces and low evaporation temperature.

The dip coating deposition process is an economical technique for fast and easy control of process parameters as shown in Figure 2.2. The process is separated into three important technical stages; immersion and dwell time, deposition and drainage, and evaporation (Brinker, 2004). Figure 2.3 illustrates the details of the flow patterns

(streamlines) during the dip-coating process where U_0 is the withdrawal speed, S is the stagnation point, δ the boundary layer and h_0 is the thickness of the entrained fluid film on the substrate (Schneller et al., 2013).

El Yamny and Rafea (2012) has successfully studied the Zn: In by dip coating with the aim to produce low cost, wide area productivity and good film quality required to compete with other sophisticated preparation techniques. It was reported the dipping rate in the range of 2 mm/s to 38 mm/s is the most suitable for good film quality while dipping rates 30 - 38 mm/s produced thicker films at lower deposition cycles. The higher dipping rate produces films with lower transparency while the small deposition rate requires a large number of deposition cycles (El Yamny and Rafea, 2012).

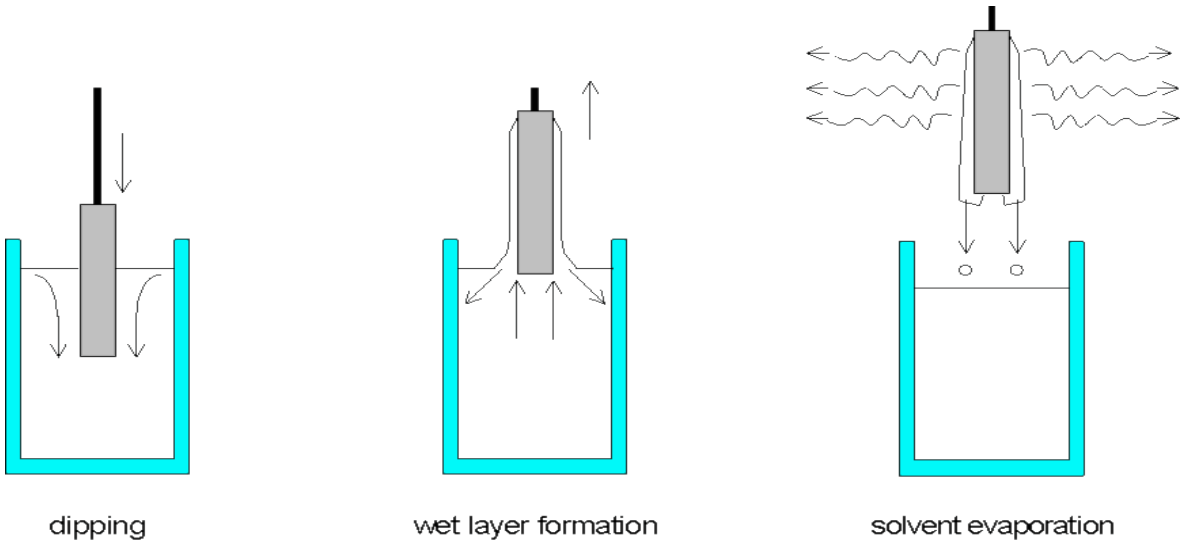

Figure 2.2: Stages of the dip coating process.

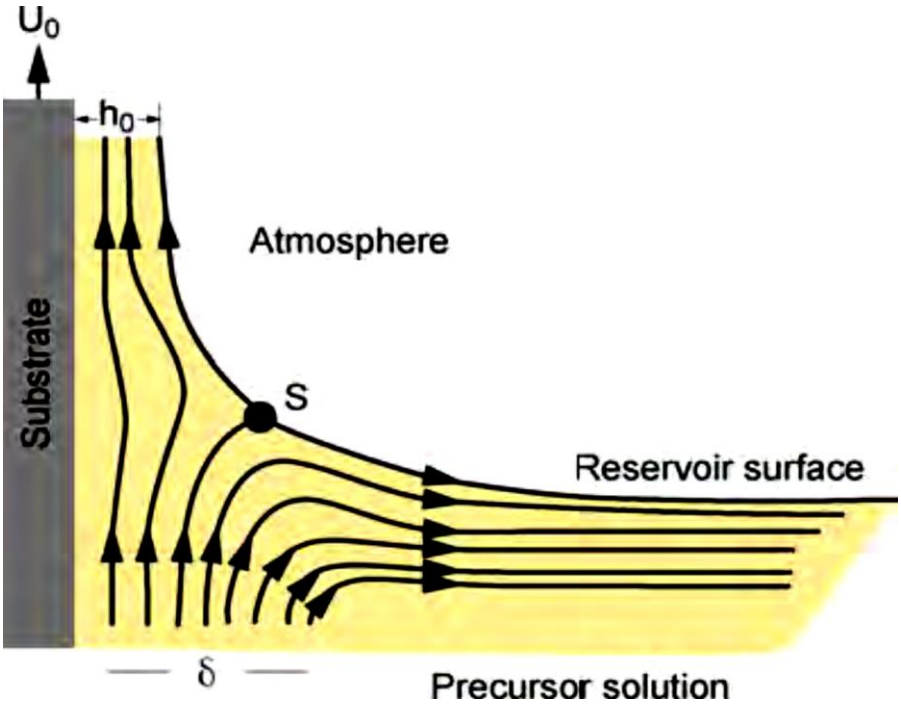

Figure 2.3: Flow pattern during dip coating process.

2.3.3 Parameters of coating

i) Thickness

The thickness of the film coating, which ranges from approximately 50 nm to 2000 nm, is one of many factors that determine the electrical and optical properties of ZnO-based TCO films. The electrical conductivity becomes better while transmittance may become poorer as the film thickness increases (Rao and Santhoshkumar, 2009). Kuo et al. (2011) reported that when the thickness is over the critical value, the excess internal stress causes structural discontinuity by the bifurcated orientation which could crack the film. This can ultimately restrict the carrier mobility and reduce the conductivity. Coating thickness is crucial as it is directly related to the resistivity of the ZnO thin film. The crystallite's size and orientation which depend on the film thickness play a big role in controlling the electrical conductivity of the polycrystalline ZnO film (Rusop, 2012). It was found that the crystalline quality and the grain size increases with film thickness. The

resistivity first decreases for thicknesses up to 41.2 nm due to the increase in carrier mobility. For films above 50 nm, the resistivity increases due to the increase of trapped carriers in the grain boundary.

The resistivity and thickness of the film are affected by the dipping rate. Figure 2.4 represents the dependence of the film thickness on dipping rate. As the dipping rate increases, the amount of precursor deposited on the substrate increases, then evaporation of the solvent occurs before dropping back to the precursor. In addition, at lower dipping rate, better film quality and clarity are produced. Furthermore, the increase of dipping rate strongly decreases the resistivity of the film thickness. This phenomenon is due to the compactness of the grains by the considerably higher amount of the deposited precursor. At a very high dipping rate, milky and powdered films are obtained, while at a very low dipping rate, both the film thickness and compactness of the grains become too low to conduct an electrical current. The dipping rate in the range of 2 - 40 mm/s is considered as the optimal range for better, clear, and electrically conducting films (El Yamny and Rafea, 2012).

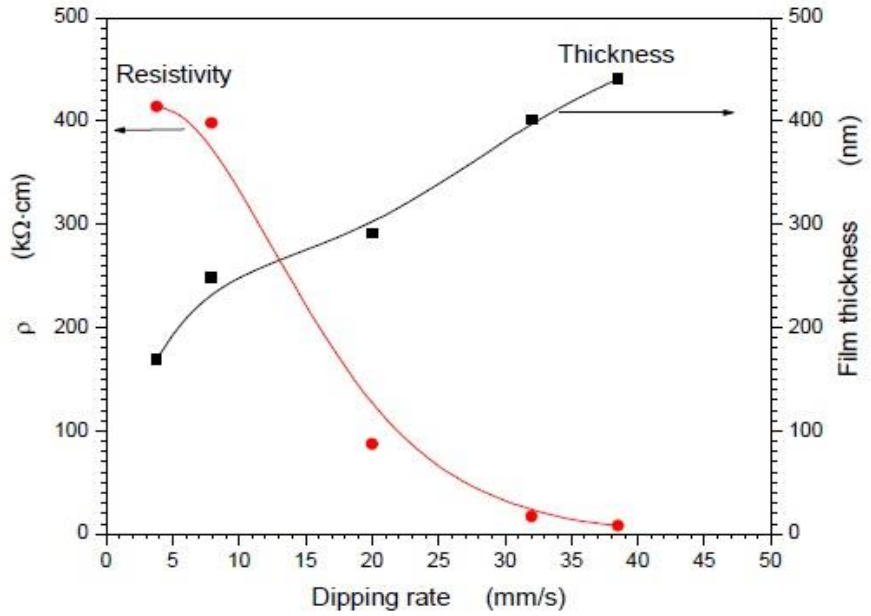

Fig. 2.4: Dipping rate dependence of electrical resistivity and film thickness (El Yamny and Rafea, 2012).

ii) Growth temperature

The transparency, conductivity, and optical properties of low processing materials like polymers and natural fibres can be improved by low temperature (<200 °C) synthesis with TCO. The low growth temperature is required for coating on various flexible substrates such as OLED, PMMA and natural fibre. However, at low growth temperatures, the resulting films exhibit poor properties. In recent years, significant progress in the growth of high-quality films at low temperature on flexible substrates has been reported. These films have attracted extensive attention owing to the low processing cost and many unique applications (Kim et al., 2012; Zhu et al., 2013). For example, Clatot et al., (2011) successfully developed Si-doped zinc oxide (SZO, Si 3wt.%) thin films at a relatively low temperature (≤150 °C) by pulsed laser deposition (PLD). The recrystallization and growth of films reduced internal imperfections, resulting in higher conductivity, Hall mobility (increased from 6.56 to 10.12 cm^2/Vs), and higher transmittance (Zhang and Cheng, 2011; Zhang et al., 2012). It is also worthy to note that the absence of damages on the underlying substrates makes this technology promising in various low-temperature applications (Liu et al., 2013).

Indium zinc oxide (IZO) is a material that exhibits good transparency in the visible range, low resistivity, and high mobility (Lee and Park, 2003; Dehuff et al., 2005; Craciun et al., 2014). The annealing temperature has a direct effect on the electrical properties and surface morphology of IZO coating. Upon annealing in the temperature range of 500 °C to 1000 °C, the thin film crystallises into polycrystalline In_2O_3 (ZnO). The lowest electrical resistivity was obtained when the annealing temperature was 700 °C at 2 Ω.cm. At higher temperatures, the amount of oxygen desorption increases along with free carriers in the thin films (Lee et al., 2012). With the increase of the annealing temperature of IZO (In_2O_3:ZnO = 90:10 wt.%) from 100 to 300 °C, the carrier concentration reportedly

decreased with increasing resistivity. The average transmittance of IZO thin films decreased slightly with increasing annealing temperature yielding an amorphous structure (Jeon et al., 2011). During the annealing treatment, the absorbed oxygen reduced the oxygen vacancies in the film thereby lowering the carrier density but increasing the mobility. When annealed at temperatures of 200, 300, 400 °C for 1 h in open air, the structure of ITO changed from amorphous to polycrystalline, although IZO remained amorphous. Overall, the transmittance of both films was improved while the resistivity decreased with increasing annealing temperature at low oxygen content (Kim et al., 2009). Upon annealing at a temperature range of 500 °C to 1000 °C, the IZO thin film (prepared with zinc acetate dihydrate ($Zn(CH_3COO)_2.2H_2O$) and indium acetate ($In(CH_3COO)_3$) as starting precursors, and 2-methoxyethanol with 1-propanol as solvents) crystallized into In_2O_3:ZnO polycrystalline (Lee et al., 2012).

iii) Number of cycles

The number of cycles is another important parametric consideration due to its influence on the TCO film thickness. As reported by El Yamny and Rafea (2012), increasing the film thickness and the deposition cycles decreases the film quality and transparency. Figure 2.5(a) and (b) shows the optical transmittance and film thickness of In_2O_3:ZnO depends on deposition cycles. Thamarai et al. (2014) also revealed the optical transmittance decreased from 65% to 55% and 52% with the increase of growth time from 3 to 4 and 5 hours, respectively. The results also showed that the bandgap decreased with increasing growth time. The decrease in the band gap of ZnO films may be attributed to the improvement in the crystalline quality of the films along with the reduction in porosity and increase in grain size.

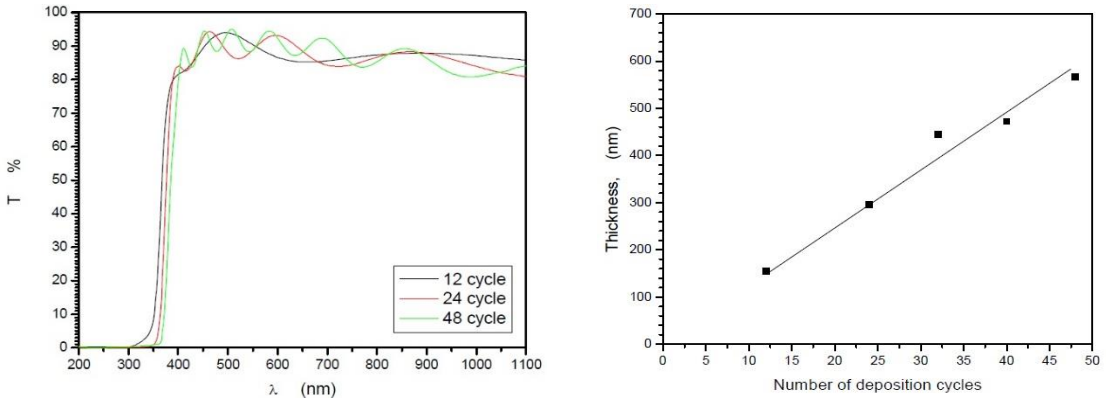

(a) (b)

Figure 2.5: a) Deposition cycles dependence of the optical transmittance of ZnO:In ;b) Deposition cycles dependence of the film thickness (El Yamny and Rafea, 2012).

2.3.4 Properties of IZO

i) Electrical properties

The electrical conductivity is due to doping either by oxygen vacancies or by extrinsic dopants. Rezaee Roknabadi et al. (2009) found that increasing the impurity above 6% transforms the n-type semiconductor to a p-type. This is probably due to the decrease in donor property of indium. However, the electrical conductivity improves as the film thickness increases, as more photons are adsorbed when the thickness increases (Rao and Santhoshkumar, 2009). Furthermore, the doping of ZnO by indium in the range 1% to 9 % shifts the absorption edge towards the shorter wavelength. The shift in the absorption edge is reportedly attributed to carrier concentrations, carrier distributions, and defects in the film (El Yamny and Rafea, 2012). The carrier concentration increased sharply and reached a maximum value at 700 °C before decreasing. The free carriers of IZO originate from donor sites associated with oxygen vacancies, hence the curve of the carrier concentration could be explained by oxygen vacancies. As the temperature increases, the amount of oxygen desorption increased, and free carriers in the thin films also increased. However, the situation was reversed over 700 °C because of oxygen diffusion into the thin films.

Similarly, the increase in temperature enhanced the diffusion rate and oxygen compensation (Lee et al., 2012). The optimal values of indium were between 1.5% and 5%, as the donor concentration increased and ZnO showed the lowest resistivity, as demonstrated in Figure 2.6. The donor action of indium compensates the grain boundary scattering and contributes to the decrease in film resistivity. As the doping concentration increases, the grain size decreases due to deformation. Although the carrier concentration is expected to increase with indium doping, the smaller grain size enhances the grain boundary scattering and the resistance at higher indium content. Furthermore, Barquinha et al. (2007) studied IZO annealing in three different atmospheres, i.e., vacuum, air and oxygen. It was described that for the conductive thin films, only the oxygen atmosphere was critical, leading to an increase of the electrical resistivity above one order of magnitude for temperatures above 250 °C.

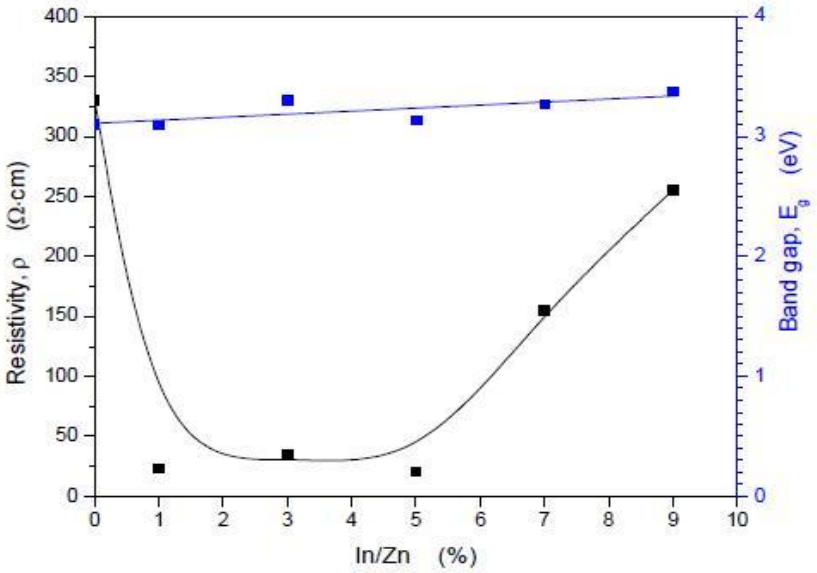

Figure 2.6: In/Zn percentage (0-9%) dependence of film resistivity and band gap energy (El Yamny and Rafea, 2012).

ii) Optical properties

It is proved by previous researchers that the optical transmittance spectra showed a very good transmittance of 99.5 % within the wavelength of 540 nm for the film doped

with 2 wt% In onto glass substrate. Increased dopant concentration would reduce transmittance of visual spectra of samples. This is due to incident diffraction caused by the indium atoms surrounded by ZnO indicating that indium atom is slightly larger than Zn and crystal imperfection (Rezaee Roknabadi et al., 2009). Moss-Burstein effect explained that the optical band-gap is shifted towards short wavelengths with high carrier concentration values. This is contrast to Lee et al. (2012) which mentioned that the absorption edge shifted towards long wavelengths with increased concentration. This might be due to the phenomenon of 'quantum confinement effect', which is caused by the grain size of films (Ghosh et al., 2007). In fact, the grain size of the thin films was comparatively small in that range of temperature. In other research, Yue et al. (2013) observed that the transparency of the IZO film was obviously improved by incorporation of Al. AIZO are highly transparent in the visible range (400-700nm) with average > 90% except of Al-free IZO thin film. Figure 2.7 (a) and (b) shows the optical transmittance spectra of the AIZO films as a function of the Al content (Yue et al., 2013).

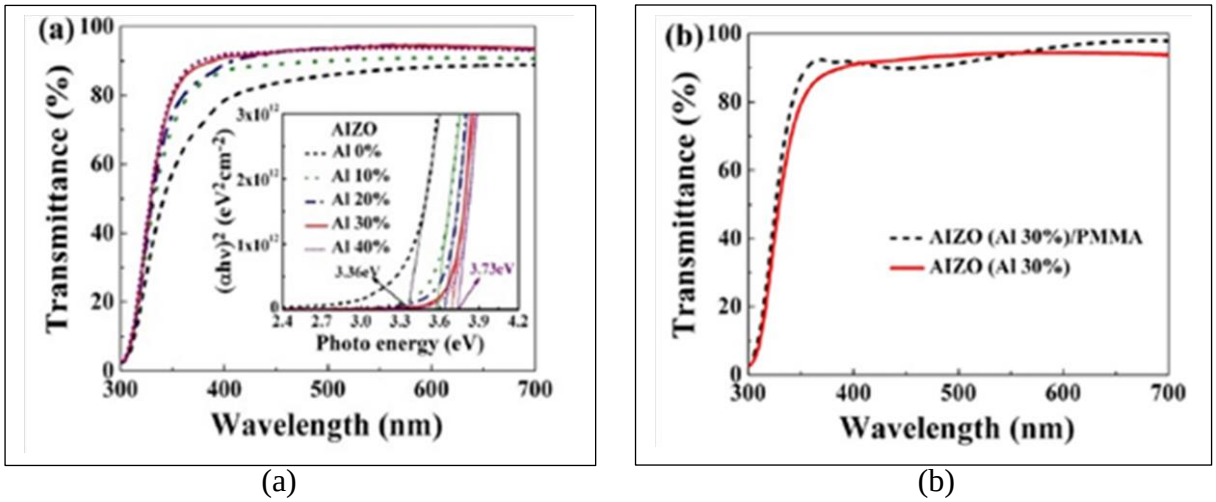

(a) (b)

Figure 2.7: (a) Optical transmittance spectra of a-AIZO thin films dip-coated with different Al content. The inset shows a plot of $(\alpha h\nu)^2$ versus $h\nu$. (b) Typical optical transmittance spectra of a-AIZO (Al 30%) + PMMA double layers (Yue et al., 2013).

2.3.5 Summary of TCO-IZO

TCO-IZO development as reported in various related papers has been reviewed. Good TCO should have a wide optical band gap (>3.5 eV), low electrical resistivity ($<10^{-3}\Omega$.cm) and high optical transmittance (>80 %) in the visible region. Doping concentration plays an important role because it affects carrier concentration and influences conductivity sequentially. The preparation methods, substrate type, film thickness, growth (annealing) temperature, number of cycles and ambient atmosphere are factors that determine the electrical, optical, and structural properties of TCO.

Among these, the film thickness critically needs to be controlled as it is directly related to resistivity. Furthermore, growth temperature should be considered for substrates with low processing temperatures such as polymers and natural fibres. As IZO coating onto glass and polymer substrates by various deposition techniques has been widely studied, the author will focus on the study of coating onto a natural fibre substrate, as this has not yet been covered. Furthermore, the coating properties are unknown, and its future potential requires more investigation. As the interest in conductive polymer composites is increasing, the new natural fibre based TCO-IZO coating can be utilized as conductive filler or reinforcement in polymer composites.

2.4 Titanium dioxide (TiO_2)

2.4.1 Introduction

TiO_2 is a well-known material that has been extensively studied in the last few decades due to its potential applications in various fields. Due to its low cost, non-toxicity and chemical stability, it is used in various different commercial products like sunscreen, pigment, toothpaste and ointment. TiO_2 is basically an oxide of Ti (Titanium) and belongs to the family of transition metal oxides. It has three different polymorphs namely;

Anatase-, Rutile- and Brookite-crystal structures (Luttrell et al., 2014). Table 2.2 stated the crystal structure data for TiO_2.

Table 2.2: Crystal structure data for TiO_2 (Gupta and Tripathi, 2011).

Properties	**Rutile**	**Anatase**	**Brookite**
Crystal structure	Tetragonal	Tetragonal	Orthorhombic
Lattice constant (Å)	a = 4.5936 c =2.9587	a = 3.784 c = 9.515	a = 9.184 b = 5.447 c = 5.154
Space group	$P4_2/mnm$	$I4_1/amd$	Pbca
Molecule (cell)	2	2	4
Volume/molecule ($Å^3$)	31.2160	34.061	32.172
Density (g cm^{-3})	4.13	3.79	3.99
Ti–O bond length (Å)	1.949 (4) 1.980 (2)	1.937(4) 1.965(2)	1.87–2.04
O–Ti–O bond angle	81.2° 90.0°	77.7° 92.6°	77.0°–105°

As known, TiO_2 is the most widely used photocatalyst for the decomposition of organic pollutants because it is chemically stable and biologically benign (Fujishima et al., 2008). The TiO_2 band gap for rutile and anatase are 3.0 eV and 3.2 eV, respectively, which ensures photoactivity under UV light (Luttrell et al., 2008). The most common commercial photocatalyst is the Degussa P-25, a powder consisting of both rutile and anatase crystallites (Ohno et al., 2001. The phase mixture of different polymorphs reportedly has synergistic effects, as such increased photocatalytic activity is observed compared to pure phases (Scanlon et al., 2013). However, for pure phases, it is generally accepted that anatase exhibits a higher photocatalytic activity compared to rutile TiO_2 (Liu et al., 2012). However, there is no specific accepted explanation of TiO_2 for different polymorphs or surface orientations towards photocatalytic activity. Nevertheless, some possible explanations for the statement include:

i. Anatase has a larger band gap than rutile TiO_2. The larger the band gaps, the higher the energy levels relative to redox potentials of adsorbed molecules.

This increases the oxidation ‘power’ of electrons and facilitates electron transfer from TiO_2 to adsorbed molecules (Batzill, 2011).

ii. Surface properties may play a role in the adsorption of molecules and subsequent charge transfer to the molecule. For example (i) chemical effects, e.g. coordination structure of surfaces that control adsorption of molecules (Diebold, 2003) (ii) electronic structure of the clean surface (Tao and Batzill, 2010) or defects and adsorbate (Tao et. al, 2011) (iii) interaction of molecules with surface defects (Liu et al., 2012; Setvín et al., 2013) and (iv) surface potential differences (such as work function differences measured in vacuum or flat band potentials in aqueous solution) may affect charge transfer from the photocatalyst to molecules (Bullard et al., 2006).

iii. Anatase exhibits an indirect bandgap that is smaller than its direct band gap. For rutile, in contrast, its fundamental band gap is either direct, or its indirect band gap is very similar to its direct band gap. Semiconductors with indirect bandgap generally exhibit longer charge carrier lifetimes compared to direct gap materials. A longer electron-hole pair life in anatase than in rutile would make it more likely for charge carriers to participate in surface reactions. One evidence for longer charge carrier lifetimes in anatase than in rutile comes from transient photoconductivity measurements on single crystalline samples (Xu et al., 2011).

iv. Charge transport may differ for different polymorphs. In this case, the exciton lifetime and its mobility need to be considered. Only excitons that efficiently diffuse can reach the surface within their lifetime. The preferential diffusion of excitons along certain crystallographic directions has been proposed for other photocatalysts. This is critical to explaining the surface orientation

dependencies in their oxidation/reduction behaviour (Giocondi et al., 2007). One measure for exciton mobility is the polaron effective mass. Although contradicting values for effective masses are reported. Generally, a higher effective mass is reported for rutile than for anatase.

As the most promising photocatalyst, TiO_2 materials are sought as a potential solution to many serious environmental and pollution-related challenges worldwide. Hence, TiO_2 is expected to play a big role in solving the energy crises by utilising solar energy based on water splitting devices and photovoltaics (Gupta and Tripathi, 2011).

2.4.2 Templated synthesis of nanostructured materials

Foremost, there has been a tremendous advancement in the preparation of TiO_2 nanomaterials. These materials have been found to be effective in various applications (Chen and Mao, 2007). The preparation of TiO_2 nanomaterials in different forms like nanoparticles, nanorods, nanowires and nanotubes has been accomplished through various synthesis methods. The various processing methods include micelle synthesised TiO_2 nanoparticles and the reverse micelle method. Others include the sol-gel, sol method, solvothermal method and templated synthesis method (Chen and Mao, 2007). Among the different methods for synthesising TiO_2 nanomaterials, template-directed synthesis has the most significant advantages since it is cheap, simple and versatile. Templating is one of the most important techniques for the controlled synthesis of nanostructured materials. This powerful tool uses a pre-existing guide with desired nanoscale features to direct the formation of nanomaterials into forms that are otherwise difficult to obtain. As a result, templated synthesis is capable of producing nanostructures with unique structures, morphologies and properties (Liu et al., 2013).

There are some works on the application of various natural and synthetic materials as templates for TiO_2 nanostructures. Figure 2.8(a) and (b) refer to the classification of templated synthesis for micro- and nano-scaling. Generally, templated synthesis of nanostructured materials include the following steps: (1) template preparation, (2) directed synthesis of target materials using the template, and (3) template removal (if necessary). Natural fibres with fine structures such as cotton, wool, spider silk, dog hair, gills of the mushroom, and wood are reportedly used as templates for the synthesis of nanomaterials.

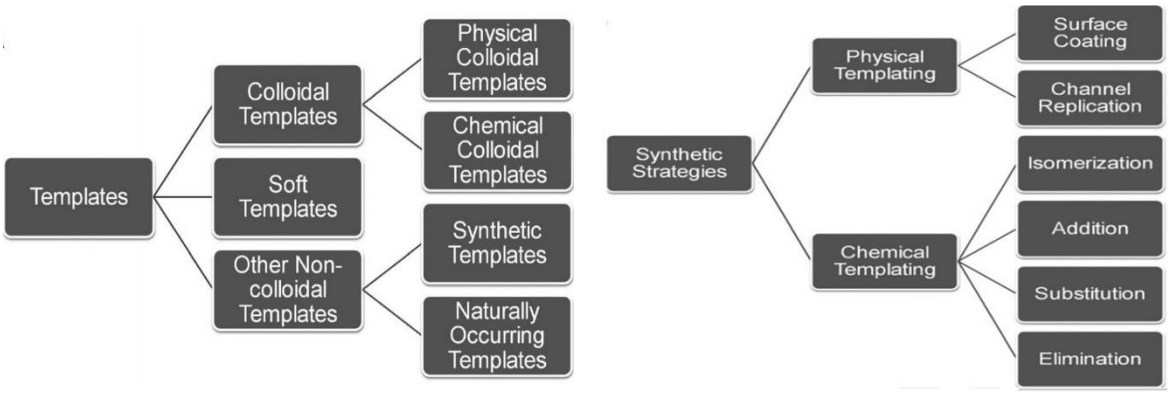

(a) (b)

Figure 2.8: Classification of nano- and micro-scale templated synthesis by (a) types of templates and (b) synthetic strategies (Liu et al., 2013).

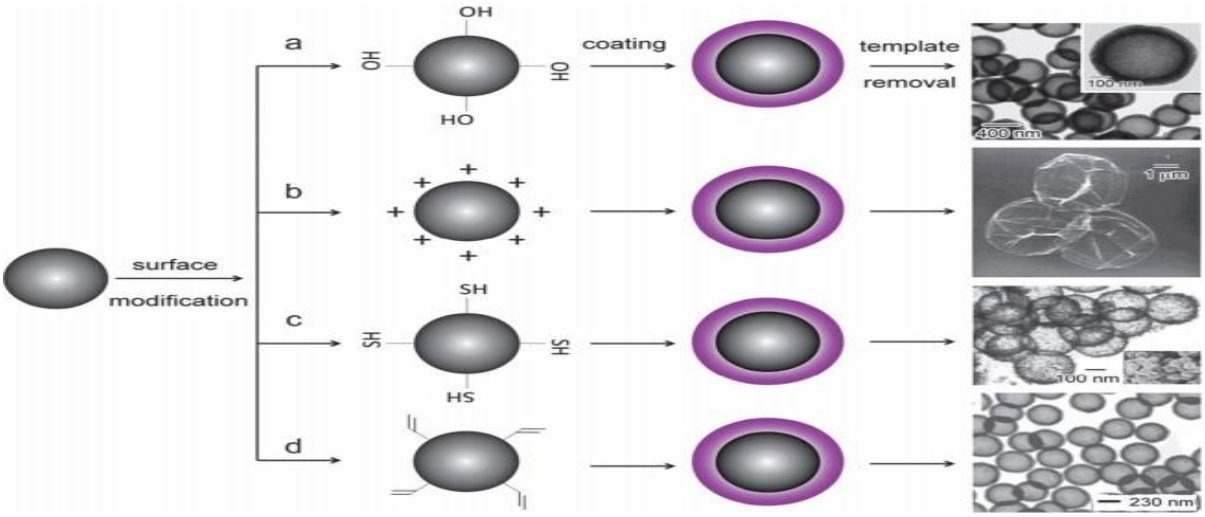

Figure 2.9: Syntheses of hollow structures by a surface coating on colloidal templates typically include steps of surface modification, surface coating of target materials and template removal and post-treatment of resultant materials (Xu and Asher, 2004).

In contrast to the synthesis of target materials, the strategies based on physical templates include surface coating and channel replication methods. However, for chemical templated synthesis, the chemical transformations during the synthesis may include isomerisation along with the addition, substitution, and elimination of chemical species. Accordingly, nearly all types of materials can be utilised, from metals, semiconductors, and ceramics to soft polymers. Others include zero-dimensional (0D) nanoparticles, one-dimensional (1D) nanowires, and two or three dimensional (2D and 3D) hierarchical nanostructures. The physical and chemical properties of the resultant materials can be preserved by removing the template after synthesis. This is achieved by physical methods such as dissolution or chemical methods including calcination and etching based on the nature of the templates (Liu et al., 2013). For example, the synthesis of the hollow structure by Xu and Asher (2004) was established through the surface coating on colloidal templates. The study examined the different surface modification, chemistry, and coating techniques for synthesising various hollow structures as illustrated in Figure 2.9.

2.4.3 Sol gel method

The sol-gel method is a widely used wet chemical method for the synthesis of ceramics and other metal oxide materials (Liu et al., 2013a). In a typical sol-gel process, a colloidal suspension, or a sol, is formed from the hydrolysis and polymerisation reactions of the precursors, which are usually inorganic metal salts or metal organic compounds such as metal alkoxides. The complete polymerisation and loss of solvent enhance the transition from the liquid sol into a solid gel phase. Hence, thin films can be produced on a piece of the substrate by spin-coating or dip-coating. A wet gel will form when the sol is cast into a mould, and the wet gel is converted into a dense ceramic with further drying and heat treatment. Hence, a highly porous and extremely low-density material called

aerogel is obtained if the solvent in a wet gel is removed under supercritical conditions. However, ceramic fibres can be drawn from the sol when its viscosity is adjusted to an appropriate range. Ultrafine and uniform ceramic powders are formed by precipitation, spray pyrolysis, or emulsion techniques. Under proper conditions, nanomaterials can also be obtained (Chen and Mao, 2007).

TiO_2 nanomaterials have been synthesised from hydrolysis of a titanium precursor using the sol-gel method. The process typically proceeds via an acid-catalysed hydrolysis step of titanium (IV) alkoxide followed by condensation (Bessekhouad et al., 2003; Oskam et al., 2003). The development of Ti-O-Ti chains is favoured by a low content of water, low hydrolysis rates, and excess titanium alkoxide in the reaction mixture. Hence, three-dimensional polymeric skeletons with close packing result from the development of Ti-O-Ti chains. The formation of $Ti(OH)_4$ is favoured by high hydrolysis rates at medium amounts of water. The presence of a large quantity of Ti-OH and insufficient development of three-dimensional polymeric skeletons lead to loosely packed first-order particles. The polymeric Ti-O-Ti chains are developed in the presence of a large excess of water. Closely packed first-order particles are yielded through a three-dimensionally developed gel skeleton (Bessekhouad et al., 2003; Oskam et al., 2003). Studies on the growth kinetics of TiO_2 nanoparticles in aqueous solution and titanium tetraisopropoxide (TTIP) precursor showed that the rate constant for coarsening increases with temperature. This was ascribed to the temperature dependence of the viscosity of the solution and the equilibrium solubility of TiO_2. The epitaxial self-assembly of primary particles forms secondary particles at higher temperatures and time; therefore the number of primary particles per secondary particle also increases with time. The average TiO_2 nanoparticle radius increases linearly with time, in agreement with the Lifshitz-Slyozov-Wagner model for coarsening (Oskam et al.,2003) Sugimoto et al. (2003), conducted a series of tests on the

formation of TiO_2 nanoparticles of different sizes and shapes by tuning the reaction parameters using the sol-gel method. A stock solution of 0.50 M Ti source was prepared by mixing TTIP with triethanolamine (TEOA) ([TTIP]/[TEOA] = 1:2), followed by the addition of water. Next, the stock solution was diluted with a shape controller solution and aged at 100 °C for 1 day and at 140 °C for 3 days. The $HClO_4$ or NaOH solution was added to adjust the pH. Furthermore, amines including TEOA, diethylenetriamine, ethylenediamine, trimethylenediamine, and triethylenetetramine were used as the shape controllers of the TiO_2 nanomaterials and to act as surfactants (Sugitomo et al., 2003). Furthermore, a combination of the sol-gel method and an anodic alumina membrane (AAM) template was used to synthesise TiO_2 nanorods successfully. This was accomplished by dipping the porous AAMs into a boiled TiO_2 sol followed by drying and heating processes (Miao et al., 2004).

In a typical experiment, a TiO_2 sol solution is prepared by mixing TTIP dissolved in ethanol with a solution containing water, acetylacetone, and ethanol. The AAM is immersed into the sol solution for 10 min after boiling in ethanol before subsequently drying in air and calcination at 400 °C for 10 h. The AAM template is removed in a 10 wt % H_3PO_4 aqueous solution. The calcination temperature can be used to control the crystal phase of the TiO_2 nanorods. At low temperature, anatase nanorods can be obtained while at high-temperature rutile nanorods are obtained. Therefore, the pore size of the AAM template can be used to control the size of the TiO_2 nanorods, which typically range from 100 to 300 nm in diameter and several micrometres in length. The size distribution of the final TiO_2 nanorods is largely controlled by the size distribution of the pores of the AAM template. To obtain smaller and monosized TiO_2 nanorods, it is necessary to fabricate high-quality AAM templates. Figure 2.10(a) shows a typical TEM for TiO_2 nanorods

fabricated with this method. Normally, the TiO_2 nanorods are composed of small TiO_2 nanoparticles or nanograins.

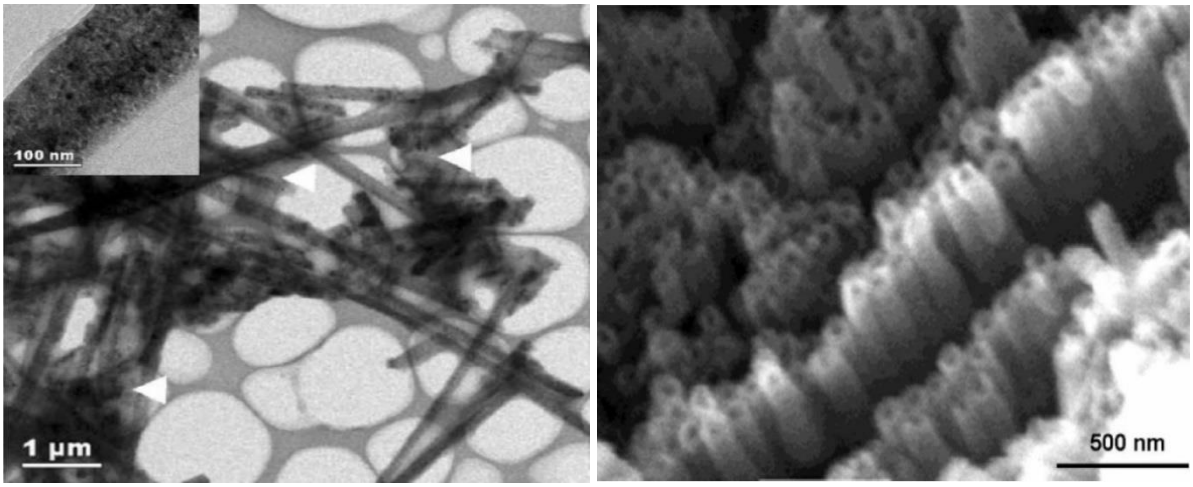

(a) (b)

Figure 2.10: Typical images of (a) TiO_2 nanorods fabricated with the sol-gel method and an anodic alumina membrane (AAM) template by TEM (b) TiO_2 nanotube array from the AAM template by SEM (Liu et al., 2013).

The TiO_2 nanotubes can also be obtained through the sol-gel method by templating with an AAM and other organic compounds (Chen and Mao, 2007). As reported by Liu et al. (2002), TiO_2 nanotubes could be obtained by coating the AAM membranes at 60 °C for a certain period (12-48 h) with dilute TiF_4 at pH = 2.1 and removing the AAM after TiO_2 nanotubes are fully developed. Figure 2.10(b) shows a typical SEM image of the TiO_2 nanotube array from the AAM template (Liu et al., 2002).

2.4.4 Applications of TiO_2

The existing and promising applications of TiO_2 nanomaterials include paint, toothpaste, and UV protection. Other applications include photocatalysis, photovoltaics, sensing, electrochromic and photochromics. Typically, TiO_2 nanomaterials have larger

band gaps (>3.0 eV) and high absorption, particularly in the UV region. Furthermore, TiO_2 nanomaterials are very stable, nontoxic, and cheap. The optical and biologically benign properties of the materials are suitable for UV protection applications (Mahltig et al., 2005; Hwang et al., 2003). In addition, the TiO_2 nanomaterials can be imparted with antifogging functions on various glass products, i.e., mirrors and eyeglasses that have superhydrophilic or superhydrophobic surfaces (Takata et al., 2003; Sirghi et al., 2003). TiO_2 nanomaterials have also been used as sensors for various gases and humidity due to the electrical or optical properties which change upon adsorption (Si et al., 2005).

One of the most important research areas for future clean energy applications is the search for efficient materials for the production of electricity or fuels such as hydrogen. When sensitized with organic dyes or inorganic narrow band gap semiconductors, TiO_2 can absorb light into the visible light region and convert solar energy into electrical energy for photovoltaic applications (Granqvist, 2003). For example, an overall solar conversion efficiency of 10.6% was reported by Grätzel (2004) by Dye-Sensitized Solar Cell (DSSC) technology. Currently, TiO_2 nanomaterials are widely applied for water splitting and hydrogen production due to their suitable electronic band structure given the redox potential of water (Chen and Mao, 2007). Another application of TiO_2 nanomaterials when sensitised with dyes or metal nanoparticles is to build photochromic devices (Kawahara et al., 2005; Biancardo et al., 2005). Undeniably, the utmost application of TiO_2 nanomaterials is the photocatalytic decomposition of various pollutants.

2.4.5 Photocatalysts and photocatalytic mechanism

Photocatalysis is the amalgamation of photochemistry and catalysis. The word “photocatalysis” is derived from the Greek language. It is composed of two parts; 1. The prefix *photo* means light, whereas *catalysis* is the process whereby a substance alters the

rate of a chemical transformation of the reactants without being altered in the reaction. The substance termed the catalyst, increases the reaction rate by reducing the activation energy (Saravanan et al., 2017).

Hence, photocatalysis is a process whereby light and catalysts are concurrently used to support or speed up a chemical reaction. Generally, photocatalysis can be defined as "a change in the rate of chemical reactions or their generation under the action of light in the presence of substances called photocatalyst that absorbs light quanta and is involved in the chemical transformations of the reactants" (Hagen, 2015). The photocatalysis process is classified into two categories: homogeneous and heterogeneous (Rajeshwar et al., 2008; Rehman et al., 2009). Most homogeneous photocatalytic processes are based on metal complex catalysts or transition metals complexes like iron, copper, chromium. However, semiconductor materials such as TiO_2, ZnO, SnO_2, and CeO_2 mainly act as heterogeneous photocatalysts. This is due to their favourable combination of electronic structures characterized by a filled valence band and an empty conduction band. These properties enhance the light absorption properties, charge transport characteristics, and a lifetime of the excited states (Rehman et al., 2009; Nakata and Fujishima, 2012; Khan et al., 2015).

Photocatalytic reactions primarily depend on the wavelength of light (photon), energy, and the catalyst. In general, semiconducting materials are used as a catalyst which also acts as sensitisers for the irradiation of light stimulated redox processes. This is due to their electronic structure, which is characterised by a filled valence band and a vacant conduction band (Hagen, 2006; Khan et al. 2015). The schematic representation of a typical semiconductor photocatalytic mechanism is depicted in Figure 2.11. The fundamental steps in the process of semiconductor photocatalysis are as follows (Hagen 2006; Rajeshwar et al. 2008; Rehman et al. 2009; Khan et al. 2015):

- When the light energy or photons fall on the surface of a semiconductor provided the energy of the incident ray is equivalent or greater than the band gap energy of the semiconductor, the valence band electrons are agitated and migrate to the conduction band of the semiconductor.
- Holes are created in the valence band of the semiconductor. These holes in the valence band can oxidise donor molecules and react with water molecules to generate hydroxyl radicals. The radicals have strong oxidising power responsible for the degradation of pollutants.
- The conduction band electrons react with dissolved oxygen species to form superoxide ions. These electrons induce the redox reactions. Next, these holes and electrons undergo successive oxidation and reduction reactions with any species, potentially adsorbed on the surface of the semiconductor to give the necessary products.

The photocatalytic activity of TiO_2 makes it an excellent material for various applications such as dye-sensitised solar cells, water purification, and anti-bacterial action. In the purification of water by degradation of organic pollutants, a photocatalytic material catalyses the photocatalytic reaction degradation of the pollutant in the presence of light. One such application involves the use of TiO_2 as a photocatalytically active material, whose properties can be triggered by light irradiation (see Figure 2.11). The TiO_2 can be used to destroy organic compounds, prevent fogging of glass, and split water into hydrogen and oxygen (Ibhadon and Fitzpatrick, 2013). As earlier mentioned, the main advantages of TiO_2 are its nontoxicity, relatively low cost and high oxidising power. Other properties include its high chemical stability when exposed to acidic and basic compounds. The outlined properties make TiO_2 a competitive candidate for many photocatalytic applications.

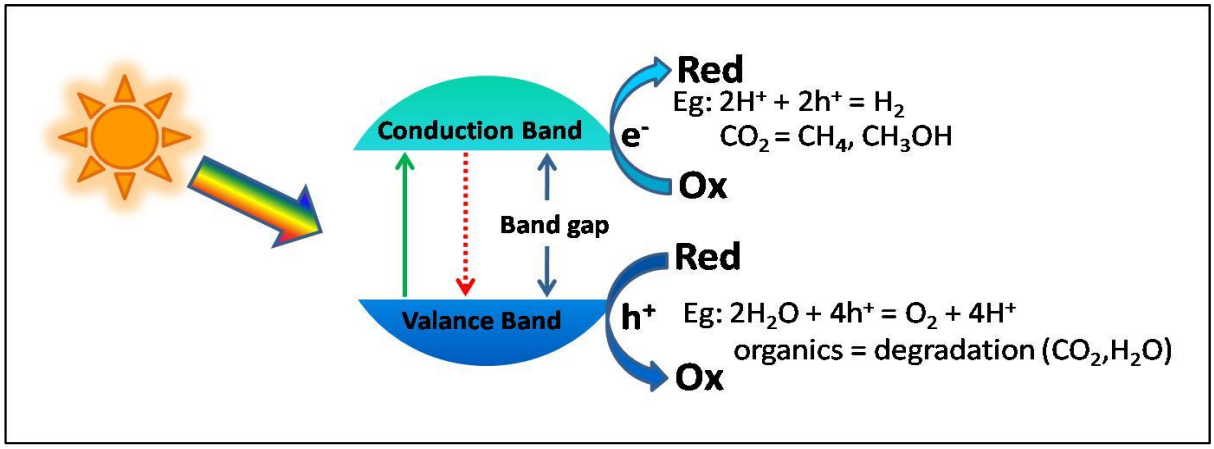

Figure 2.11: Schematic of the photocatalytic mechanism by semiconductor.

It has been recently found that the nano-sized materials (in the range 1–100 nm) exhibit different properties compared to their bulk variants. Therefore, nano-sized TiO_2 can be potentially used as a photocatalytic material for the oxidation of organic pollutants whose activity (chemical reaction rate) can be increased by increasing its surface area (Binas et al., 2017). A large surface area with a constant surface density of adsorbents leads to faster surface photocatalytic reaction rates. In this sense, the larger the specific surface area, the higher the photocatalytic activity. Conversely, the surface is a defective site; therefore, the larger the surface area, the faster the recombination. However, the higher the crystallinity, the fewer the bulk defects, and the higher the photocatalytic activity. The crystallinity of TiO_2 nanomaterials is improved by high-temperature treatment. This ultimately induces the aggregation of small nanoparticles, thereby decreasing the surface area. Judging from the above general conclusions, the relation between the physical properties and the photocatalytic activities is complex. Therefore, optimal conditions require taking these considerations into account, although these may vary case by case (Chen and Mao, 2007).

2.4.6 Photocatalysis parameters

Primarily, the rate of photo mineralization of an organic compound by photocatalysis depends on the following parameters: structure, shape, size, and surface area of the catalyst. Other important criteria include; reaction temperature, pH, light intensity, amount of catalyst, and concentration of wastewater (Rajeshwar et al. 2008; Rehman et al. 2009; Saravanan et al. 2011). The following are the related explanation of the catalyst parameters:

i) Crystal structure, shape, size, and surface area

The structure of catalyst plays a key role in achieving superior photocatalytic activity. For example, the TiO_2 material has three phases such as anatase, rutile, and brookite. However, the most sensitive and attractive is the anatase phase which has remarkable photocatalytic. This is due to its stability, conduction band location, a high degree of hydroxylation, and adsorption power (Khan et al., 2014; Gnanasekaran et al., 2015). Furthermore, morphology also acts as a potential factor that influences the final degradation efficiency, as reported earlier (Saravanan et al., 2011). Nanomaterials with small size and large surface areas have been compared with bulk materials to highlight their higher efficiency in photocatalytic reactions effectively. Compared to its bulk form, nanosized TiO_2 materials are more efficient for water purification and recycling due to their smaller size (Cernuto et al., 2011; Han et al., 2014). When the size of the catalyst is smaller, a huge number of atoms are accumulated on the surface of a catalyst which leads to increase in surface to volume ratio. This property enhances the number of active sites and interfacial charge carrier transfer rates, thereby achieving higher catalytic activities (Cernuto et al., 2011). Furthermore, the photocatalytic redox reaction occurs primarily on the surface of the photocatalysts. As a result, the surface properties significantly influence the efficiency of catalyst (Saravanan et al., 2013; Khan et al., 2015).

ii) Effect of reaction temperature

Numerous researchers have demonstrated the dependence of photocatalytic activity on reaction temperature (Rajeshwar et al. 2008; Malato et al., 2009; Rehman et al. 2009). The photocatalytic reaction of TiO_2 at temperatures above 80 °C enhanced the electron-hole recombination and desorption process of adsorbed reactant species resulting in decreased photocatalytic activity. The degradation rate dependency on temperature is reflected by the low activation energy (5–20 kJ mol^{-1}) compared with ordinary thermal reactions. Due to photonic activation, heat is not required for photocatalytic systems and can operate at room temperature. The optimum reaction temperature for photocatalytic activity of TiO_2 is reportedly in the range 20–80 °C. When the temperature is at 0 °C, there is an increase in the apparent activation energy. However, the optimum range mainly depends on the activation energy of the material in the photocatalytic reaction (Chatterjee and Dasgupta, 2005).

iii) Effect of pH

In the photocatalytic reactions, the pH of the solution is a vital factor, due to its influence on the surface charge properties of the photocatalyst. Furthermore, the change in pH affects the efficiency of degradation of organic pollutants (Castillo-Ledezma et al. 2011; Reza et al., 2017; Kazeminezhad and Sadollahkhani, 2016). The photocatalytic degradation of TiO_2 material for Reactive Blue 4 was examined under different pH conditions (Neppolian et al. 2002). The results clearly explained that the lower degradation efficiency in the acidic solutions (pH < 5) was due to the degradation of the dye and lagging by high proton concentration. However, in alkaline medium (pH > 10), the existence of hydroxyl ions defuses the acidic end products that are produced by the photodegradation reaction. Furthermore, an unexpected drop in degradation was detected in the alkaline range (pH=11–13) because the hydroxyl radicals (OH) were rapidly

scavenged preventing reaction with the dyes (Neppolian et al., 2002; Reza et al., 2017). The effect of pH on the rate of reaction can be interpreted in terms of electrostatic interactions between the charged particles and the contaminants. These influence the adsorption and subsequently the surface properties.

iv) Effect of light intensity

The degradation rate of photocatalytic reaction mostly depends on the light intensity. The quanta of light absorbed by any photocatalyst or reactant are given by the quantum yield which is the ratio of the rate of reaction to the rate of absorption of radiation. The result of the photocatalytic reaction was varied under different wavelengths of the light source (Malato et al., 2009; Reza et al., 2017; Chatterjee and Dasgupta, 2005; Akpan and Hameed, 2009). The TiO_2 catalyst has a large band gap (3.2 eV) which absorbs mostly in the UV region (Reza et al., 2017). The degradation reaction rate of TiO_2 varies for different intensities of light as follows; the reaction rate increases with increasing light intensity in the range of 0–20 mW/cm^2. In principle, the reaction rate depends on the square root of the light intensity (half order) above the certain value (~25 mW/cm^2) of intermediate light intensity. However, the reaction rate decreases at high-intensity light irradiation due to favourable recombination of the electron-hole. In addition, the excessive light intensity promotes further electron-hole recombination, thereby decreasing the reaction rate (Malato et al., 2009; Reza et al., 2017; Chatterjee and Dasgupta, 2005; Akpan and Hameed, 2009).

v) Effect of amount

The amount of catalyst also influences the efficiency of photocatalytic degradation. If there is an increase in the quantity of catalyst, the number of active sites on the semiconductor surface increases due to a higher generation of OH^- and O_2^- radicals (Malato et al., 2009; Rajeshwar et al., 2008). As a result, the rate of photocatalytic

degradation is increased. Konstantinou et al. (2004) elucidated that the degradation rate is directly proportional to the catalyst concentration in any reactor system. However, as the catalyst loading improves beyond an optimum concentration, the degradation rate becomes unfavourable. This is due to the decrease in the light penetration depth into the solution and consequently diminishing of light scattering occurs.

vi) Concentration of pollutants in wastewater

Another main factor that influences the degradation rate is the pollutant type and its concentration (Chatterjee and Dasgupta, 2005; Rajeshwar et al., 2008; Rehman et al., 2009; Malato et al. 2009). Many researchers have accounted for the photocatalytic activity under similar operating conditions using similar catalysts. However, the variation in the preliminary concentration of water contaminants results in different irradiation time required to attain complete mineralization (Chong et al., 2010; Rajeshwar et al., 2008; Rehman et al., 2009; Malato et al., 2009; Chatterjee and Dasgupta, 2005). Kiriakidou et al. (1999) reported that the TiO_2 material shows different efficiency under similar operating conditions at different concentrations of Acid Orange 7 (25–600 mg/L). The results indicated that complete degradation rate was achieved at 25–100 mg/L. However, the rate of degradation diminished at higher concentration of dye (200–600 mg/L) (Kiriakidou et al., 1999). This observation is in good agreement with several previous reports in the literature (Malato et al., 2009; Reza et al., 2017; Chatterjee and Dasgupta, 2005; Akpan and Hameed, 2009).

2.4.7 Advantages and limitation of photocatalysis

As known, photocatalytic technology has their specific advantages as well as limitations. The advantages of photocatalysis are as follows (Nakata and Fujishima, 2012; Rajeshwar et al. 2008; Rehman et al., 2009):

i) Photocatalysis offers a good replacement for the energy-intensive ultrafiltration, reverse osmosis, coagulation by chemical agents, ion exchange on synthetic adsorbent resins) with potential applications in renewable and pollution-free solar energy.

ii) Photocatalysis leads to the formation of harmless products, unlike conventional treatment measures that transfer pollutants from one phase to another.

iii) The photocatalytic process can be used in the destruction of various hazardous compounds in different wastewater streams.

iv) The reaction conditions for photocatalysis are mild, the reaction time is modest, and requires less chemical input.

v) There is minimal secondary generation of wastes.

vi) It can be applied to hydrogen generation, gaseous phase, and aqueous treatments as well for moderate solid (soil) phase treatments.

However, the limitations of photocatalytic activity depend on the following (Rehman et al., 2009; Rajeshwar et al., 2008):

i) Interfacial charge transfer.

ii) Improving the charge separation.

iii) Inhibition of charge carrier recombination.

These are essential for enhancing the efficiency of the photocatalytic process.

CHAPTER 3

METHODOLOGY

3.1 Experimental work

In this chapter, all experimental work will be explained precisely with a comprehensive methodology as well as approaches to fulfil the defined objectives. There are two (2) stages of experimental work which will be accomplished in this study namely:

i. Deposition of IZO onto kenaf fibres hereafter called KF-IZO by dip-coating process.

ii. Nanostructured tubular TiO_2 synthesis using kenaf fibres as a sacrificial template.

In stage 1, the alkalization process of kenaf fibres, surface modification and increasing their adhesion properties be will be described. The detailed explanation of the dip coating (deposition) process with the precursor solution IZO will also be defined. Next, the procedure for producing the precursor solution used in the study will be presented. The experimental techniques used to determine the electrical conductivity by four probe methods with line contact attachment will be highlighted. The qualitative and quantitative analysis by SEM/EDX and its morphology will also be shown for a clearer determination of KF-IZO. The detailed flow of experiment 1 is illustrated in Figure 3.1.

In stage 2, the experimental works will cover details of how the non-woven kenaf mat was used as a template for the deposition of titanium (IV) isopropoxide (TTIP) precursor for the synthesis of TiO_2 in a tubular form. The acquired material was

characterised by various testing and analysis. Next, the performance of tubular TiO_2 was assessed for its photocatalytic activity. All the experimental works involved in this study are explained comprehensively including sol-gel techniques for producing TTIP precursor solution, dip-coating process, calcination process, performance test and all related process. The detailed flowchart for experimental 2 is given in Figure 3.2.

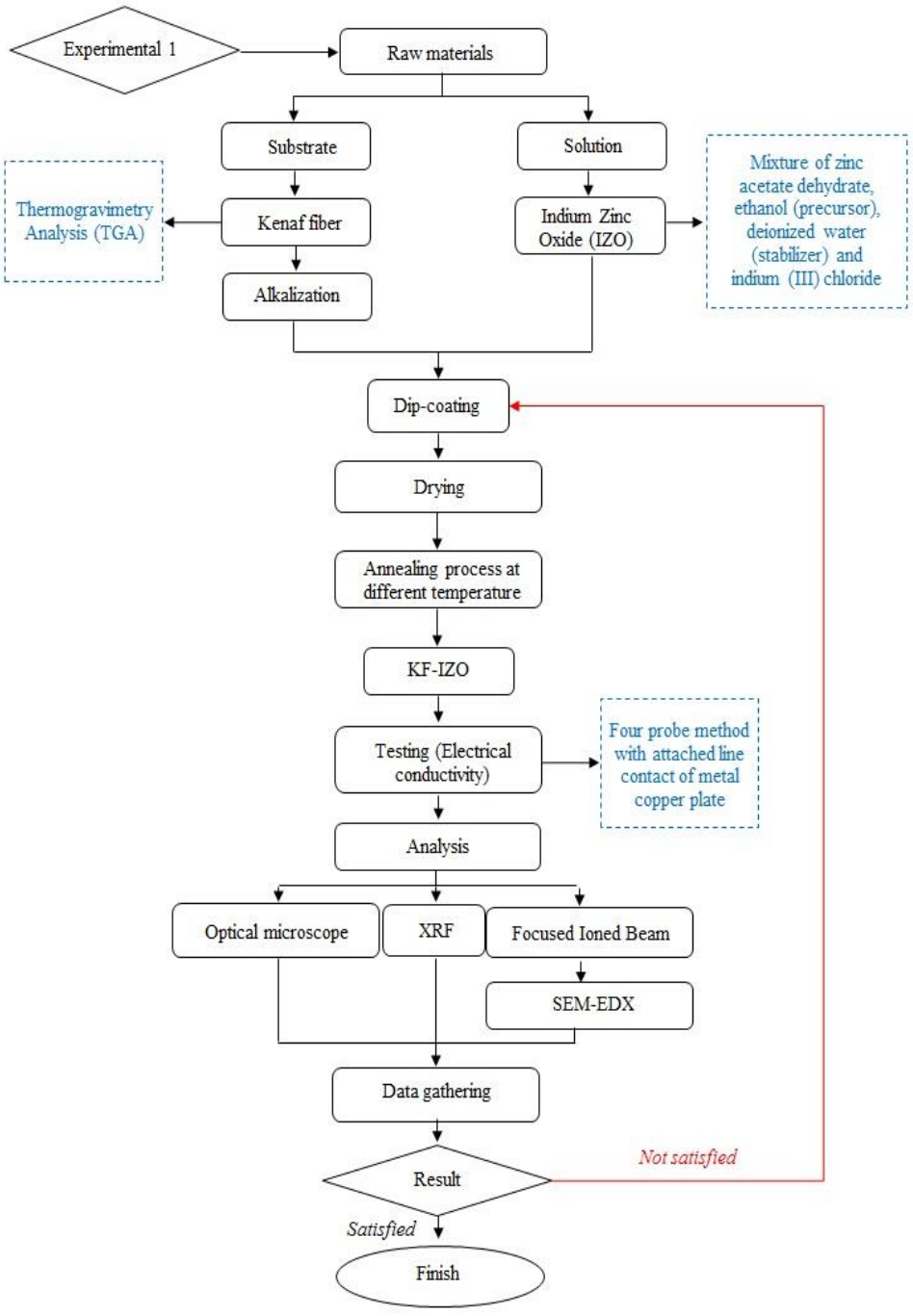

Figure 3.1 Process flow for experimental 1.

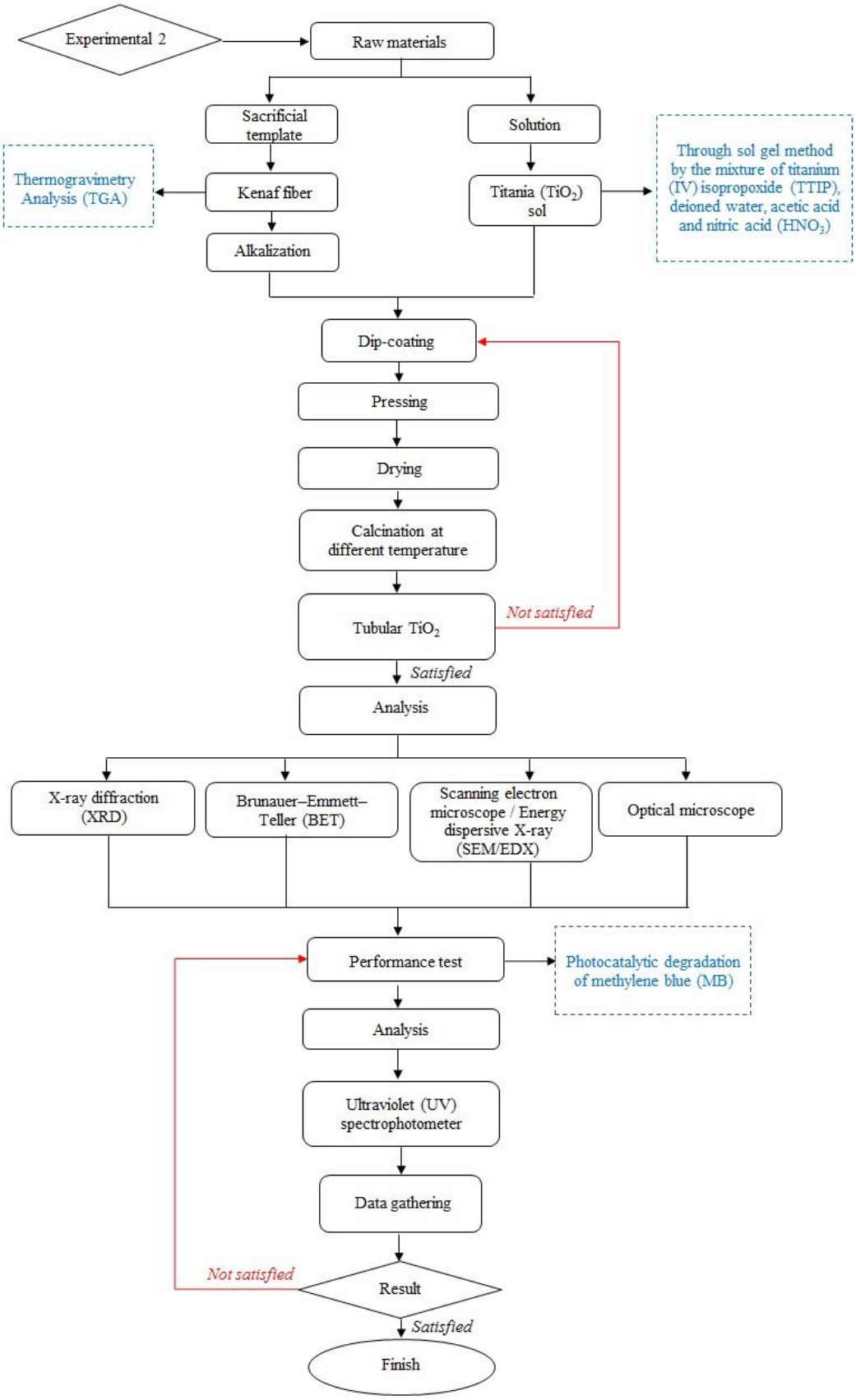

Figure 3.2: Process flow for experimental 2.

3.2 Alkalization process

The contact ability of kenaf fibres with a hydrophobic material can be enhanced by alkalization. As known, alkaline treatment is the easiest surface treatment technique for natural fibres like kenaf, jute, bamboo, hemp and others. In this study, kenaf bast fibre with randomly oriented mats and a surface density of 800 g/m^2 was used. Figure 3.3 shows SEM images of the as-received KFs. The average diameter of the KF is in the range 50 – 70 µm. The raw KF mat was alkalized with 5% sodium hydroxide (NaOH) solution to eliminate the natural grease, pectin, lignin, and stains present in it. The alkalization process was performed for 48 h by immersing the raw KF mat in the NaOH solution. Next, the mat was rinsed with deionised water 5 times followed by drying at 70 °C for 24 h. As a result, the alkalized KF shows a significant difference compared to the raw (untreated) KF as presented in Figure 3.4 (a) and (b).

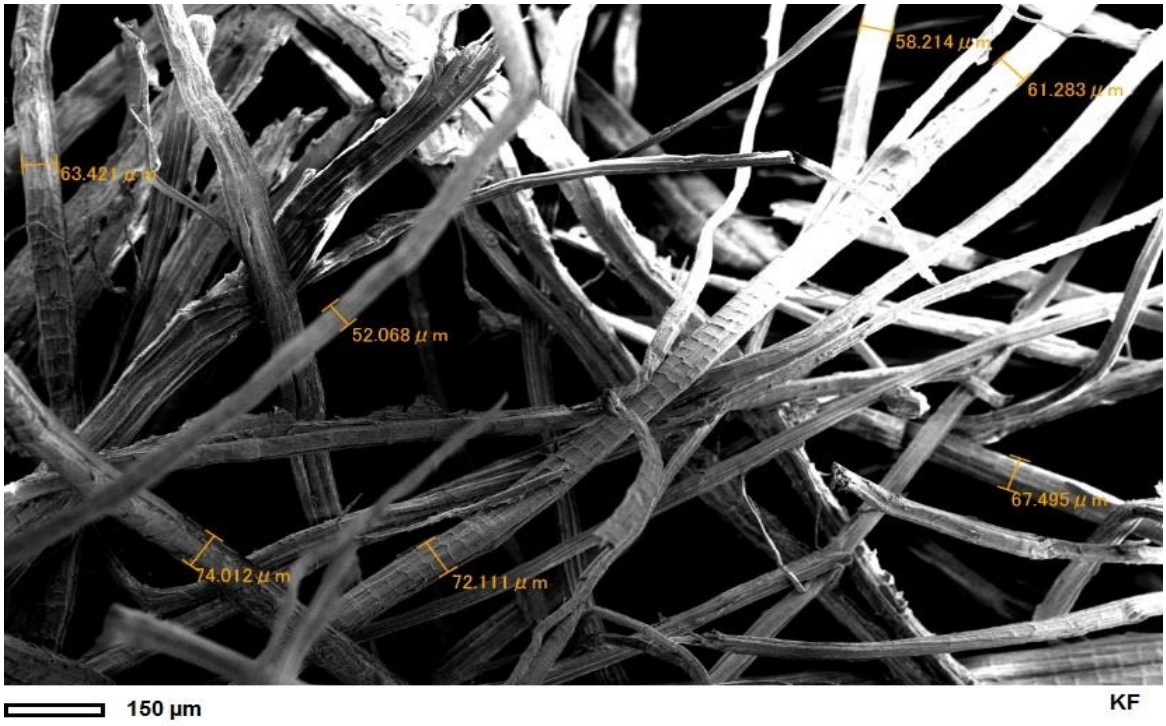

Figure 3.3: SEM images of the as-received KFs (obtained at a magnification of 60×).

(a) (b)

Figure 3.4: Non-woven kenaf fibres; a) KF before alkaline treated: corrupted and fungi, b) KF after alkaline treated: clean, shiny surfaces and free of impurities (10x Magnification).

3.3 Preparation of Indium zinc oxide (IZO) precursor solution

The IZO solution was prepared with an In/Zn ratio of 6%. The IZO solution was prepared by adding 3 g of zinc acetate dehydrate (≥98% purity, supplied by Aldrich Chemical) and dissolving in 100 ml of ethanol (99.5%, supplied by Kanto Chemical). Next, the mixture was magnetically stirred at a speed of 700 rpm for about 1 h at 25 °C. During the process, about 1 ml of deionised water, which acted as a stabiliser, was dropped into the mixture by a syringe. Once the dissolution was complete, 0.15 g of indium (III) chloride (98% purity, supplied by Aldrich Chemical) was added to the solution, as a dopant material. The resulting mixture was subsequently stirred for 1 h at 75 °C. In the end, a clear and homogenous solution of IZO was obtained. Figure 3.5 shows a schematic process flow for the preparation of IZO. The Zinc Acetate Dehydrate dissolved in ethanol by a magnetic stirrer (700rpm) for 1 h at 25 °C. Pour with Indium (III) Chloride and continued stirred (700rpm) for 1 h at 75 °C. After the process was completed, clear and homogenous of IZO solution was obtained.

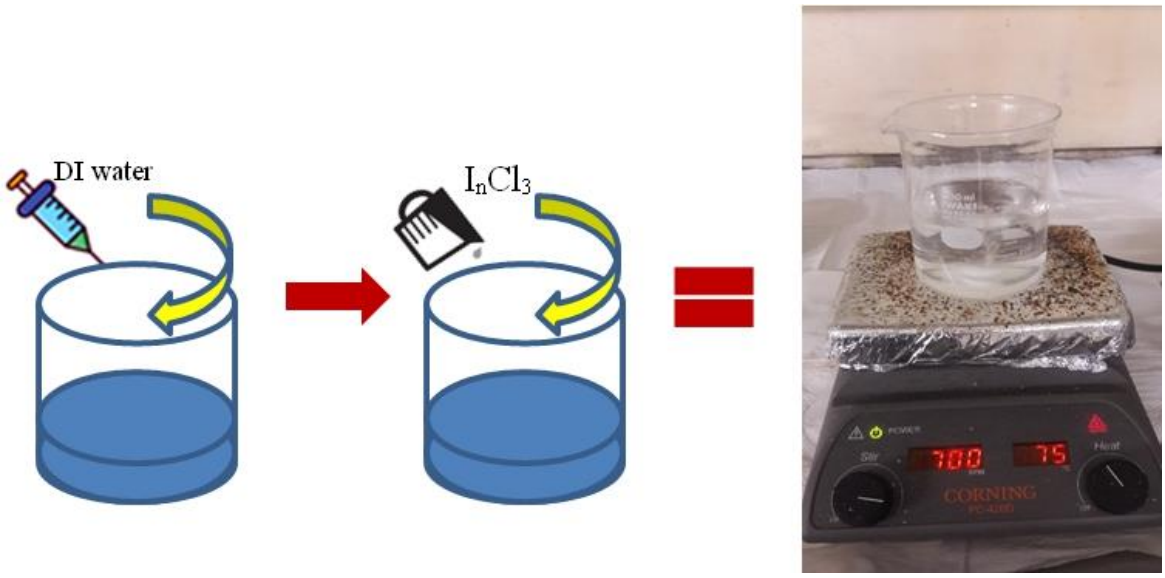

Zinc Acetate Dehydrate dissolved in ethanol by magnetic stirrer (700rpm) for 1 h at 25 ◦C

Pour with Indium (III) Chloride and continued stirred (700rpm) for 1 h at 75 ◦C

Clear and homogenous of IZO

Figure 3.5: Schematic of a process flow for IZO preparation.

3.4 Preparation TiO_2 solutions

The TiO_2 solution was prepared with a mixture of 10 mL titanium (IV) isopropoxide (TTIP) (97% purity, supplied by Aldrich Chemical) and 10 mL of acetic acid (≥99.8% purity, supplied by Aldrich Chemical). In addition, 100 mL of distilled water was added to the reaction mixture to accelerate the hydrolysis reaction. The desired pH range of the solution (4–6) was achieved by adding 1 mL of nitric acid (HNO_3). The resulting mixture was stirred with a magnetic stirrer for about 16 h at 60 °C until a whitish blue colloidal suspension with high viscosity was produced. Figure 3.6 shows the process flow for preparing the TiO_2 colloidal suspension.

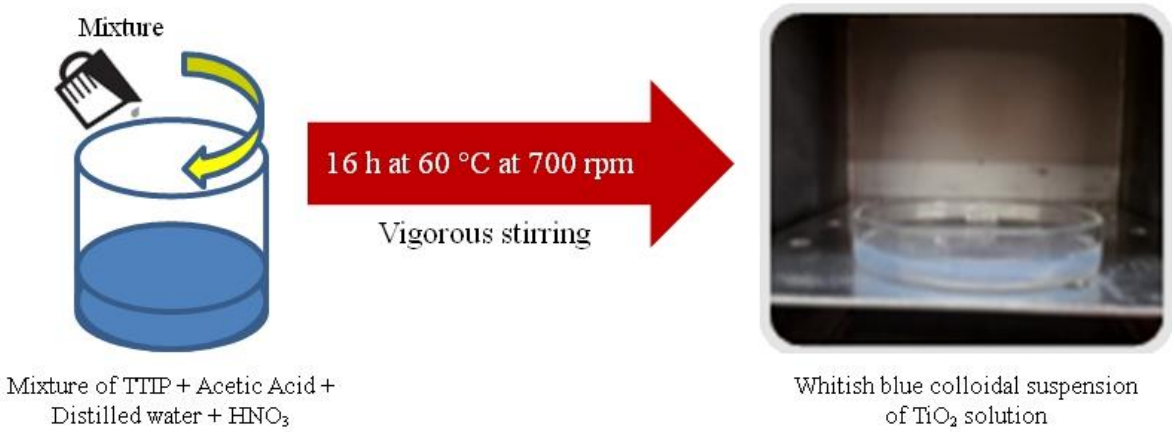

Figure 3.6: Schematic of a process flow for TiO_2 preparation.

3.5 Dip-coating process

The simplest and easiest method for preparing KF-IZO and tubular TiO_2 were selected and applied in this study. The dip-coating method is an economical, fastest and easy method to handle as compared to other sophisticated methods like chemical vapour deposition, hybrid method among others in the literature. The dip-coater (DC4300, Aiden) was used to perform the dipping process. The hanging height of samples was set up at 50 mm above the solution (Figure 3.7).

3.5.1 KF-IZO deposition

To produce the KF-IZO, the IZO was deposited on the KF using a dipping method at 25 °C at a dipping rate of 1–30 mm/s (1, 3, 5, 7, 9, 15, 20, and 30 mm/s). After deposition, the KF-IZO was dried followed by annealing at 150, 175 and 200 °C for 4 h in a vacuum furnace. For the effect of annealing time on the resistivity of KF-IZO after the deposition, the KF-IZO was dried at 120 °C followed by an annealing process at 150 °C for 2, 4, 8 and 16 hours in a vacuum furnace.

3.5.2 TiO_2 deposition

To perform TiO_2 coating, a KF mat with a mass of about 0.5 g and dimensions of 2.5×2.5 cm was dipped in the precursor solution for 1 min. Next, it was pressed at an applied force of 2.5 kg/cm^2 (36 psi) for 30 s to squeeze the excess of TiO_2 precursor out of the mat. Figure 3.3 shows the setup diagram of the dip-coating process applied in this study. Afterwards, the treated KF mat was dried at 90 °C for 3 h followed by the stepwise heating to 500, 600, 700, and 1000 ◦C for 4 h at each temperature to burn and completely remove any remaining KF species.

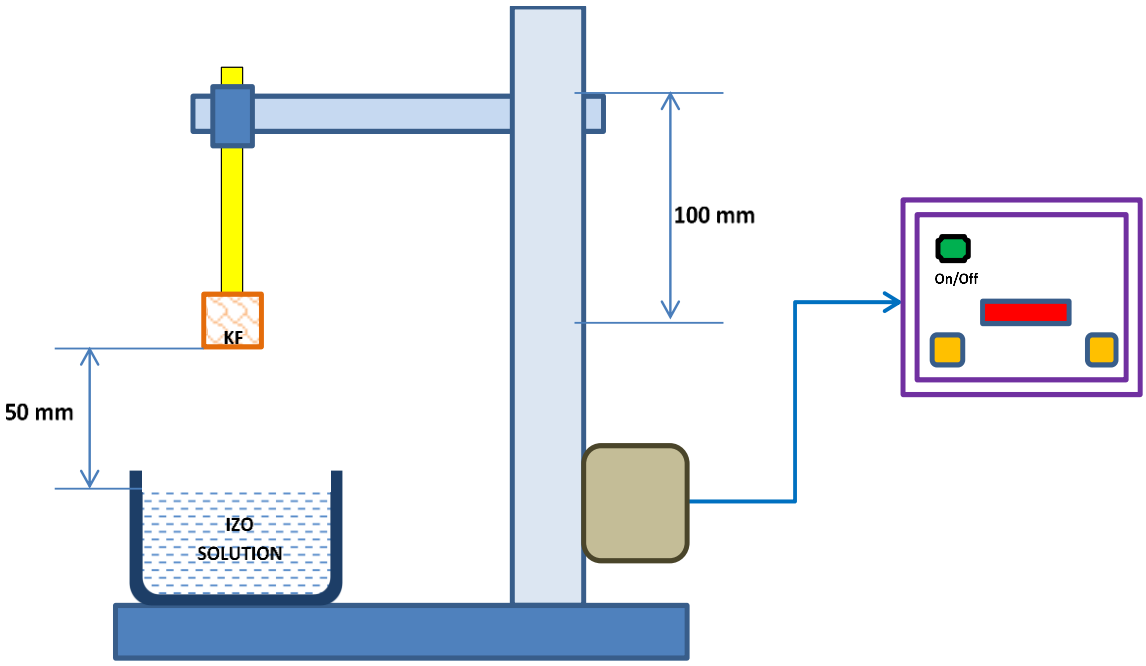

Figure 3.7: Schematic diagram of the dip-coater setup.

3.6 Testing and Analysis

3.6.1 KF-IZO

In this study, KF-IZO was further analyzed through X-Ray fluorescent (XRF), optical microscope and Scanning Electron Microscope / Energy Dispersive X-Ray (SEM/EDX).

i) XRF

XRF (X-ray fluorescence) is a non-destructive analytical technique used to determine the elemental composition of materials. XRF analysers determine the chemistry of a sample by measuring the fluorescent (or secondary) X-ray emitted from a sample when it is excited by a primary X-ray source. Each of the elements present in a sample produces a set of characteristic fluorescent X-rays ("a fingerprint") unique for that element. This is why XRF spectroscopy is an excellent technology for the qualitative and quantitative analysis of material composition. Therefore, KF IZO was examined through the XRF, Rigaku Supermini 200. The purpose of XRF analysis is to detect the initial presence of In^{3+} and Zn^{2+} elements in KF-IZO. Subsequently, it is used to calculate the ratio of In/Zn which plays an important role in determining the electrical properties of KF-IZO.

ii) Optical microscope

The optical microscope images for macrostructure analysis of KF-IZO were observed by MORITEX–Scopemen. Various magnification levels were adjusted to capture better images. The optical microscope is capable of detecting any imperfections in the KF-IZO in millimetre scale. Hence, imperfections such as agglomeration, segregation, and coating condition can be detected under this equipment. The analysis is thus required to ensure the quality and condition of IZO thin film is well-coated and distributed appropriately among the fibres.

iii) SEM-EDX

For the KF-IZO morphology, SEM images were used for initially detecting IZO thin layer and its existence on the KF surfaces. Furthermore, the thickness IZO thin films built on KF surfaces was predicted. Next, KF-IZO was analysed through SEM/EDX with three (3) surface analyses that are i) Point/Area analysis, ii) Elemental mapping analysis,

and iii) Line profile analysis. All tests were determined to confirm the IZO thin films covered the KF surfaces. In this study, a focused ion beam (FIB) was used to cut the KF cross-section, which was then scanned by SEM/EDX (JEOL, JSM-6510A). This was done with an acceleration voltage of 10 kV to reveal the coating condition and provide elemental identification and quantitative compositional information. Technically, a focused ion beam (FIB) instrument is almost identical to an SEM but uses a beam of ions rather than electrons. The focused ion beam can directly modify or "mill" the specimen surface, through the sputtering process, which is controlled with nanometer precision. Figure 3.8 presents the images before and after FIB cutting. The red dash rectangular box shows where the cutting is performed. The machine JEOL, JEM9320FIB with acceleration voltage 30 kV has been using to run KF-IZO cross-sectional cutting.

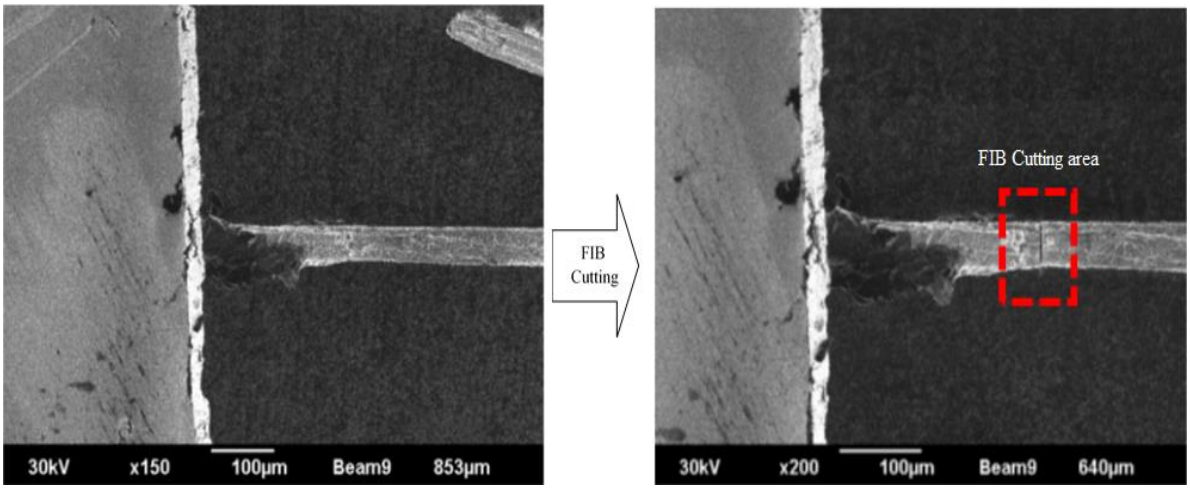

(a) (b)

Figure 3.8: KF-IZO single fibre FIB cutting as sample preparation for SEM/EDX analysis; (a) Before FIB (b) After FIB.

3.6.2 Tubular TiO_2

The resultant tubular TiO_2 were further examined and analysed using TGA, BET, XRD and SEM/EDX analysis techniques. The following is the detailed explanation of the tubular TiO_2 examined and analysed:

i) Thermogravimetric Analysis (TGA)

TGA measures the weight loss (%) of a test sample while the sample is heated at a uniform rate in an appropriate environment. The loss in weight over specific temperature ranges provides an indication of the composition of the sample, including volatiles and inert filler, as well as indications of thermal stability. In this study, the TGA was performed on the DTG-60 series from Shimadzu. The TG analysis was performed to identify the behaviour of kenaf towards the temperature especially thermal decomposition and degradation. This is essential because the KF will undergo annealing process and temperature is a major concern in the development of IZO thin films. Secondly, TGA was used to analyse the behaviour of KF at high temperature. Therefore, the thermal decomposition and degradation for complete removal of KF were identified. For both, TGA temperature profile as illustrated in Figure 3.9 was utilised.

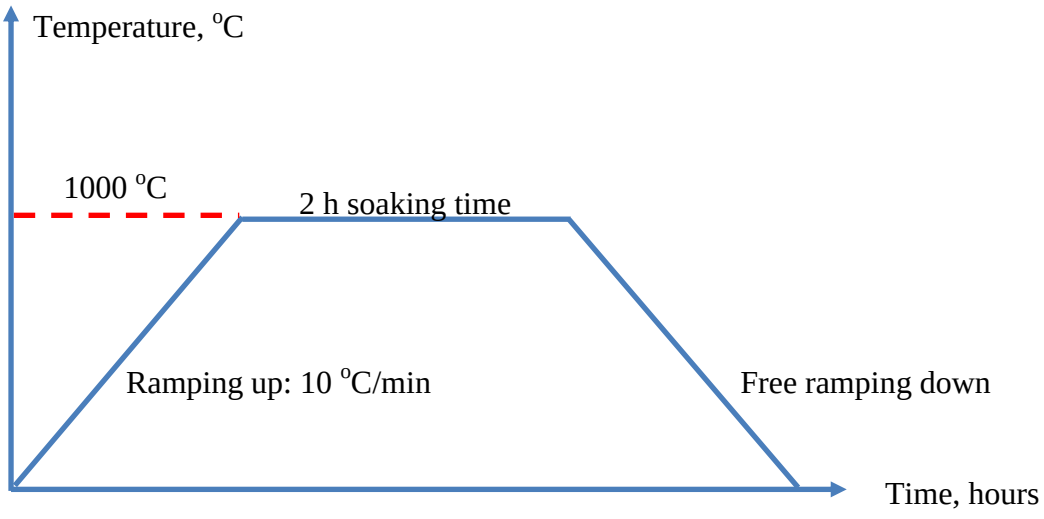

Figure 3.9: TGA temperature profile.

During the test, the inert (N_2) and oxidative (O_2) gas flow rates were set to provide the appropriate environments for the test. The test material was placed in the specimen holder (aluminium) before raising the furnace temperature. The initial weight reading was set to 100% before initiating the heating program. The gas environment was preselected for inert thermal decomposition (nitrogen gas) and oxidative decomposition (air or oxygen). The amount of sample tested was in the range of 5 - 10 mg.

ii) Brunauer–Emmett–Teller (BET)

The theory of BET aims to explain the physical adsorption of gas molecules on a solid surface. As such, it serves as the basis for an important analysis technique for the measurement of the specific surface area of materials. The BET technique is also the most commonly used method for determining the surface area of powders and porous materials, which involves nitrogen adsorption measurements. In this study, the Dollimore-Heal method was used to obtain the pore size distributions of tubular TiO_2 after heating to 500, 600, and 700 °C. Generally, nitrogen gas (N_2) is utilised as a probe molecule, which is adsorbed on the surface of the studied solid under cryogenic conditions (corresponding to a temperature of 77 K in this work). The surface area of the solid is estimated from the measured monolayer capacity and cross-sectional area of the probe molecule, which is equal to 16.2 $Å^2$ in the case of nitrogen.

iii) X-Ray Diffraction (XRD)

XRD is a rapid analytical technique primarily used for phase identification of a crystalline material, which provides information on unit cell dimensions. The analysed material is finely ground, homogenised, and average bulk composition is determined. Hence, SmartLab Intelligent X-ray Diffraction (XRD) System by Rigaku Co was used to characterize the tubular TiO_2. The tubular TiO_2 was calcined at stepwise heating at; 500, 600, 700 and 1000 °C before XRD analysis to determine its crystalline

structure and phase changes from anatase to rutile. Similarly, the XRD technique was utilised to examine the crystallinity and crystallite sizes of the produced tubular TiO_2 samples.

iv) SEM/EDX

For the tubular TiO_2, SEM was utilised to capture the tubular TiO_2. An SEM with an acceleration voltage of 5 to 10 kV was used for the analysis. SEM images of the tubular TiO_2 that replicated kenaf fibre form at different calcination temperatures were revealed. The phase changes of the tubular TiO_2 nanostructured wall from anatase to rutile due to calcination were also identified. Meanwhile, SEM/EDX by point/area analysis was performed to characterise the tubular TiO_2 synthesised through the kenaf template-assisted sol-gel method. Furthermore, atomic fractions of various elements in tubular TiO_2 were determined through SEM/EDX.

3.7 Performance Testing

3.7.1 Electrical properties of KF-IZO

The electrical properties of KF-IZO were measured by a four-probe method (Hewlett Packard 34401A multimeter with Advantest R6144 voltmeter) using a copper metal attachment plate. This attachment acted as the line contact between the adjacent fibres along the KF-IZO surface area. The distance between the two plates was 2.5 mm. The schematic diagram of electrical conductivity test by the four probe method is presented in Figure 3.10. However, Figure 3.11 shows schematic cross-sectional of the copper metal attachment plate.

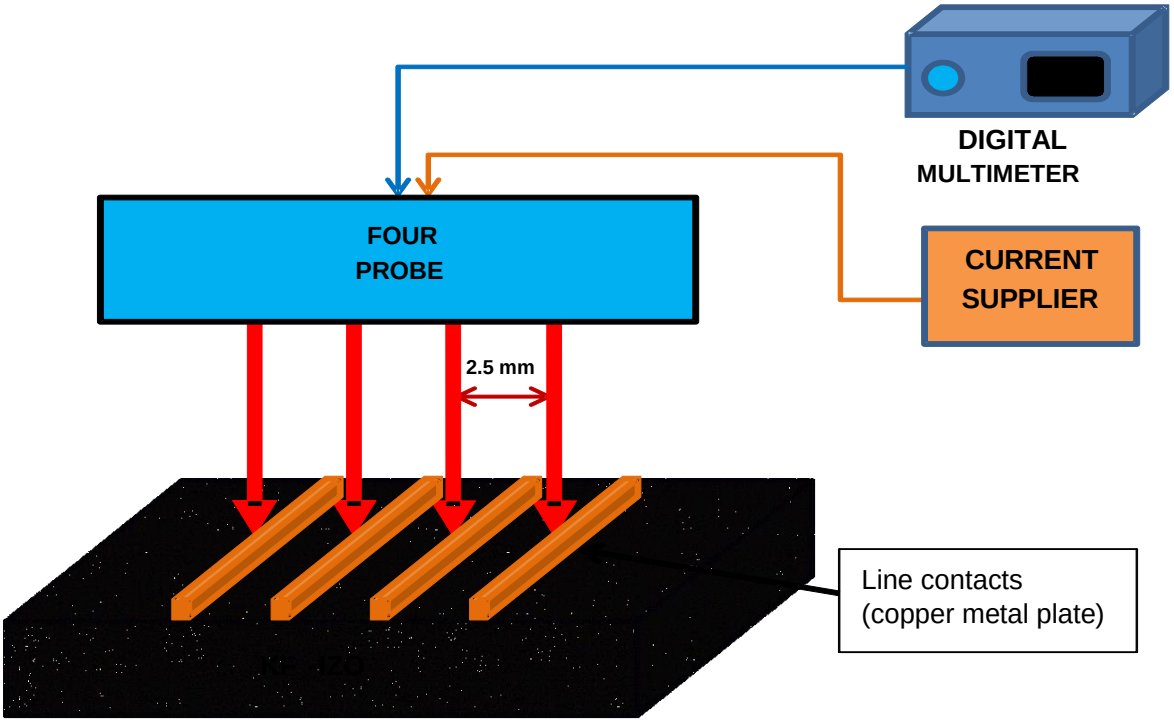

Figure 3.10: Schematic diagram of electrical conductivity test by four probe method.

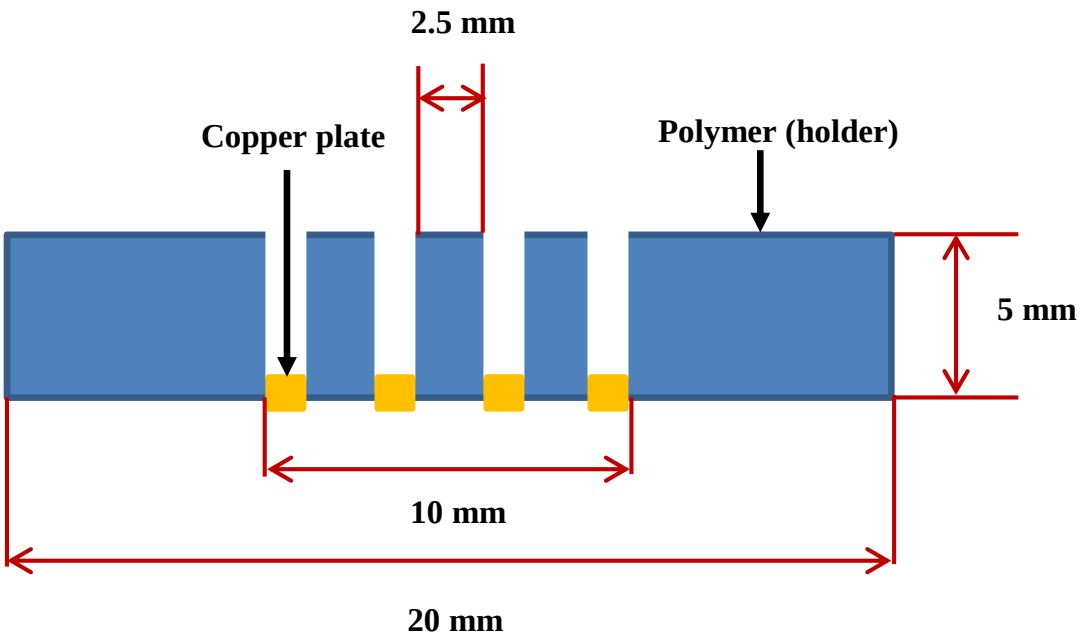

Figure 3.11: Schematic diagram of cross-sectional of copper metal attachment.

Electrical properties of KF-IZO were measured by using the following equation:

Resistivity, $\rho = R (A/L)$

Hence,

Conductivity, $\sigma = 1/\rho$

Or **$\sigma = L / (R \times A)$**

Electrical properties of KF-IZO were measured using the following equation:

S1 unit of conductivity is Siemens per metre (S/mm)

Legend:

R = Electrical resistance (ohm)

L = Length of the sample (mm)

A = Cross-sectional area of the sample (mm^2)

3.7.2 Photocatalytic test of tubular TiO_2

The solution of methylene blue (MB) in water with a mass ratio of 1:500 was used to evaluate its photocatalytic degradation in the presence of TiO_2 (the mass ratio between TiO_2 and the MB solution was 1:300). The two materials were mixed thoroughly for 15 min using a magnetic stirrer to allow the absorption and desorption processes to proceed to completion. The procedure was performed under dark conditions to prevent any unwanted photocatalytic processes. After 15 min of stirring, the MB solution was exposed to the UV irritation with a wavelength of 365 nm. Figure 3.12 presents the set up for the photocatalytic test of tubular TiO_2 which was designated by ISO 10678:2010 (Mills, 2012). During the first 2 h, the solution was periodically examined every 30 min with an ultraviolet (UV) spectrophotometer (JASCO, model V-670) to monitor possible changes in the transmission of MB. Finally, the MB solution was exposed to UV irradiation for 24 h to complete the cycle and determine the photocatalytic activity of tubular TiO_2.

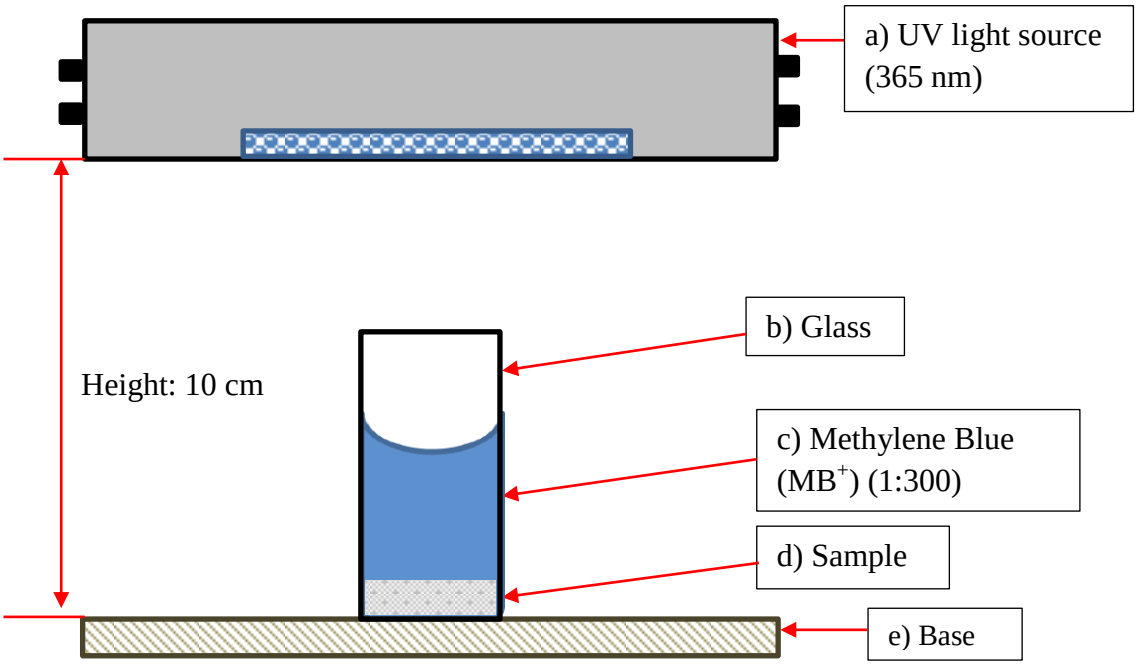

Figure 3.12: Schematic illustration of the Methylene Blue (MB^+) ISO 10678:2010.

CHAPTER 4

RESULT AND DISCUSSION – STUDY OF MORPHOLOGY AND ELECTRICAL PROPERTIES OF KF-IZO

4.1 Introduction

This chapter will analyse and discuss effects of dipping rate and the annealing process on the electrical properties (conductivity and resistivity) on the synthesized KF-IZO.

4.2 KF characterization

Initially, alkalization was used to enhance the interface adhesion between the KF substrates and the alkoxide groups. Alkalization is among the most effective chemical treatment for kenaf fibre (KF). Several researchers have reported improvements in the mechanical properties of cellulose fibres when alkalized at different NaOH concentrations (Gassan and Bledzki, 1999; Sreekala, 1997). The optimum alkali treatment is a low-cost and effective surface modification and treatment process for natural fibres (Ramesh, 2016). As referred to Table 4.1, the process washed out about 25.20 % of the impurities like wax, pectin, and lignin present in untreated KFs.

Table 4.1: Percentage of yield and impurities after alkaline treatment.

Alkaline Treatment	Kenaf fibre			
	Before (Avg. wt)	After (Avg. wt)	Yield	Impurities
5% NaOH at 48 h immersed	94.25 g	70.50 g	74.80 %	25.20 %

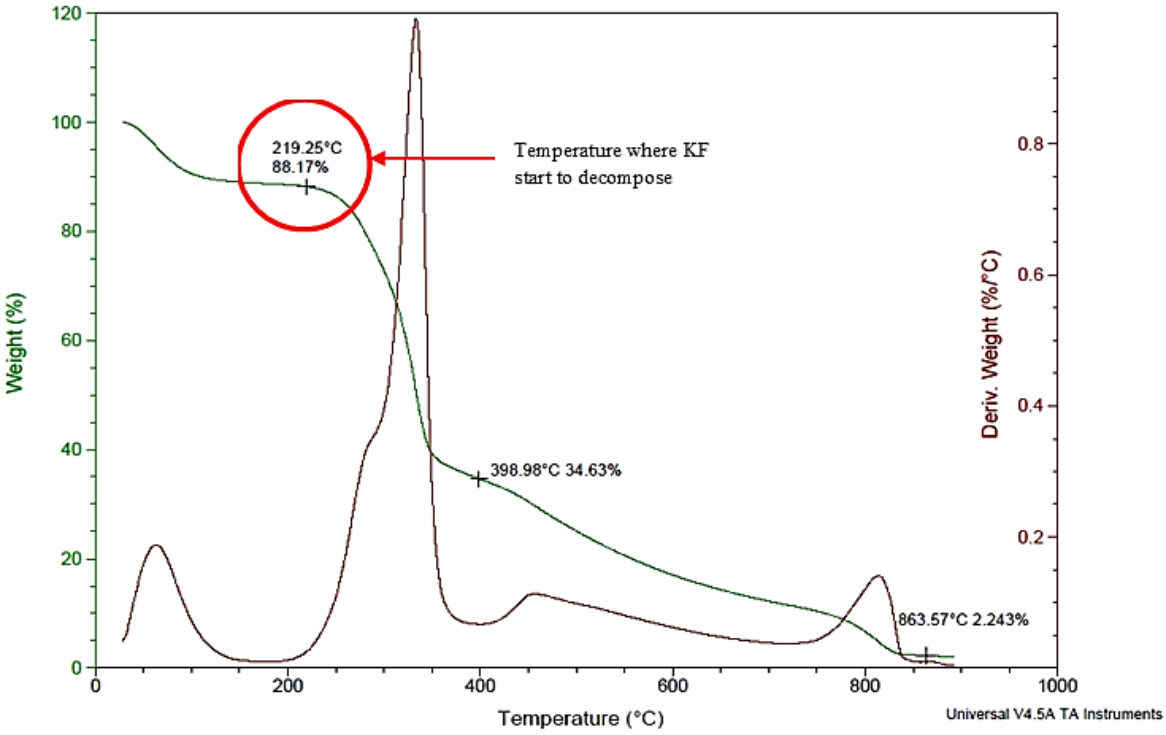

Figure 4.1: TGA result for raw KF.

One of the limitations of natural fibres is thermal instability. To avoid decomposition or degradation by high-temperature processing, the processing temperature is limited to 200 °C and short time duration (Wielage et al., 1999). The KF decomposition results show that about 4–11 % of the total KF weight was lost at temperatures in the range of 150–200 °C. The TGA results show that the KFs were strongly decomposed at 220 °C and the weight of the remaining KF sample was 88 % of the initial weight as

referred to Figure 4.1. Hence, natural fibres, which are low-temperature application resources should be annealed at low temperatures (≤ 200 °C).

4.3 KF-IZO thin film

The surface morphology of the KF-IZO thin film was examined to confirm the presence of IZO. Figures 4.2 and 4.3 show the appearance of KF-IZO under SEM and an optical microscope, respectively.

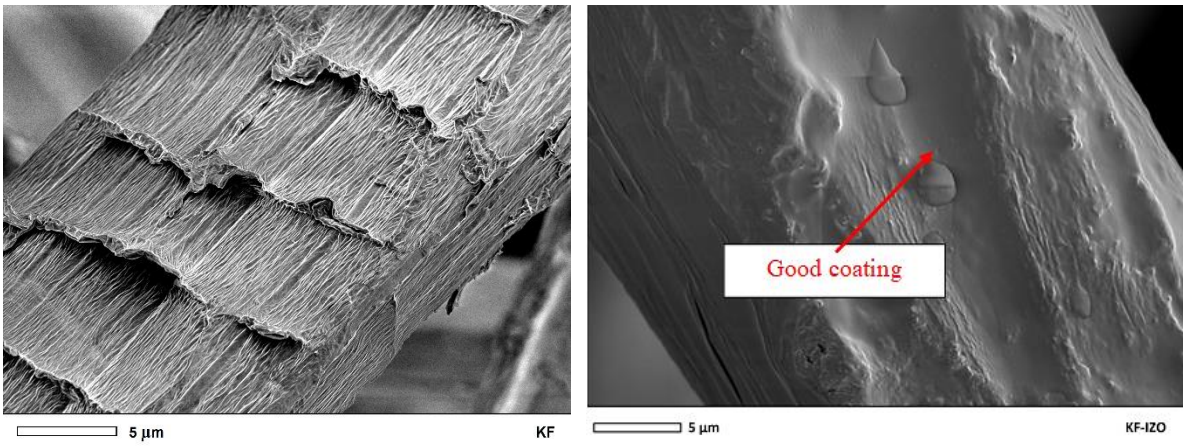

(a) (b)

Figure 4.2: SEM images for a single KF-IZO fibre **(a)** before IZO coating **(b)** after IZO coating at an annealing temperature of 150 °C.

It is seen that the appearance of KF-IZO is shiny with smooth surfaces compared to raw KF as referred to Figure 4.3 (b). It is strongly believed that this appearance is an indication of a good coating of indium (In) and zinc (Zn) around KFs. This could be responsible for the good electrical conductivity properties of KF-IZO. Moreover, it is greatly distributed along the KF fibre without any area lacking the IZO thin film. Furthermore, the thin film condition is free from agglomeration and segregation effects meaning that the IZO thin film was well distributed on the surface of KF.

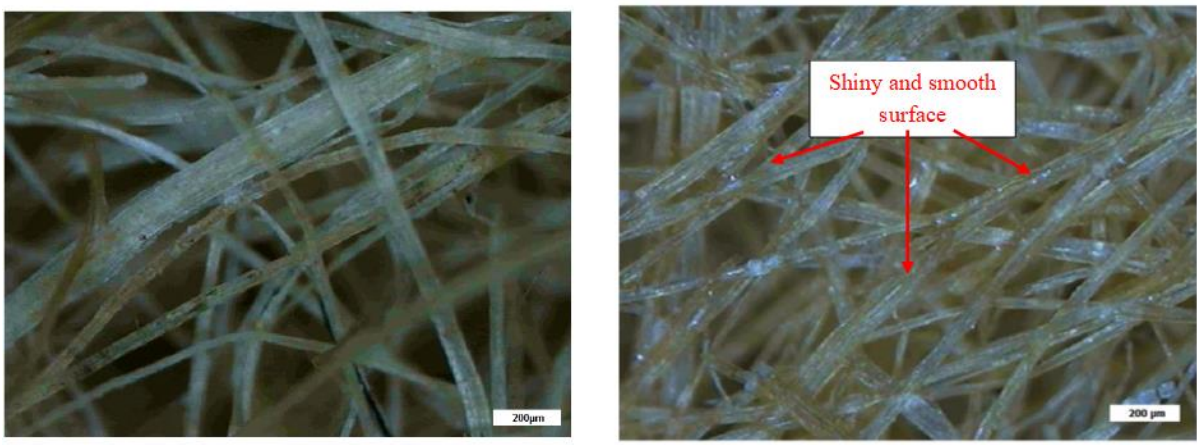

(a) (b)

Figure 4.3: Optical microscope image (MORITEX–Scopemen series with 166× magnification) of KF-IZO **(a)** before IZO coating **(b)** after IZO coating at an annealing temperature of 150 °C.

4.3.1 Surface analysis

To ensure the homogeneity of the IZO thin film, the surface analysis was performed to examine the IZO distribution on the KF substrates by SEM/EDX. The analysis includes i) Point/Area analysis, ii) Elemental mapping analysis and iii) Line profile analysis.

i) Point/Area analysis

Ideally, the EDS unit possesses the ability to pinpoint features within a field of view and gather a spectrum based upon a variety of user demands. The point scan allows the user to concentrate the X-Ray collection on a singular point within a field of view. Multiple point scans may be gathered in quick succession to compare the data. These collected spectra may then be overlaid onto one another to analyse the differing elemental constituents found at various locations. The same type of analysis may be taken of a circular, rectangular, or a user-drawn area to obtain information from a larger location.

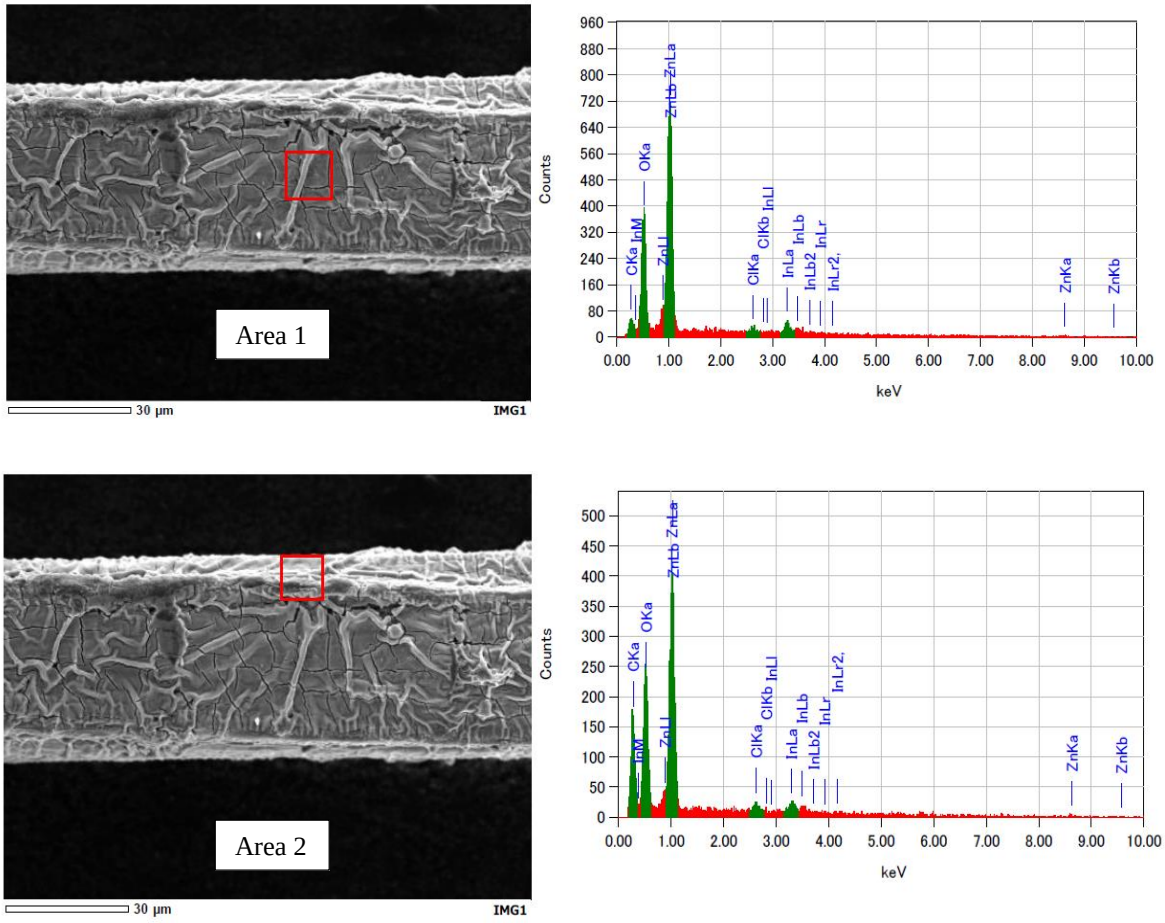

Figure 4.4: SEM/EDX area analysis for the area (1) and (2) of the side KF-IZO surfaces.

In this study, point/area analysis was performed along the fibre side of KF-IZO. The surface area 1 and 2 was further analysed as referred to Figure 4.4. The areas marked red in Figure 4.4 are two (2) specific surface area of KF-IZO, which were further investigated by SEM/EDX. The In/Zn ratios were 6.4% and 5.66%, respectively at a dipping rate of 5 mm/s. Furthermore, the In/Zn ratio was similar to that used for preparing the IZO solution which is 6.4% (Area 1) and 5.66% (Area 2). Hence, it can be surmised the IZO film was uniformly coated around KF. As reported by El Yamny and Rafea (2012), the lowest electrical resistivity is typically obtained at In/Zn ratios of 2 – 5%. Hence, it could be concluded that KF-IZO has good electrical properties.

ii) Elemental mapping analysis

Characteristic x-ray intensity is measured relative to a lateral position on the sample surface. Hence, the variations in x-ray intensity indicate the relative elemental concentrations across the surface. Maps are recorded using image brightness intensity as a direct function of the local concentration of the element or elements present. The lateral resolution of about 1µm is possible. EDS elemental mapping allows for all detectable elements to be analysed simultaneously, ensuring fast analysis in various settings. Hence, in this study, the elemental mapping analysis (qualitative and quantitative) of KF-IZO is explained.

The qualitative method is an interpretation of an image, whether an optical image, back-scattered electron image or a secondary electron image. The qualitative X-ray microanalysis was performed by energy-dispersive element spectra. Combining the processes of imaging with spectroscopy such as energy dispersive X-ray spectrometry (EDS) or wavelength dispersive spectroscopy (WDS) gives the capabilities for chemical analysis and chemical mapping on a microscopic scale. The subsequent production of elemental maps and chemical phase maps can make it quantitative. Therefore, qualitative and quantitative mapping analysis was conducted to identify the distribution of IZO on the KFs. Each pixel in the map is representative of the raw number of counts in the element's region of interest in the EDS spectrum. However, the background is not an issue in this case, as it provides far superior signal-to-noise. The elemental analysis of KF-IZO revealed the presence of C, O, In, Zn, and Cl in it. C and O were contributed by the KFs, while In, Zn, and Cl were contributed by IZO. Figure 4.5 confirms the presence of IZO on the KF substrates. The figure reveals the presence of Zn^{2+} (presented in pink colour) on the KF surface which leads to electrical properties.

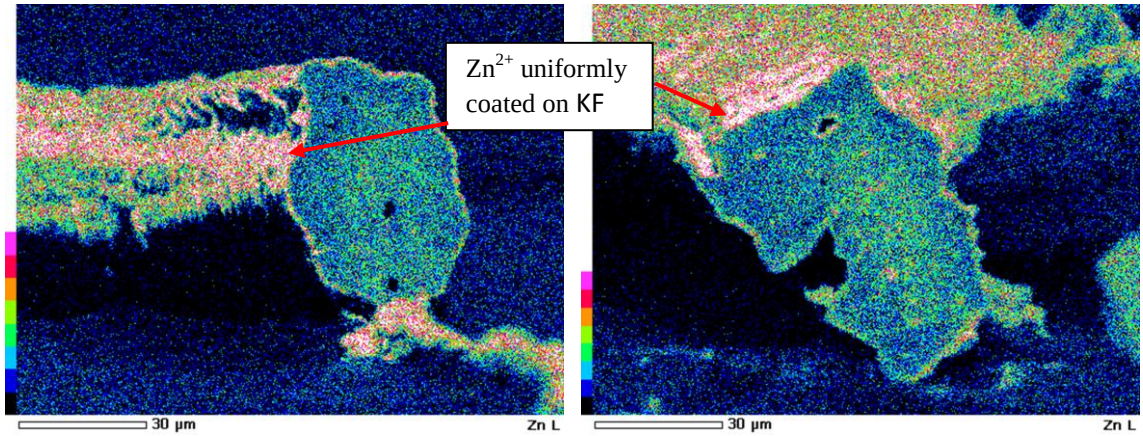

i) Cross sectional area of KF IZO

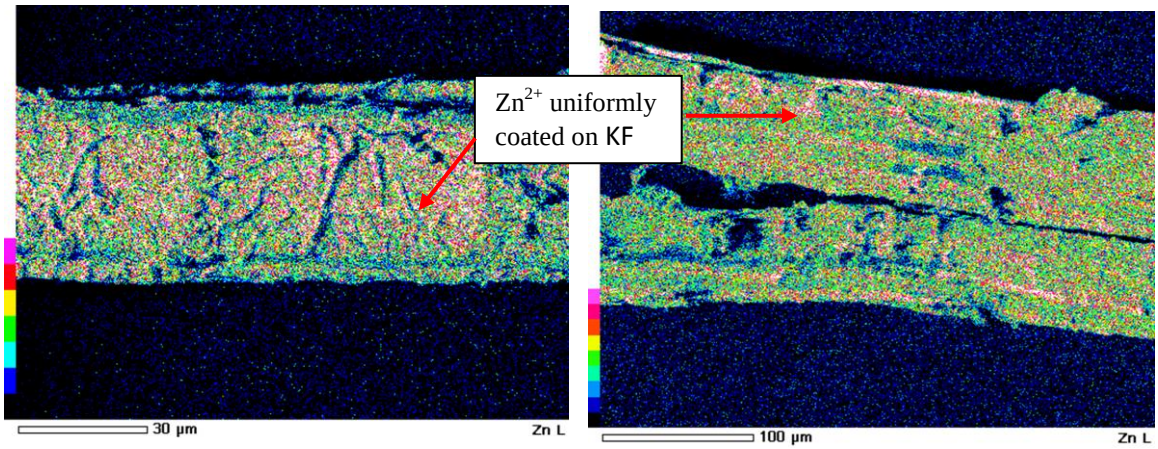

ii) Along the fibre side of KF IZO

Figure 4.5: SEM/EDX qualitative map analysis of the i) and ii), confirming the presence of Zn^{2+}.

Moreover, from the SEM/EDX quantitative map analysis, it can be clearly observed that the KFs were well-coated with IZO and that the Zn^{2+} was uniformly distributed around the fibre surfaces (Figure 4.6). The IZO layer had a thickness of about 5 µm and contained In^{3+} and Zn^{2+} ions. Furthermore, the Cl^{+} ions were also detected since indium (III) chloride was used as the dopant. The presence of thin ZnO layers on the KF substrates was confirmed. Liu et al. (2013) claimed that these layers are responsible for the good conducting properties of KFs. The conducting properties of ZnO thin films are primarily dominated by electron-generated vacancies and charge donations. For more details, this mapping can be referred to the appendix.

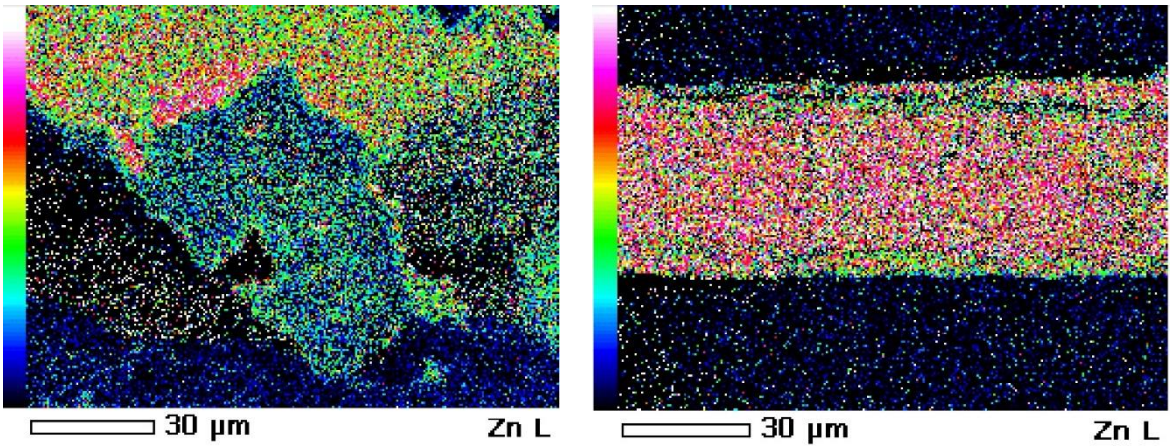

i) Cross sectional area of KF IZO ii) Along the fibre side of KF IZO

Figure 4.6: SEM/EDX quantitative map analysis of the i) and ii), confirming the presence of Zn^{2+}.

iii) Line profile analysis

The line profile analysis was also performed to identify the presence of Zn^{2+} on KF-IZO. For this analysis, the SEM's electron beam is scanned along a pre-determined line across the sample while x-rays are detected for specific positions along that line. Analysis of the x-ray energy spectrum at each position provides plots of the relative elemental concentration for each element compared to a position along the line. Next, the data is displayed on a qualitative graph, showing the increase or decrease in all elemental constituents present at all points on the line. This may also be condensed into more quantitative form by compressing the data captured along the line into equi-spaced spectra.

The line profile analysis for KF-IZO shown in Figure 4.7 shows the elements exist on the cross-section and along the side area of fibre in KF-IZO. Both pictures, as referred to Figure 4.7 i) and ii), show that Zn^{2+} only exists on the surface of KFs instead of the cross-sectional area. Other major elements such as O and C exist in KF's cross-sectional area. The small amounts of In and Cl elements, due to the dopant material mentioned earlier, were also detected. This clearly indicates the IZO thin film was only covered on

the outer surface of the KFs. Therefore, it provides good electrical conductivity to the KF-IZO whereas KF acts as a flexible support for IZO thin film.

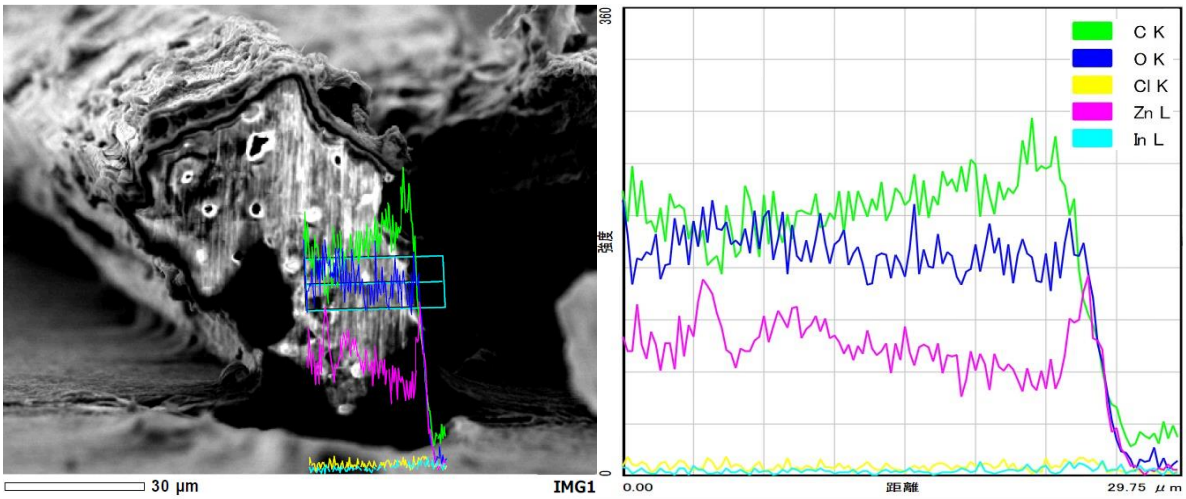

i) Cross sectional area of KF IZO

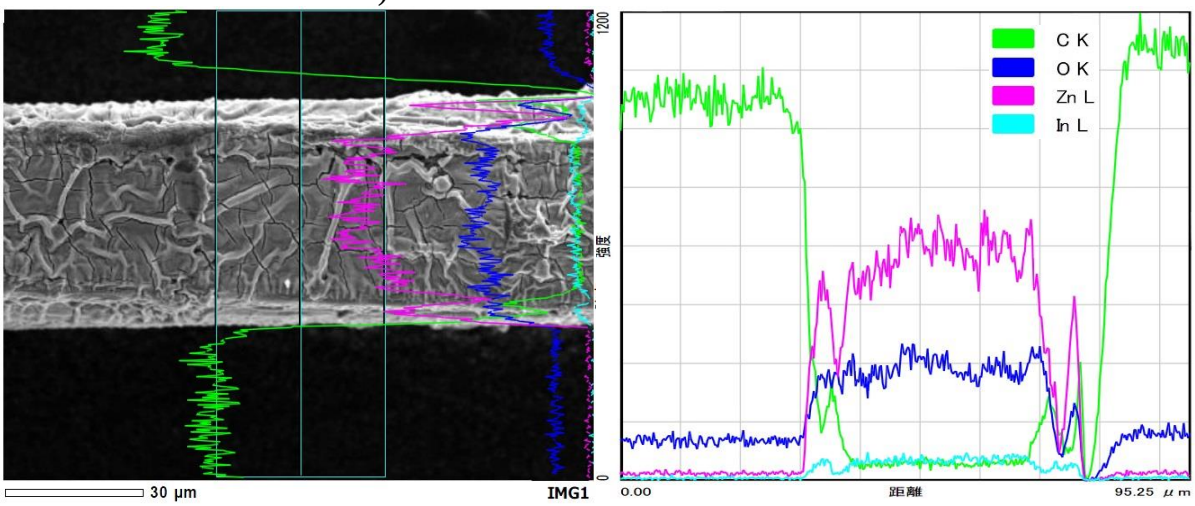

ii) Along the fibre side of KF IZO

Figure 4.7: SEM/EDX line profile analysis of the i) and ii), confirming the presence of Zn^{2+}.

4.4 KF-IZO electrical properties

In this study, the four-probe method employing a copper metal attachment plate was used to investigate the electrical properties of KF-IZO.

4.4.1 Effect of dipping rate

This investigation was performed at various dipping rates (1, 3, 5, 7, 9, 15, 20, and 30 mm/s) to obtain good adhesion of the IZO film deposited onto the KF substrates. El Yamny and Rafea (2012) stated that dipping rates in the range of 2–40 mm/s yield good quality films. Such films strongly adhered to the substrate and exhibit good transparency. Furthermore, the dipping rate affects the amount of precursor left on the substrate, which in turn, is a measure of the thickness and homogeneity of the thin film.

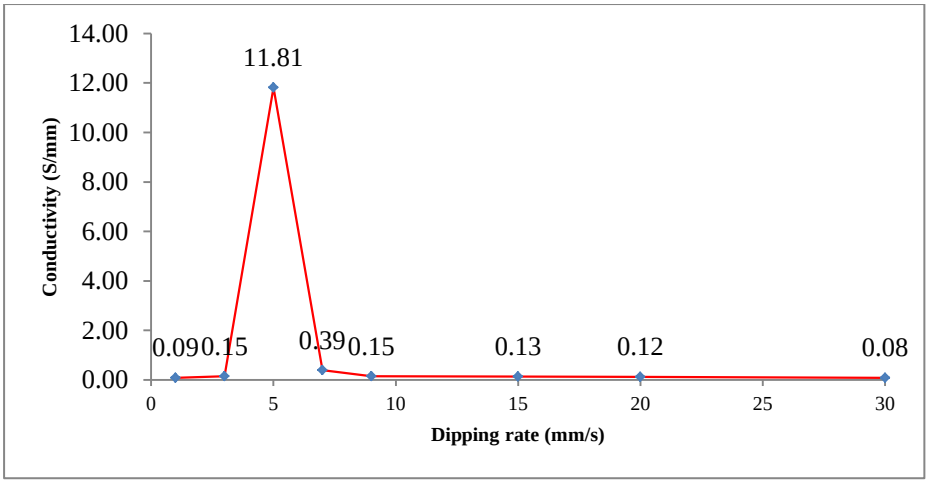

Figure 4.8: Electrical conductivity of KF-IZO vs. dipping rate at an annealing temperature of 150 °C.

From Figure 4.8, it can be seen that the dipping rate of 5 mm/s resulted in the highest electrical conductivity of 11.81 S/mm at an annealing temperature of 150 °C. The higher the dipping rate, the lower the electrical conductivity of KF-IZO. This phenomenon correlates with the observation that the amount of IZO deposited on the KF substrates increased with an increase in the dipping rate.

The surfaces of KF-IZO samples obtained at different dipping rates were observed using SEM and were compared (Figure 4.9). At lower dipping rates, the KFs absorbed more IZO because of their hydrophilic nature, which resulted in imperfections such as

uneven thin-film coating, breakage of the thin-film coating, agglomeration, and aggregation. Such imperfections affected the electrical conductivity of KF-IZO. Kuo et al. (2011), reported that when the film thickness is higher than a critical value, excess internal stress is produced, which causes structural discontinuities by the bifurcated orientation of crystal structure. As a result, the IZO films deposited on KF surfaces crack, as also observed in Fig. 4.9a. Both effects restrict the carrier mobility and reduce the conductivity. Similarly, the electrical conductivity of KF-IZO decreased dramatically at dipping rates above 5 mm/s. This is because less IZO (i.e. low In/Zn ratio) was deposited on the KF substrates as referred to Table 4.2. The results indicate that the dipping rate affected the In/Zn ratio and also the electrical conductivity performance of KF-IZO.

At the dipping rates of 1 and 30 mm/s, the In/Zn ratios of 5.09% and 4.07% were obtained, respectively. The dipping rate of 5 mm/s showed the highest In/Zn ratio of 6.4%. This observation is slightly inconsistent with the results reported by El Yamny and Rafea (2012). The authors reported the lowest electrical resistivity was obtained when a 1.5–5% In/Zn ratio was used. As reported by Rezaee Roknabadi et al. (2009), when indium (In) is added as a dopant to ZnO, it substitutes Zn because of their similar ionic radii. Since it has one extra electron than Zn, it acts as a donor impurity and creates an n-type semiconductor with high conductivity. Hence, the low In/Zn ratio resulted in the low conductivity of KF-IZO. In addition, the vaporisation of the precursor, which contained 50% ethanol, during the dipping process, may have affected the deposition of the dopant material on the surface of the KF substrates.

Table 4.2: The In/Zn ratios of the KF-IZO samples obtained at different dipping rate, as determined from the XRF results.

Elements	Dipping rate		
	1 mm/s	**5 mm/s**	**30 mm/s**
In	5.47	3.42	2.79
Zn	68.07	53.42	69.47
In/Zn ratio	5.09 %	6.40 %	4.07 %

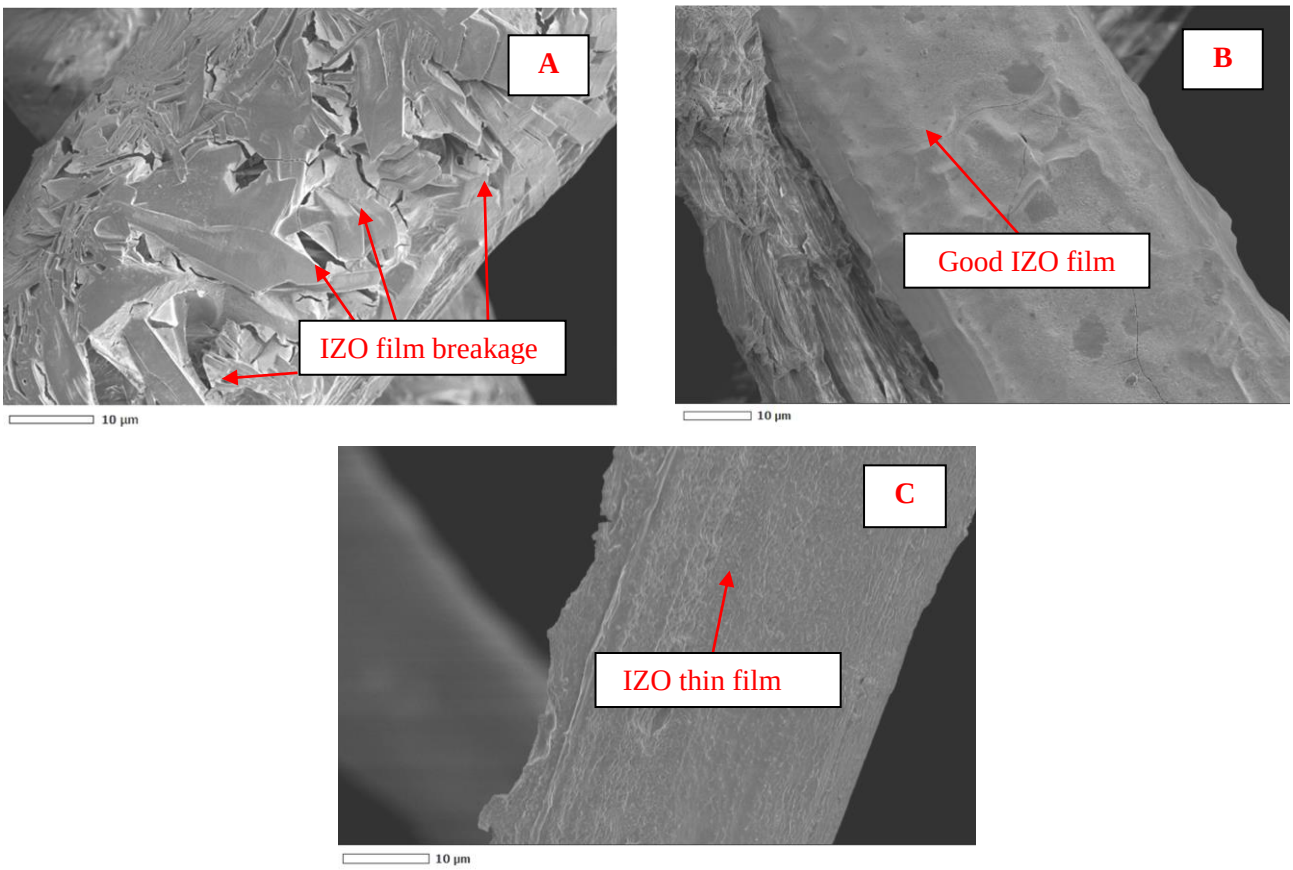

Figure 4.9: Comparison of the surfaces of KF-IZO samples obtained at various dipping rates; (a) 1, (b) 5, and (c) 30 mm/s.

4.4.2 Effect of the annealing process

The annealing process is an important aspect that requires investigation, particularly when adapted to natural fibres (NF). One of the disadvantages of NF fibres is low thermal stability (Tan et al., 2015). Therefore, the process conditions of TCOs need to

be adjusted to allow coating of such heat-sensitive substrates. Moreover, the temperature and time of the annealing process are the parameters that affect the NF accordingly. Many groups have reported the effects of annealing on the properties of ZnO thin films (Wang et al., 2003; Cho et al., 2001; Ozaki and Gomi, 2002; Ogata et al., 2000). However, the annealing conditions such as ambient gas species, annealing temperature, and time examined by the different groups and their findings are still under debate (Seng et al., 2016). Generally, low annealing temperature and time are strictly required for natural fibre because they are low-temperature application resources. The TGA results revealed that KF must be operated at low temperature (≤200 °C). Therefore, the effect of annealing temperature and time on the electrical properties of KF-IZO was further investigated.

i) Annealing temperature

Low annealing temperatures are strictly required for natural fibres due to their low-temperature applications. The thermogravimetric analysis (TGA) result shows that KF strongly decomposed at 219.25 °C with about 88.17% of remaining KF weight (Figure 4.1). In the previous study by Wielage et al. (1999), it was demonstrated that KF must be operated at low processing temperatures (≤200 °C). Table 4.3 shows parallel results, where KF weight loss increased with an increase in the annealing temperature.

Table 4.3: KF loss weight dependence annealed temperature.

Annealed Temp. (°C)	Loss weight of KF (%)
150	4.27
175	8.92
200	10.95

Furthermore, the KF decomposition result indicates that at temperatures ranging from 150 °C to 200 °C, KF lost about 4% - 11% in total weight (as represented in Table 4.3). This

creates an obstacle towards electrical current conduction of KF-IZO, as illustrated in Figure 4.10. As the temperature increased, the amount of oxygen desorption increased, and free carriers in the thin films also increased (Lee et al., 2012). It was observed that with the increase in the annealing temperature of IZO (In_2O_3: ZnO = 90:10 wt.%) from 100 °C – 300 °C, the carrier concentration decreased whereas the resistivity increased accordingly. However, with the rise in annealed temperatures, the amount of KF weight loss increased, resulting in a build-up of carbon concentration on the KF substrates, as reported in Table 4.3. The existing large amount of carbon created a barrier towards IZO coating to conduct electrical charges. Carbon is known as a non-metallic material and a good conductor with low electrical conductivity. Also, carbon residues are present in the samples as seen in the colour change in KF-IZO due to the annealing temperature (Figure 4.10). It shows that at an annealed temperature of 200 °C, KF-IZO turns blackish, and KF appears burnt and decomposed compared to the samples at 150 °C. Furthermore, the reaction between the IZO layers towards the KF surfaces during the annealing process caused another catastrophic change in KF structure making it more brittle.

150 °C 175 °C 200 °C

Figure 4.10: KF-IZO appearances after different annealed temperature (MORITEX – Scopemen series with 166× magnification).

ii) Annealing time

As observed in Table 4.4, the optimum annealing time for the conducting thin films was 4 h with a minimum resistivity of 0.0853 Ω.mm. However, the maximum

resistivity of 12.6154 Ω.mm was recorded at 16 h of annealing time. Similar findings were also reported by Seng et al. (2016), who state that the optimum annealing time for a conducting thin film (Aluminium doped tin oxide, (SnO_2: Al) is approximately 4 h, whereas the minimum values for the sheet resistance and resistivity are 6.78 × 10^6 (Ohm/sq) and 0.212 k (Ohm-cm), respectively. Based on Figure 4.11, the resistivity performance of KF-IZO increased with increase in annealing time. It was assumed that the annealing time directly affected the electrical properties of KF-IZO.

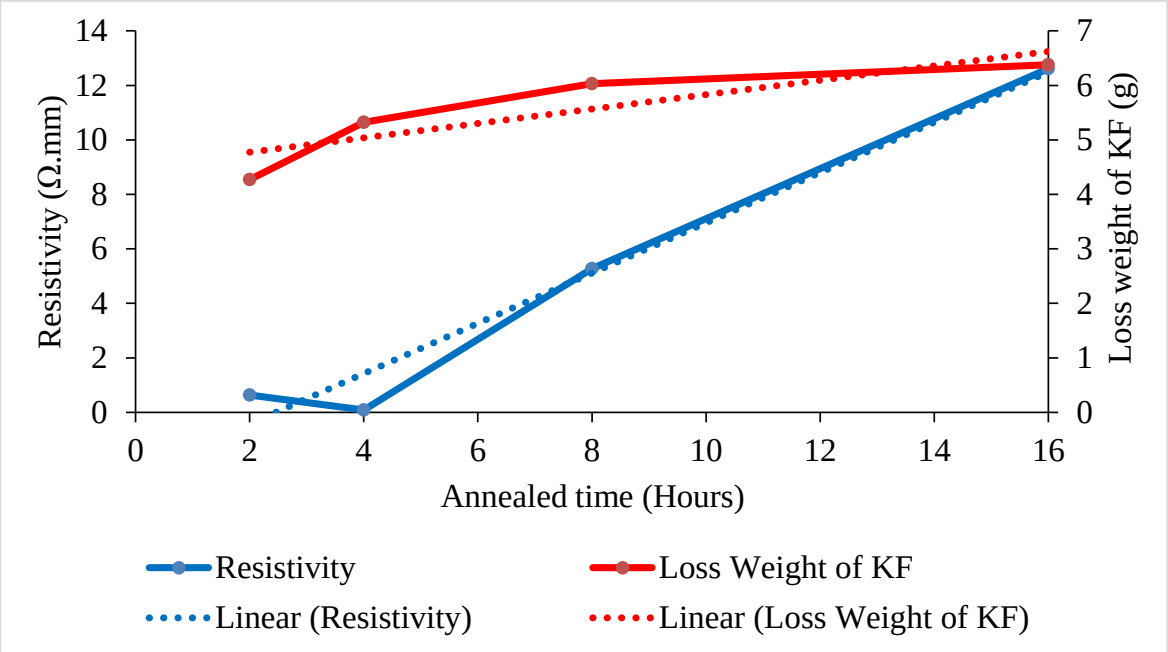

Figure 4.11: Dependence of resistivity and loss weight on the annealing time at 150 °C.

These results could be attributed to the decomposition of KF especially during the annealing process. According to Ishak et al. (2012), natural fibres undergo significant mass loss (~70 %) due to its basic constituents; cellulose, hemicellulose, and lignin which occurs at 140 °C and above. In this study, the TGA results for KF-IZO with different annealing time showed that KF experienced a weight loss of 4-6 % between 150 °C and 200 °C, as shown in Table 4.4.

Table 4.4: KF-IZO sample for different annealing time at a temperature of 150 °C.

Annealed Time (Hr)	**Resistivity (Ω.mm)**	**Loss weight of KF (%)**	**% Carbon (Diamond form)**
2	0.6370	4.27	3.8
4	0.0853	5.32	3.9
6	1.1676	5.91	7.8
8	5.2678	6.03	12.5
16	12.6154	6.38	17.0

Moreover, the amount (%) carbon also increased due to the build-up of carbon concentration on KF-IZO (Table 4.4). This was observed in the colour changes of the KF-IZO samples with increasing annealing time (Figure 4.12). It showed that within 16 h of annealing time and 150 °C, the KF-IZO turned black or burnt compared to other samples. This scenario occurred because KF was burning and forming carbon coal/diamond. Carbon in the form of diamond/coal is known as a non-conducting material. As a consequence, the amount of carbon formed introduced a barrier towards IZO coating. Furthermore, the percentage of carbon formed increased with the increase in annealing time. This drastically increased at 8 to 16 h annealing time. Lastly, the KF-IZO appeared more brittle with low strength compared to the raw KF.

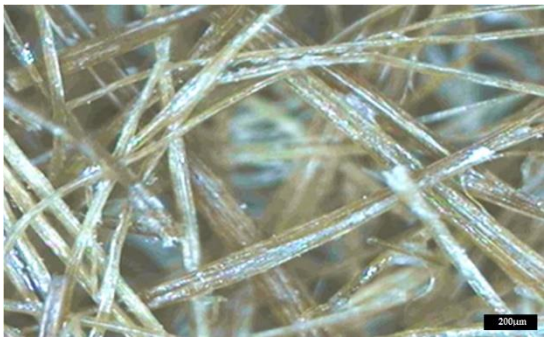

i) 2 h

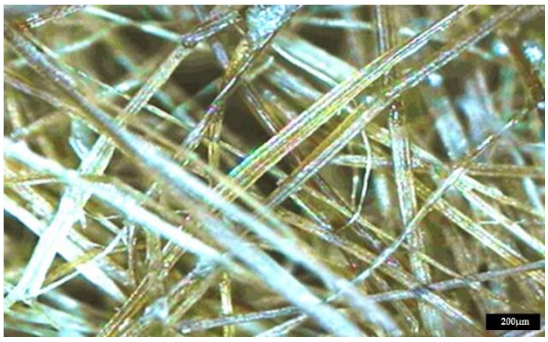

ii) 4 h

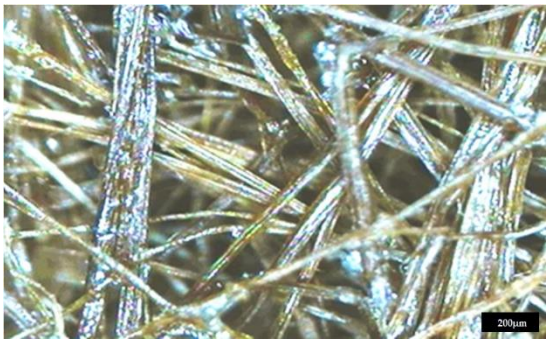

iii) 8 h

iv) 16 h

Figure 4.12: KF-IZO colour changes for four different annealing times; i) – iv) (MORITEX – Scopemen series with magnification 166×).

CHAPTER 5

RESULTS AND DISCUSSION – STUDY OF NANOSTRUCTURED TUBULAR TiO_2 SYNTHESIZED USING KENAF FIBRES AS A SACRIFICIAL TEMPLATE

5.1 Introduction

This chapter will analyse and discuss the photocatalytic activity of nanostructured tubular TiO_2 synthesised using kenaf fibres as a sacrificial template. The study parameter is the calcination temperature of tubular TiO_2.

5.2 Thermogravimetric analysis (TGA)

The TGA analysis was performed on the raw and TiO_2-coated KFs to examine the thermal decomposition and degradation of the materials. Four stages of the thermal degradation of natural fibres were observed (Fig. 5.1) corresponding to moisture evaporation, hemicellulose decomposition, cellulose decomposition, and lignin decomposition (Yang et al., 2007; Ishak et al., 2012).

According to the TGA results obtained, the KFs coated with TiO_2 require higher temperatures before a drastic weight loss is observed (compared to the raw KFs). The relatively slow decomposition of the TiO_2-coated KFs can be explained by the fact the TiO_2 coating acts as a protective layer in the temperature region of 350–400 °C. This observation indicates the thermal degradation resistance of KF mats can be significantly improved by applying TiO_2 coatings. At 500 °C, all the KF species were completely removed from the TiO_2 layer. It is interesting to note that the complete decomposition and

degradation of the TiO_2-coated KFs (corresponding to the decomposition of its cellulose and lignin components) occurs at a slightly higher temperature (~500–550 °C) compared to the uncoated KFs. The remaining weight of 10–15 wt. % represents the synthesised tubular TiO_2 material.

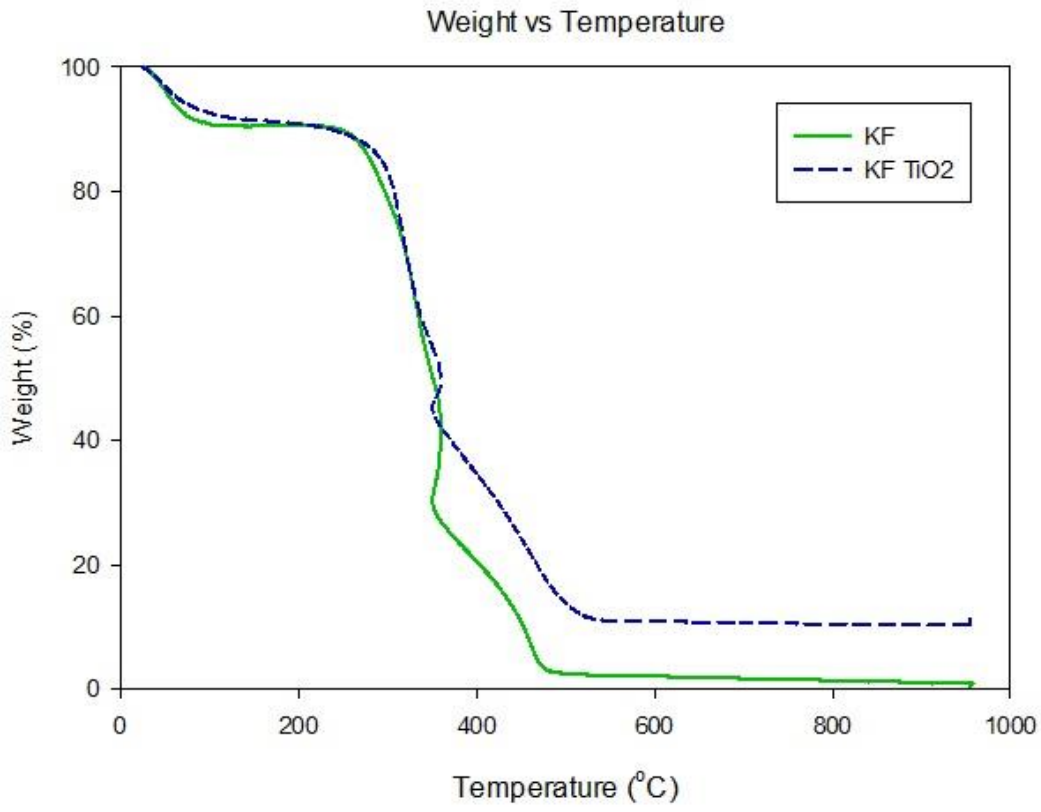

Figure 5.1: TGA spectra recorded for TiO_2-coated KF and KF fibres.

5.3 Microscopy observation

The microscopy analysis is divided into two (2) sections; i) Optical microscopy through SEM images and ii) SEM/EDX analysis (includes point/area analysis and elemental mapping analysis).

5.3.1 Optical microscopy and SEM

The optical microscopy and SEM images of tubular TiO_2 synthesised through the

kenaf template-assisted sol-gel method are shown in Figure 5.2. Here, the KFs acted as a sacrificial template and were burnt off at a high calcination temperature to produce the yellowish white TiO_2 tubes, which replicated the fibre shape. In other words, the obtained material reproduced the hollow structure of KFs containing nano-sized thin walls.

Figure 5.3 shows the SEM images of the TiO_2 species formed at calcination temperatures of 500, 700, and 1000 °C. The produced tubular TiO_2 assumed the shape of the KF template with a wall thickness of 0.15–0.20 µm. According to the SEM images depicted in Figure 5.3(a) and (b), the tubular TiO_2 formed at 500 °C is characterised by a smooth surface. However, after the calcination temperature was increased to 700 °C, a new granular structure was formed. Furthermore, the fraction of this new phase increased as the temperature of calcination further increased to 1000 °C (Figure 5.3(c)), which corresponded to the transformation of the anatase phase to the rutile phase. Figure 5.4 presents the significant difference in the wall structure of anatase compared to the rutile phase based on the calcination temperatures of 500 °C and 1000 °C, respectively. Based on the images, it is confirmed that tubular TiO_2 changed completely to the rutile phase at 1000 °C meaning that granular structure is formed on the tubular TiO_2 surfaces. It has been reported that the nucleation and growth of the rutile phase are initiated in the temperature range of 600–700 °C (Li et al., 2003; Li et al., 2004). In another study, the initial and final temperatures for the formation of the rutile phase were 600 and 900 °C, respectively (Oskam et al., 2003). These results confirm that the calcination temperature highly influences the surface structure of TiO_2.

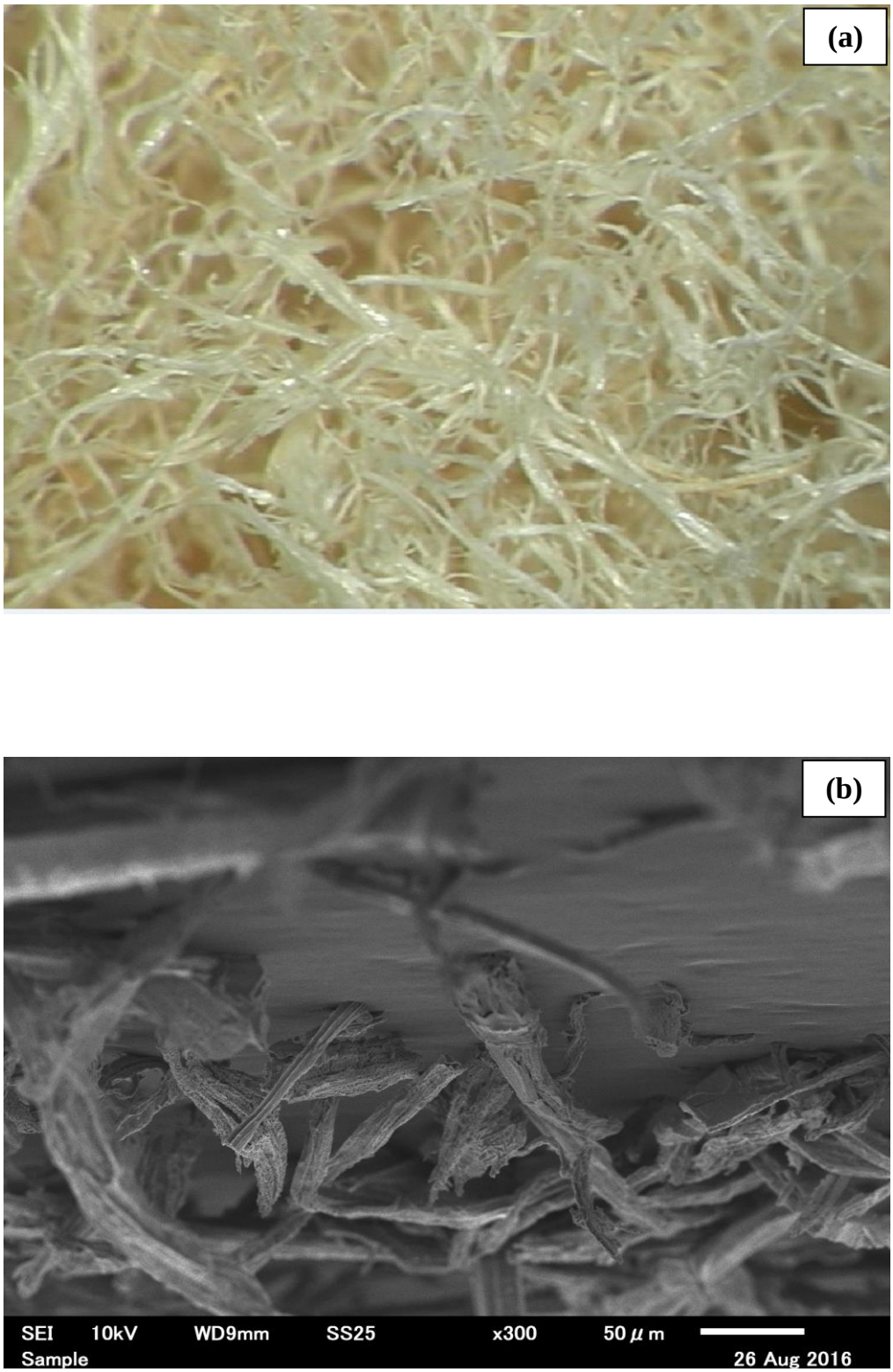

Figure 5.2: Image of tubular TiO_2; a) Optical microscopy images of tubular TiO_2, b) SEM image of tubular TiO_2.

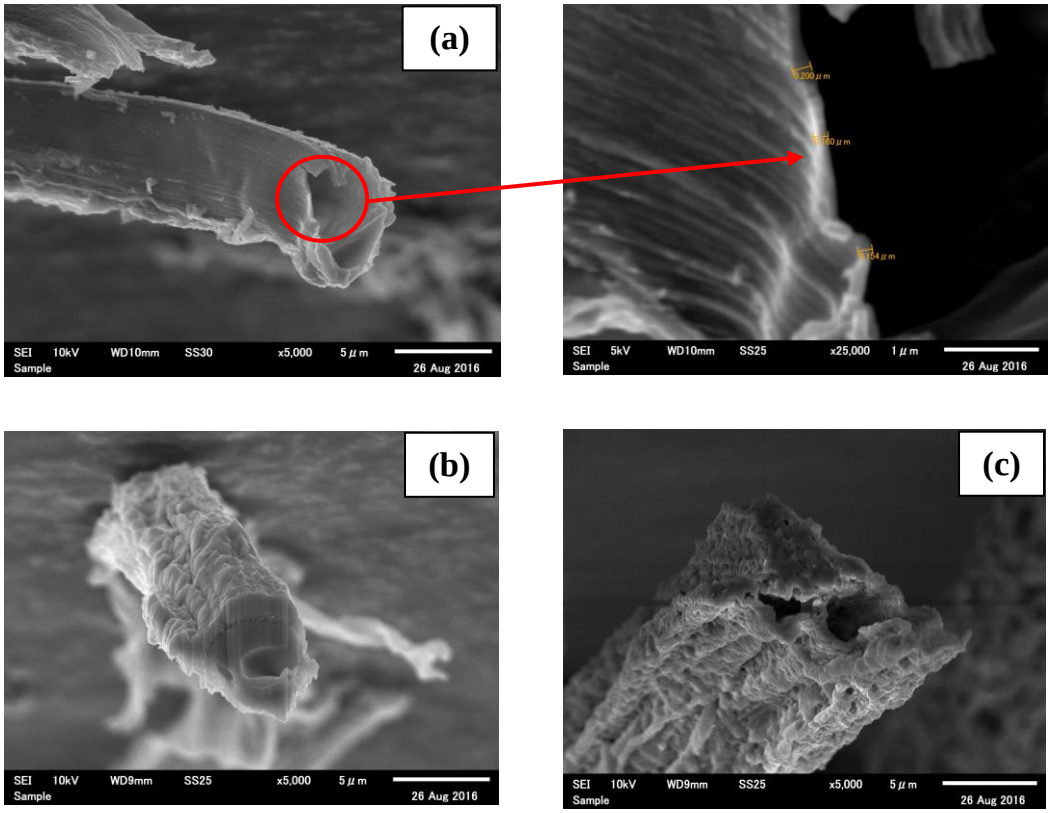

Figure 5.3: SEM images of tubular TiO_2 formed at calcination temperatures of (a) 500 °C (25,000× magnification to clarify nanostructures wall thicknesses), (b) 700 °C, and (c) 1000 °C (obtained at a magnification of 5000×).

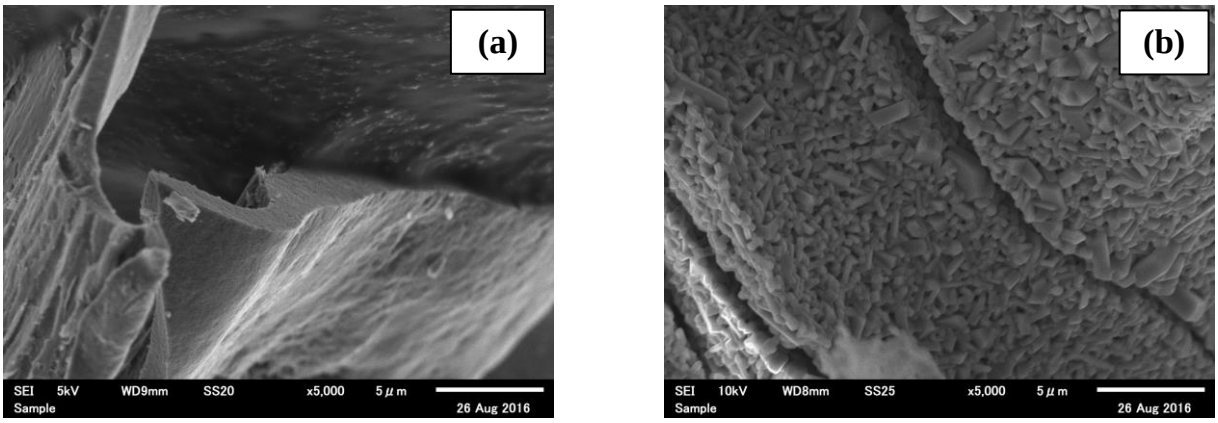

Figure 5.4: SEM images of tubular TiO_2 formed at calcination temperatures of (a) 500 °C (b) 1000 °C where there are significant differences on the pattern of the wall structures.

5.3.2 SEM/EDX analysis

The tubular TiO_2 was further examined by SEM/EDX to perform point/area based surface analysis.

i) Point/Area analysis

The point/area analysis was selected to analyse the tubular TiO_2 and detect the presence of elements in the material. The atomic fractions of C, O, and Ti elements of the TiO_2 layer formed at 500 °C, 700 °C and 1000 °C, obtained through SEM–EDX, are listed in Table 5.1. The location of the point/area analysis is shown in Figure 5.5 (a) to (f). It was found that the atomic fraction of Ti increased with an increase in the calcination temperature due to the larger crystallite size of tubular TiO_2. At the calcination temperature of 500 °C, the atomic fractions of C on the inner and outer surfaces of tubular TiO_2 were ~15 %. However, at 700 °C, the atomic fractions of C obtained for the inner and outer surfaces were 36.18 % and 16.36 %, respectively. This could be explained by the stronger decomposition of KFs at higher calcination temperatures that generated more C-containing volatile compounds. In addition, the results for C obtained at 1000 °C, also presents the same pattern of C-containing volatile compounds at 700 °C, 8.21% (inner) and 3.91 % (outer). As a result, a larger number of C atoms were detected on the inner surface of TiO_2 tubes due to the direct attachment to the fibres of the KF template. As seen in Table 5.1, the C content dramatically decreased at the calcination temperature of 1000 °C. It is because the majority of the C-containing compounds have been converted to O-containing volatile compounds.

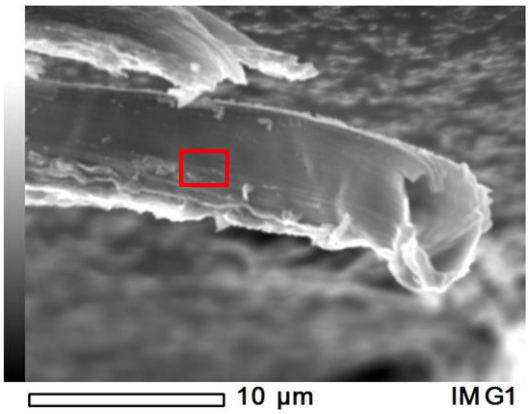

(a) 500 °C (outer)

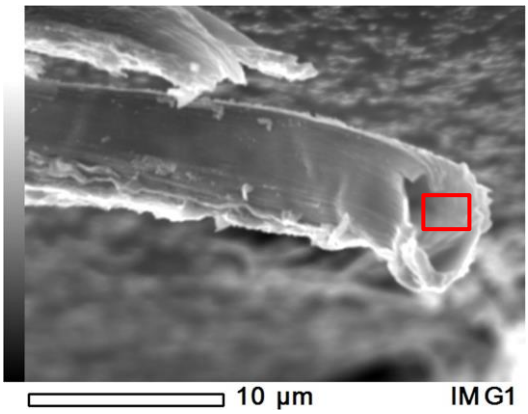

(b) 500 °C (inner)

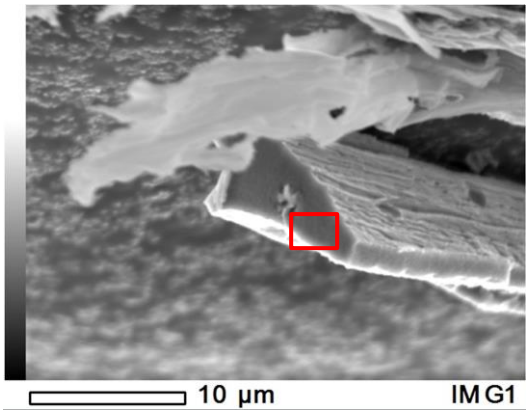

(c) 700 °C (outer)

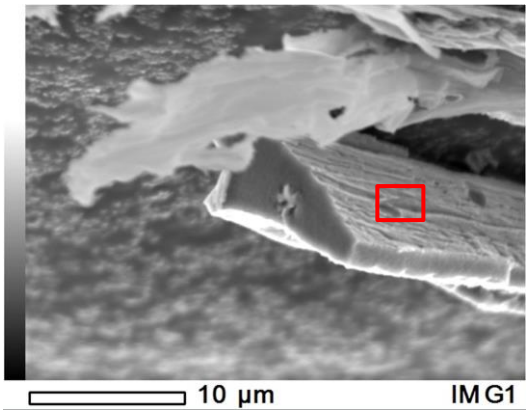

(d) 700 °C (inner)

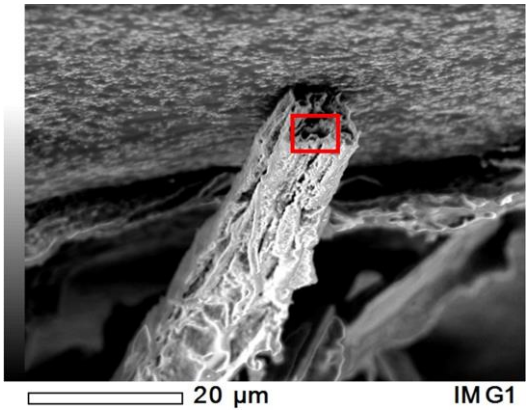

(e) 1000 °C (outer)

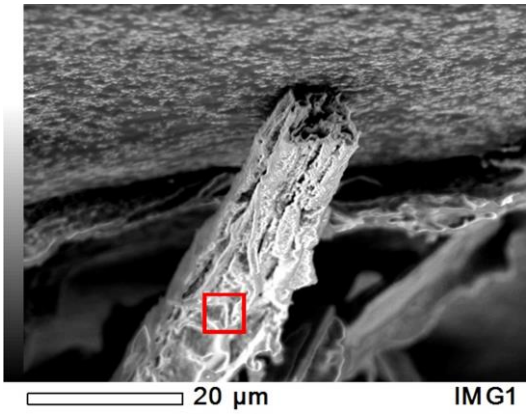

(f) 1000 °C (inner)

Figure 5.5: Point/Area analysis of tubular TiO_2 (outer and inner) by SEM/EDX.

Table 5.1: Atomic fractions of various elements in tubular TiO_2 measured by SEM/EDX.

Calcination temperature (°C)	Analyzed surface	Atomic fractions of elements (%)			
		C	O	Ti	Total
500	Inner	15.98	61.41	22.61	100
	Outer	15.15	56.88	27.97	100
700	Inner	36.18	22.81	41.01	100
	Outer	16.36	47.42	36.21	100
1000	Inner	8.21	56.34	35.45	100
	Outer	3.91	66.52	29.57	100

ii) Elemental mapping analysis

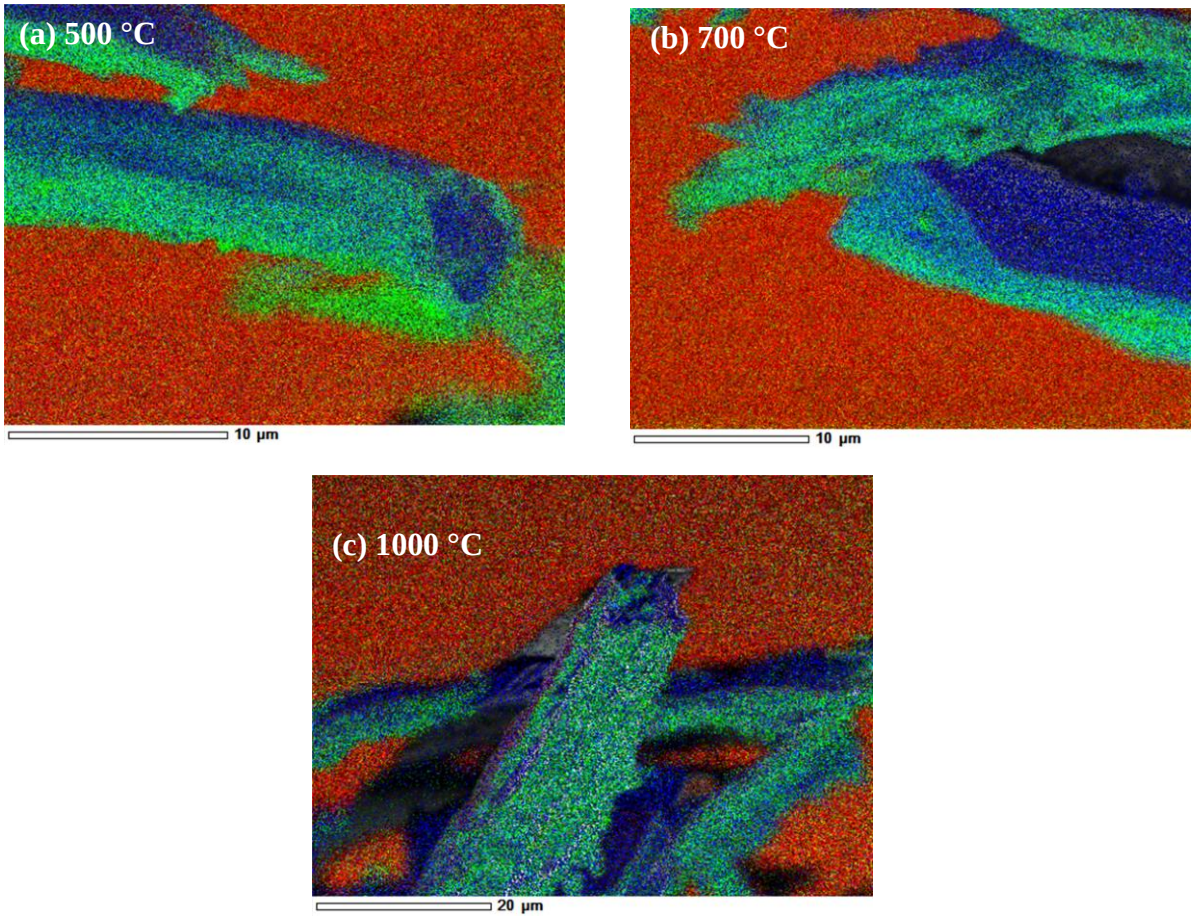

Figure 5.6: Elemental mapping analysis of tubular TiO_2 by SEM/EDX at a calcination temperatures of 500 °C, 700 °C and 1000 °C.

Elemental mapping analysis was used to confirm the elements present on the tubular TiO_2. The elements; O, C and Ti, detected on the tubular TiO_2 where based on images captured, O = green, C = red and Ti = blue. Figure 5.6 (a) to (c) illustrated the analysis according to the calcination temperatures; 500 °C, 700 °C, and 1000 °C for all the existing elements. Figure 5.7 presents the elemental mapping for tubular TiO_2 at 500 °C for every single element that exists on the material. From the images, it is seen that Ti dominated the surfaces. Meanwhile, the presence of O and C, which exist as volatile compounds, were varied based on the temperatures applied.

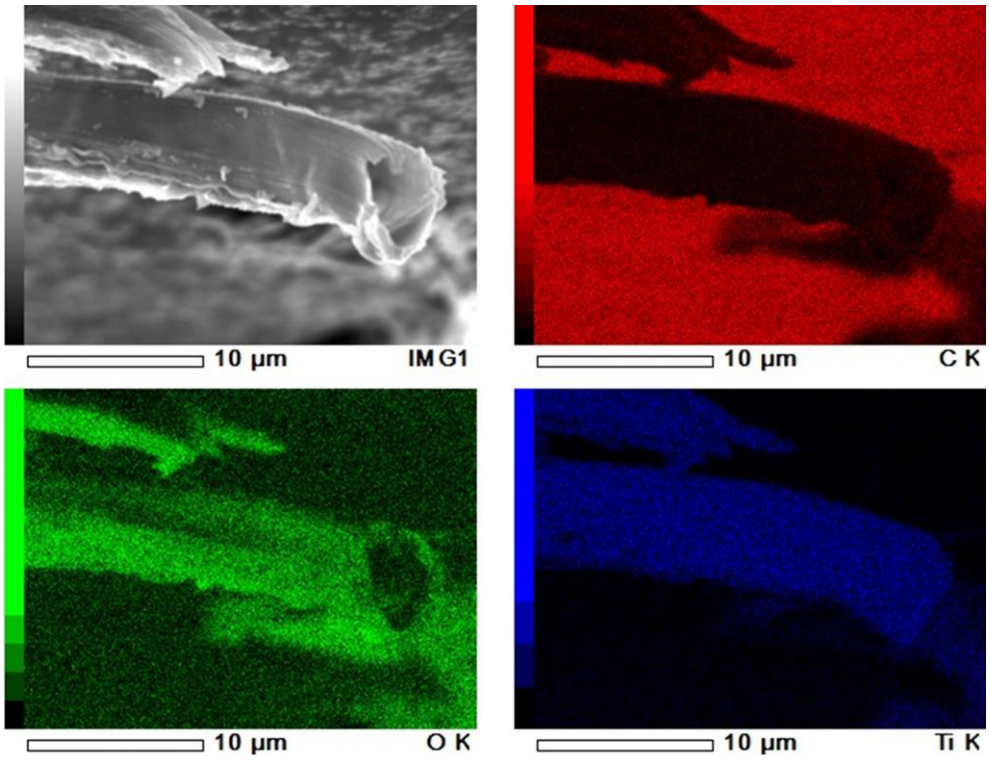

Figure 5.7: Elemental mapping of tubular TiO_2 at 500 °C for all elements (C, O and Ti).

5.3.3 XRD studies

The XRD technique was utilised to examine the crystallinity and crystallite sizes of the synthesized TiO_2 samples. Figure 5.8 shows the XRD patterns recorded for the TiO_2

nanostructures synthesised from the KF templates and calcined at different temperatures. The sharp, intense peak observed at a Bragg angle of 25.3° for all samples represents the anatase phase. The obtained patterns clearly demonstrate that all samples exhibited high degrees of crystallinity, while the wide peaks indicate the presence of defects in the sample nanostructures. The variations of the TiO_2 crystallite size with the calcination temperature is demonstrated in Figure 5.9. Here, the TiO_2 crystallite size was estimated from the XRD line broadening using Debye-Scherrer's equation (Oskam et al., 2003):

$$B = \frac{k\lambda}{s\cos\theta} \qquad \text{(Eq. 2)}$$

Where B is the full width at half maximum (FWHM), k is the constant equal to 0.94, λ is the wavelength of X-ray radiation (Cu Kα = 0.15406 nm), s is the crystallite size, and θ is the diffraction angle.

The results showed that the average crystallite size increased with an increase in the calcination temperature. Therefore, the tubular TiO_2 with the smallest crystallite sizes was produced at 500 °C. Similarly, the size of the crystallites formed increased when the temperature was first increased to 600 °C, and then 700 °C. This observation could be attributed to the thermally promoted crystallite growth (thus, the size of anatase crystallites increased from 9.27 nm to 22.94 nm after the calcination temperature was increased to 700 °C).

At 700 °C, the formation of the rutile phase was detected in addition to the anatase phase, as indicated by the small (110) rutile peaks observed in the XRD spectra at a Bragg angle of 27.5° (see Figure 5.8). At this temperature, the crystallite size was larger than the value obtained at lower temperatures (Figure 5.9). Therefore, the growth of the rutile

phase affects the average crystallite size, as indicated by the drastic increase in its nucleation temperature equal to around 600–700 °C (Mahshid et al., 2007). At 1000 °C, the anatase phases were completely changed to rutile, as earlier mentioned. The decrease in the anatase peak was changed by the higher rutile peak (110) that occurred on the graph as observed in Figure 5.10.

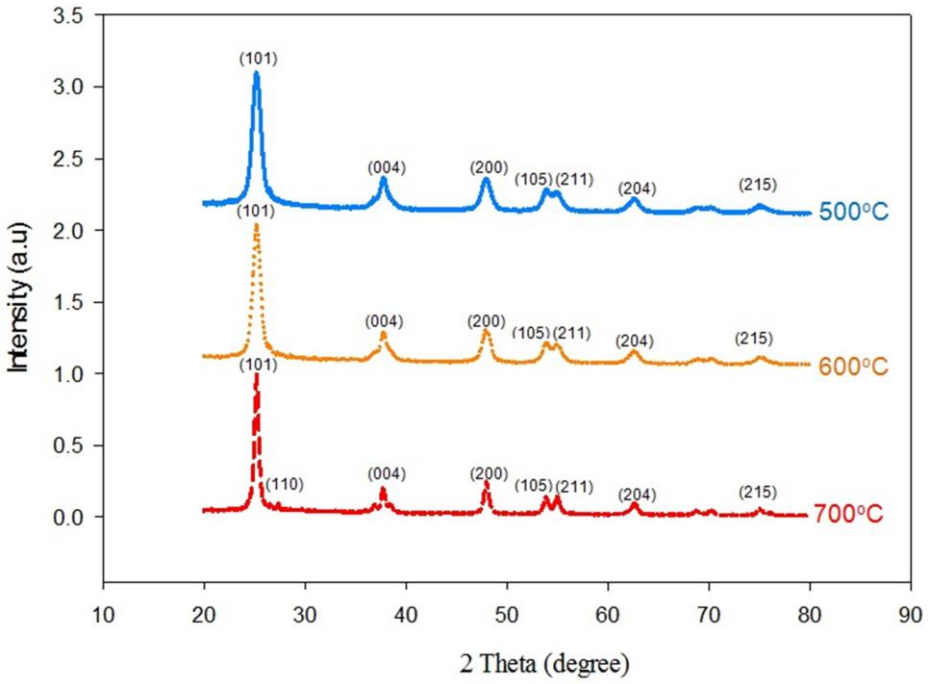

Figure 5.8: XRD spectra of tubular TiO_2 synthesised at different calcination temperatures.

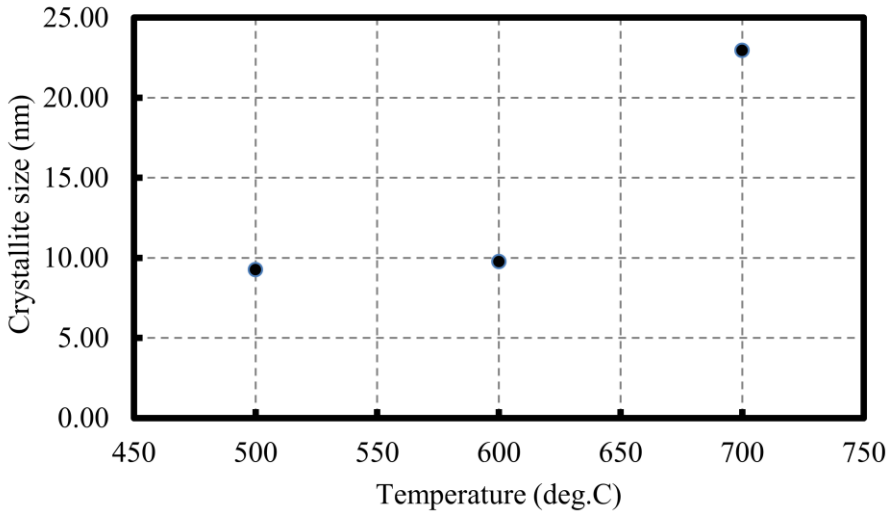

Figure 5.9: Crystallite sizes of tubular TiO_2 formed at different calcination temperatures.

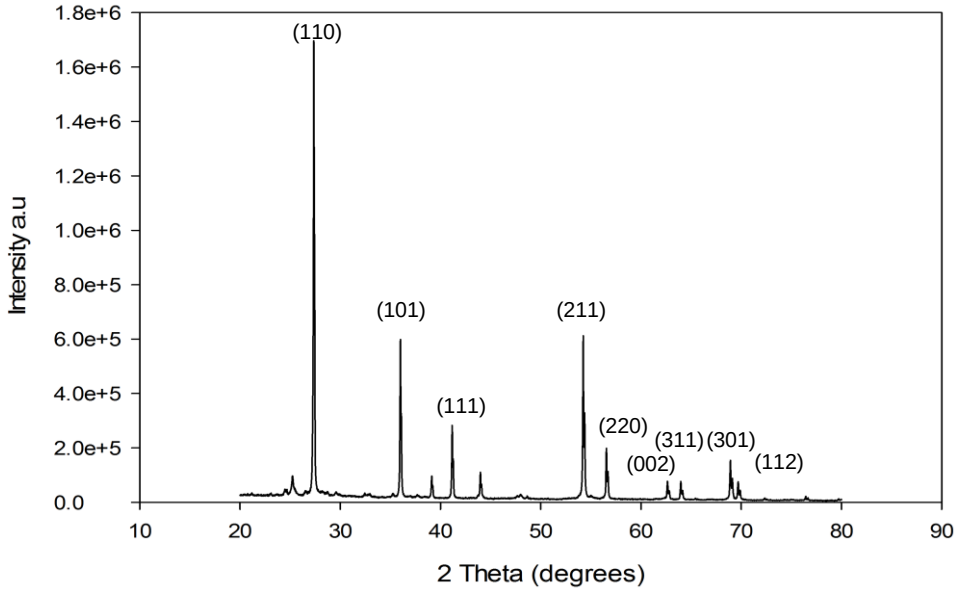

Figure 5.10: XRD spectra of tubular TiO_2 synthesised at 1000 °C calcination temperatures.

5.3.4 BET analysis

In this study, BET analysis was performed to evaluate both the BET area and average pore size of the tubular TiO_2 (see Figure 5.11). During the analysis, the Dollimore-Heal (DH) method was utilised by plotting the two highest peaks for the samples synthesised at 500 °C, 600 °C, and 700 °C (these graphs represent the pores size distributions on the tubular TiO_2 surfaces; see Figure 5.12). The results indicate that the tubular TiO_2 is a mesoporous material because it exhibits pore diameters of 6–8 nm (peak 1) and 30–40 nm (peak 2). Generally, mesoporous materials contain pores with diameters ranging between 2 and 50 nm (Sing, 1985). Furthermore, Table 5.2 lists the parameters of the TiO_2 tubes synthesised from the KF template, which shows that the BET areas increase with increasing temperature of calcination. The results also indicate that the TiO_2 tubes produced at 500 °C exhibit the highest porosity. In other words, the TiO_2 sample formed at 500 °C is characterised by higher porosity compared to the sample synthesised at 700 °C, and therefore, higher photocatalytic activity due to the easier access of the organic

pollutants to the catalytically active sites (Wang and Caruso, 2011). Moreover, it was found that higher volumes of mesopores were obtained for tubular TiO_2 calcined at 600 °C and 700 °C.

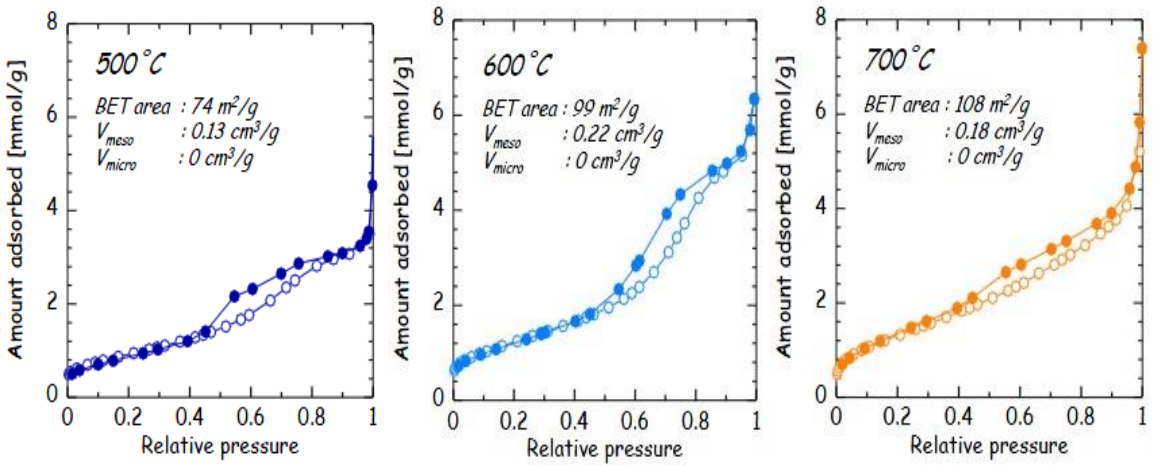

Figure 5.11: N_2 adsorption isotherms of tubular TiO_2 synthesised at 500 °C, 600 °C, and 700°C.

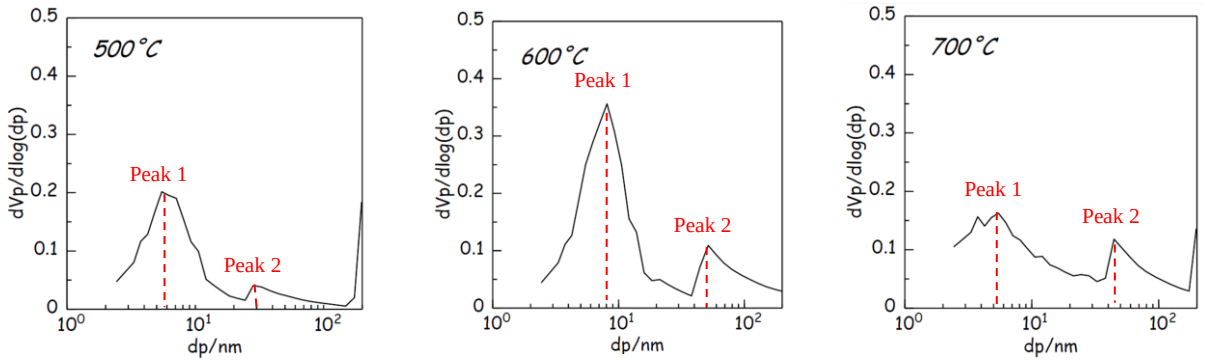

Figure 5.12: Pore size distributions (DH plots) of tubular TiO_2 synthesised at different calcination temperatures.

Table 5.2: BET surface areas of the synthesised tubular TiO_2 samples.

Sample	**BET area (m^2/g)**	**Volume of mesopores (cm^3/g)**	**Pore size distribution [peak 1 (6–8 nm) to peak 2 (30–40 nm) ratio]**
TiO_2 500	74	0.13	4
TiO_2 600	99	0.22	3.5
TiO_2 700	108	0.18	1.5

5.3.5 Performance test - UV analysis for the photocatalytic activity of TiO_2

In general, the photocatalytic activity of TiO_2 depends on several parameters including crystallinity, phase composition, and surface area (Neppolian et al., 2007). The photocatalytic activity of tubular TiO_2 can be evaluated by studying the degradation of MB under the UV irradiation with a wavelength of 365 nm. Figure 5.13 shows the colour of the irradiated MB solution, which becomes almost clear after 24 h, due to its degradation in the presence of TiO_2.

Figure 5.14 compares the fractions of MB remaining in solution after specified time intervals in the presence of tubular TiO_2 calcined at various temperatures. It shows that tubular TiO_2 synthesised at 500 °C exhibits the highest photocatalytic activity, compared to the samples at 600 °C and 700 °C. Hence, the results are in good agreement with the smallest crystallite size measured for tubular TiO_2 synthesised at 500 °C, which suggests the crystallite size of the tubular TiO_2 is closely related to its photocatalytic activity. As was previously reported by Sun et al. (2010), the decrease in the TiO_2 surface area due to the increase in its crystallite size reduces the degradation rate of MB. Therefore, the smaller crystallite sizes increase the photocatalytic activity of tubular TiO_2.

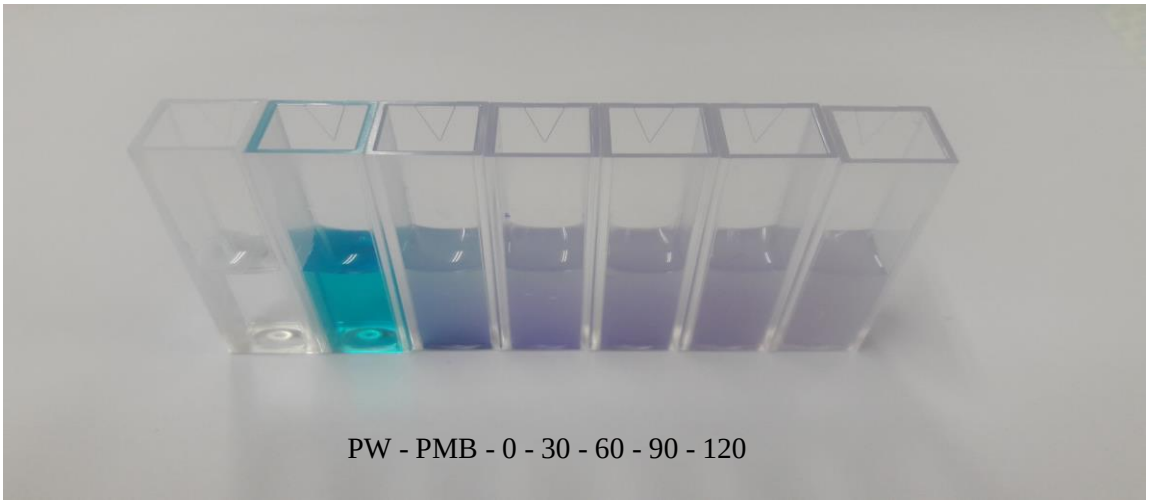

Figure 5.13: Colour changes of the MB solution containing tubular TiO_2 synthesised at 500 °C exposed to UV irradiation for 0–120 min (PW: pristine water, PMB: pristine methylene blue).

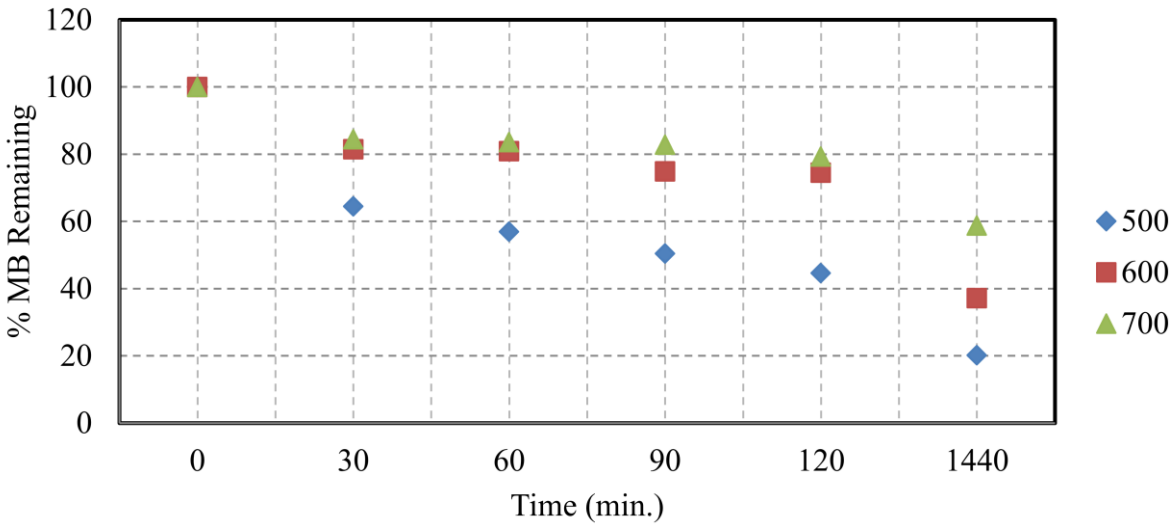

Figure 5.14: Percentages of the MB remaining containing tubular TiO_2 synthesised at different calcination temperatures.

The anatase phase of tubular TiO_2 exhibits the most intense processes of desorption, absorption, and photocatalytic activity (self-cleaning). During the initial stage, the MB dye molecules become trapped on the surface of tubular TiO_2. Next, the self-cleaning of MB through photocatalytic oxidation occurs during UV irradiation. As a result, the photocatalytic activity of the tubular TiO_2 formed at 600 °C slowly decreases. Simultaneously, the TiO_2 crystalline structure becomes more compact and solid with increasing temperature, which reduces the rates of desorption and absorption of MB species and thus the photocatalytic activity of tubular TiO_2.

For the tubular TiO_2 formed at 700 °C, there is a transformation of the anatase to the rutile phase (as demonstrated by the observed changes in its surface structure). The TiO_2 species assume granular shapes, and their crystallite sizes increase with an increase in the calcination temperature. These observations are in good agreement with a previous study, which showed that the presence of the anatase phase increased the rate of a photocatalytic reaction to a greater extent than the rutile phase because of its band gap and surface properties (Luttrell et al., 2014). Furthermore, the results of other studies also

revealed that the anatase phase of TiO_2 is more photocatalytically active toward the degradation of organic materials than the rutile phase (Barakat et al., 2005; Ba-Abbad et al., 2012).

After 24 h of UV irradiation (1440 min), the fractions of MB species removed were 80, 63, and 51 %, for samples calcined at 500, 600, and 700 °C, respectively. Therefore, the photocatalytic activity of tubular TiO_2 decreases with an increase in the calcination temperature (Figure 5.15). The degree of the photocatalytic degradation of MB can be expressed as follows:

$$\text{Photocatalytic degradation (\%)} = (\text{Co} - \text{C})/\text{Co}\ x\ 100\ \% \qquad \text{(Eq. 2)}$$

Here C_o is the initial concentration of MB, and C is the concentration of MB after irradiation. As illustrated in Figure 5.15, the fraction of the oxidised MB decreases with increasing temperature due to the crystallite growth and phase transformation from anatase to rutile.

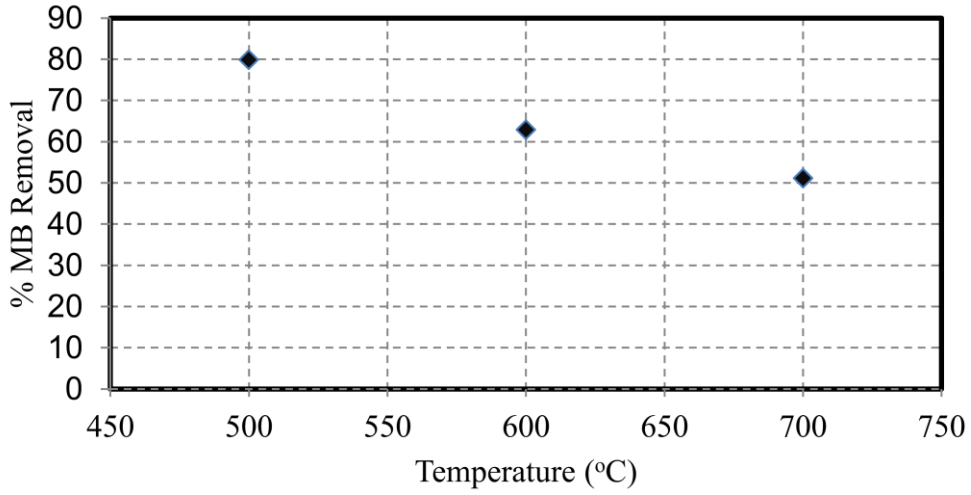

Figure 5.15: Calcination temperature dependence of the photocatalytic removal of MB observed after 24 h of UV irradiation.

CHAPTER 6

CONCLUSION AND RECOMMENDATIONS

In a nutshell, the following conclusions are obtained which is reflecting to the defined objectives.

6.1 Study of morphology and electrical properties of KF-IZO

The KF has successfully coated with IZO using the dip-coating method. The ZnO which acts as precursor and indium as dopant material for TCO-IZO is the best combination so far. This is because it can be processed at low temperature and adapted to KF. The potential of KF as a conductor was successfully explored with emphasis on its morphology and electrical conductivity. The results revealed that KF-IZO showed the highest electrical conductivity of 11.81 S/mm at a dipping rate of 5 mm/s at 150 °C. The SEM/EDX results revealed that Zn^{2+} and In^{3+} co-existed on the surface of the KF substrates and were uniformly distributed around the fibres. Furthermore, no significant damage to the KF-IZO samples occurred when the dipping rate was 5 mm/s, as evident from the SEM images. Besides, the lowest resistivity was observed in KF-IZO at 150 °C for 4 hours annealing time, 0.12 Ω.mm while the highest is 12.62 Ω.mm for 16 hours of annealing time. The SEM/EDX elemental analysis shows the In/Zn ratio is about 5.5% to 6.5% which is similar to the prepared solution. The FIB revealed good coating condition of KF-IZO as well as an IZO thin layer thickness growth of 5 μm. The annealing time was found to influence the electrical resistivity of KF-IZO because of the carbon formation

element contributed by KF. In a nutshell, these outcomes could provide information and ideas for the newly developed KF-IZO. In conclusion, it can be said that dipping rate of the dip-coating process, temperature and time of annealing process has significantly influenced the electrical properties of KF-IZO.

6.2 Study of nanostructured tubular TiO_2 synthesised using kenaf fibres as a sacrificial template.

A pure tubular TiO_2 with the high surface area was successfully synthesised by a facile method using KFs as a sacrificial template. The utilised technique does not require any surfactants and, therefore, is relatively simple, inexpensive, and saves time. It was found that the produced TiO_2 replicated the structure of the KF template with a tubular shape and nano-sized thin walls with a thickness of about 150–200 nm. The synthesised tubular TiO_2 was predominantly composed of the anatase phase (corresponding to the XRD peak centred at a Bragg angle of 25.3°) even at calcination temperatures above 600 °C. At the calcination temperature of 700 °C, the produced TiO_2 transformed the anatase to the rutile phase corresponding to the Bragg angle of 27.5°. The hollow tubular structure of TiO_2 exhibited high BET surface area, while the calcination temperature significantly affected the porosity distribution and photocatalytic activity of TiO_2. The obtained results indicate that the TiO_2 tubes produced at 500 °C were characterised by the highest degree of porosity resulting in the degradation of 80 % MB species in solution after 24 h of UV irradiation. In summary, KFs can serve as an effective, abundant, and inexpensive template material for the synthesis of nanostructured tubular TiO_2 with the high surface area. The empirical evidence presented in this thesis proves that kenaf fibres work as flexible support for IZO thin films as well as a sacrificial template of nanostructured tubular TiO_2 by applying a dip-coating technique on the fibres.

6.3 Recommendations for future improvement

Here is a list of recommendations for future studies.

6.3.1 KF-IZO

1. Study of other kinds or form of natural fibre. The highly recommended form of fibre should be unidirectional and with filaments of homogeneous sizes. It is easier to determine the electrical properties as well as morphology observation.
2. Investigation of the different kinds of dopant material such as B, Al and Ga to increase the electrical conductivity of the ZnO thin films. The use of In as the dopant material in the current development should be reduced due to its high costs and scarcity.
3. Study of various techniques instead of sol gel-like RF magnetron sputtering to ease or control the growth of thin films thickness on natural fibre surfaces. Furthermore, a high rate of sputter coating of substrates can ensure large area and competitive costs. Care must be taken to avoid fibre damage during the deposition process.
4. Mechanical and physical properties of a natural fibre coated with TCOs should be investigated since there is a significant change especially after deposition process and thermal decomposition.

6.3.2 Tubular TiO_2

1. The pH value of the TiO_2 prepared solution affects the formation of TiO_2 crystal structure, shape, size, and surface area. Therefore, the pH value needs further attention since the structured forms of TiO_2 directly affected the photocatalytic activities.

2. To produce a homogeneous size of the tubular TiO_2, the natural fibre used as a sacrificial template should be in the same range size of diameter.
3. Exposing of a different wavelength of UV light during the photocatalyst could be considered for an extension of the study. The different wavelength gives different photocatalytic performance or activities for TiO_2.

References

Akil, H., Omar, M.F., Mazuki, A.A.M., Safiee, S.Z.A.M., Ishak, Z.M. and Bakar, A.A., 2011. Kenaf fibre reinforced composites: A review. *Materials & Design, 32*(8-9), 4107-4121.

Aji, I.S., Sapuan, S.M., Zainudin, E.S. and Abdan, K., 2009. Kenaf fibres as reinforcement for polymeric composites: a review. *International Journal of Mechanical and Materials Engineering, 4*(3), 239-248.

Akpan, U.G. and Hameed, B.H., 2009. Parameters affecting the photocatalytic degradation of dyes using TiO_2-based photocatalysts: a review. *Journal of Hazardous Materials, 170*(2-3), 520-529.

Ashori, A., Harun, J., Raverty, W.D. and Yusoff, M.N.M., 2006. Chemical and morphological characteristics of Malaysian cultivated kenaf (Hibiscus cannabinus) fibre. *Polymer-Plastics Technology and Engineering, 45*(1), 131-134.

Aziz, S.H. and Ansell, M.P., 2004. The effect of alkalization and fibre alignment on the mechanical and thermal properties of kenaf and hemp bast fibre composites: Part 1 – polyester resin matrix. *Composite Science and Technology, 64*, 1219–1230.

Aziz, S.H. Ansell, M.P., Clarke S.J. and Panteny S. R., 2005. Modified polyester resins for natural fibre composites. *Composite Science and Technology, 65*, 525-535.

Ba-Abbad, M.M., Kadhum, A.A.H., Mohamad, A.B., Takriff, M.S. and Sopian, K., 2012. Synthesis and catalytic activity of TiO_2 nanoparticles for photochemical oxidation of concentrated chlorophenols under direct solar radiation. *International Journal of Electrochemical Science*,7, 4871–4888.

Babatunde, O.E., Yatim, J.M., Ishak, M.Y., Masoud, R. and Meisam, R., 2015. Potentials of kenaf fibre in bio-composite production: a review. *Cellulose, 1*, 22.

Bagheri, S., Shameli, K. and Sharifah, B.A.H., 2013. Synthesis and characterization of anatase titanium dioxide nanoparticles using egg white solution via sol-gel method. *Journal of Chemistry* 2, 1–5.

Barakat, M.A., Schaeffer, H., Hayes, G. and Ismat-Shah, S., 2005. Photocatalytic degradation of 2-chlorophenol by Co-doped TiO_2 nanoparticles. *Apply Catalyst B*, 57, 23–30.

Barquinha, P., Goncalves, G., Pereira, L., Martins, R. and Fortunato, E., 2007. Effect of annealing temperature on the properties of IZO films and IZO based transparent TFTs. *Thin Solid Films*, *515*(24), 8450-8454.

Batzill, M., 2011. Fundamental aspects of surface engineering of transition metal oxide photocatalysts. *Energy & Environmental Science*, *4*(9), 3275-3286.

Behnajady, M.A., Eskandarloo, H., Modirshahla, N. and Shokri, M., 2011. Investigation of the effect of sol–gel synthesis variables on structural and photocatalytic properties of TiO_2 nanoparticles. *Desalination*, 278, 10–17.

Bessekhouad, Y., Robert, D. and Weber, J.V., 2003. Synthesis of photocatalytic TiO_2 nanoparticles: optimization of the preparation conditions. *Journal of Photochemistry and Photobiology A: Chemistry*, *157*(1), 47-53.

Biancardo, M., Argazzi, R. and Bignozzi, C.A., 2005. Solid-state photochromic device based on nanocrystalline TiO_2 functionalized with electron donor−acceptor species. *Inorganic chemistry*, *44*(26), 9619-9621.

Binas, V., Venieric, D., Kotziasd, D. and Kiriakidisa, G., 2017. Modified TiO_2 based photocatalysts for improved air and health quality. *Journal of Materiomics*, 3, 3–16.

Biswal, R., Maldonado, A., Vega-Pérez, J., Acosta, D.R. and De La Luz Olvera, M., 2014. Indium doped zinc oxide thin films deposited by ultrasonic chemical spray technique, starting from zinc acetylacetonate and indium chloride. *Materials*, *7*(7), 5038-5046.

Bozzi, A., Yuranova T., Guasaquillo I. , Laub D., and Kiwi J., 2005. Self-cleaning of modified cotton textiles by TiO_2 at low temperatures under daylight irradiation, *Chemistry*, vol. 174, 156–164.

Brinker, C.J., 2004. Evaporation-induced self-assembly: functional nanostructures made easy. *MRS bulletin*, *29*(9), 631-640.

Castillo-Ledezma, J.H., Salas, J.S., López-Malo, A. and Bandala, E.R., 2011. Effect of pH, solar irradiation, and semiconductor concentration on the photocatalytic disinfection of Escherichia coli in water using nitrogen-doped TiO_2. *European Food Research and Technology*, *233*(5), 825.

Cernuto, G., Masciocchi, N., Cervellino, A., Colonna, G.M. and Guagliardi, A., 2011. Size and shape dependence of the photocatalytic activity of TiO_2 nanocrystals: a total scattering Debye function study. *Journal of the American Chemical Society*, *133*(9), 3114-3119.

Chatterjee, D. and Dasgupta, S., 2005. Visible light induced photocatalytic degradation of organic pollutants. *Journal of Photochemistry and Photobiology C: Photochemistry Reviews*, *6*(2-3), 186-205.

Chen, X. and Mao, S.S., 2007. Titanium dioxide nanomaterials: synthesis, properties, modifications, and applications. *Chemical Review,* 107, 2891–2959.

Cheung, H.Y., Ho, M.P., Lau, K.T., Cardona, F. and Hui, D., 2009. Natural fibre-reinforced composites for bioengineering and environmental engineering applications. *Composites Part B: Engineering*, *40*(7), 655-663.

Chong, M.N., Jin, B., Chow, C.W. and Saint, C., 2010. Recent developments in photocatalytic water treatment technology: a review. *Water Research*, *44*(10), 2997-3027.

Clatot, J., Campet, G., Zeinert, A., Labrugère, C., Nistor, M. and Rougier, A., 2011. Low temperature Si doped ZnO thin films for transparent conducting oxides. *Solar Energy Materials and Solar Cells*, *95*(8), 2357-2362.

Craciun, V., Martin, C., Socol, G., Tanner, D., Swart, H.C., Becherescu, N. and Craciun, D., 2014. Optical properties of amorphous indium zinc oxide thin films synthesized by pulsed laser deposition. *Applied Surface Science*, *306*, 52-55.

Dagade P.C. and Shaikh S. M, 2015. Fabrication of Composite Materials by using Short Pineapple Leaf Fibre (PALF), *IJIERT*.

Davoodi, M.M., Sapuan, S.M., Ahmad, D., Ali, A., Khalina, A. and Jonoobi, M., 2010. Mechanical properties of hybrid kenaf/glass reinforced epoxy composite for passenger car bumper beam. *Materials & Design*, *31*(10), 4927-4932.

Dehuff, N.L., Kettenring, E.S., Hong, D., Chiang, H.Q., Wager, J.F., Hoffman, R.L., Park, C.H. and Keszler, D.A., 2005. Transparent thin-film transistors with zinc indium oxide channel layer. *Journal of Applied Physics*, *97*(6), 064505.

Diebold, U., 2003. The surface science of titanium dioxide. *Surface Science Reports*, *48*(5-8), 53-229.

Do-Hoon, S.H.I.N., Yun-Hae, K.I.M., Joong-Won, H.A.N., Kyung-Man, M.O.O.N. and Murakami, R.I., 2009. Effect of process parameters on electrical, optical properties of IZO films produced by inclination opposite target type DC magnetron sputtering. *Transactions of Nonferrous Metals Society of China*, *19*(4), 997-1000.

Edeerozey, A.M., Akil, H.M., Azhar, A.B. and Ariffin, M.Z., 2007. Chemical modification of kenaf fibres. *Materials Letters*, *61*(10), 2023-2025.

Eichhorn, S.J., Baillie, C.A., Zafeiropoulos, N., Mwaikambo, L.Y., Ansell, M.P., Dufresne, A., Entwistle, K.M., Herrera-Franco, P.J., Escamilla, G.C., Groom, L. and Hughes, M., 2001. Current international research into cellulosic fibres and composites. *Journal of Materials Science*, *36*(9), 2107-2131.

Ellmer, K., 2012. Past achievements and future challenges in the development of optically transparent electrodes, *Nature Photonics*, vol. 6, 12, 809-817.

Elsaid, A., Dawood, M., Seracino, R. and Bobko, C., 2011. Mechanical properties of kenaf fibre reinforced concrete. *Construction and Building Materials*, *25*(4), 1991-2001.

El Yamny, S. and Rafea, M.A., 2012. Preparation and characterization of ZnO: In transparent conductor by low cost dip coating technique. *Journal of Modern Physics*, *3*(09), 1060-1069.

Fujishima, A., Zhang, X. and Tryk, D.A., 2008. TiO_2 photocatalysis and related surface phenomena. *Surface Science Reports*, *63*(12), 515-582.

Gassan, J. and Bledzki, A.K, 1999. Possibilities for improving the mechanical properties of jute epoxy composites by alkali treatment of fibres. *Composites Science Technol*ogy, 59, 1303-1309.

Ghosh, P.K., Jana, S., Nandy, S. and Chattopadhyay, K.K., 2007. Size-dependent optical and dielectric properties of nanocrystalline ZnS thin films synthesized via rf-magnetron sputtering technique. *Materials Research Bulletin*, *42*(3), 505-514.

Giocondi, J.L., Salvador, P.A. and Rohrer, G.S., 2007. The origin of photochemical anisotropy in $SrTiO_3$. *Topics in Catalysis*, *44*(4), 529-533.

Gnanasekaran, L., Hemamalini, R. and Ravichandran, K., 2015. Synthesis and characterization of TiO_2 quantum dots for photocatalytic application. *Journal of Saudi Chemical Society*, *19*(5), 589-594.

Granqvist, C.G., 2003. Solar energy materials. *Advanced Materials*, *15*(21), 1789-1803.

Grätzel, M., 2004. Conversion of sunlight to electric power by nanocrystalline dye-sensitized solar cells. *Journal of Photochemistry and Photobiology A: Chemistry*, *164*(1-3), 3-14.

Gupta, S.M. and Tripathi, M., 2011. A review of TiO_2 nanoparticles. *Chinese Science Bulletin*, *56*(16), 1639.

Hagen, J., 2015. *Industrial Catalysis: A Practical Approach*. John Wiley & Sons.

Han, G., Lei, Y., Wu, Q., Kojima, Y. and Suzuki, S., 2008. Bamboo–fibre filled high density polyethylene composites: effect of coupling treatment and nanoclay. *Journal of Polymers and the Environment*, *16*(2), 123-130.

Han, G., Wang, L., Pei, C., Shi, R., Liu, B., Zhao, H., Yang, H. and Liu, S., 2014. Size-dependent optical properties and enhanced visible light photocatalytic activity of wurtzite CdSe hexagonal nanoflakes with dominant {0 0 1} facets. *Journal of Alloys and Compounds*, *610*, 62-68.

Haniffah, W.H., Sapuan, S.M., Abdan, K., Khalid, M., Hasan, M. and Hoque, M.E., 2015. Kenaf fibre reinforced polypropylene composites: effect of cyclic immersion on tensile properties. *International Journal of Polymer Science*, *2015*.

Hao, X., Ma, J., Zhang, D., Yang, Y., Xu, X., Chen, F. and Ma, H., 2002. Electrical and optical properties of SnO_2: Sb films prepared on polyimide substrate by rf bias sputtering. *Applied Surface Science*, *189*(1-2), 157-161.

Holbery, J. and Houston, D., 2006. Natural-fibre-reinforced polymer composites in automotive applications. *Jom*, *58*(11), 80-86.

Hwang, D.K., Moon, J.H., Shul, Y.G., Jung, K.T., Kim, D.H. and Lee, D.W., 2003. Scratch resistant and transparent UV-protective coating on polycarbonate. *Journal of Sol-Gel Science and Technology*, *26*(1-3), 783-787.

Ibhadon, A.O. and Fitzpatrick, P., 2013. Heterogeneous photocatalysis: recent advances and applications. *Catalysts*, *3*(1), 189-218.

Ibrahim, I.D., Jamiru, T., Sadiku, E.R., Kupolati, W.K. and Agwuncha, S.C., 2016. Impact of surface modification and nanoparticle on sisal fibre reinforced polypropylene nanocomposites. *Journal of Nanotechnology*, *2016*.

Ishak, M. R., Sapuan, S. M., Leman, Z., Rahman, M. Z. A. and Anwar, U. M. K., 2012. Characterization of sugar palm (Arenga pinnata) fibres. *Journal of Thermal Analysis Calorimetry*, 109, 981–989.

Jeon, J.W., Jeon, D.W., Sahoo, T., Kim, M., Baek, J.H., Hoffman, J.L., Kim, N.S. and Lee, I.H., 2011. Effect of annealing temperature on optical band-gap of amorphous indium zinc oxide film. *Journal of Alloys and Compounds*, *509*(41), 10062-10065.

Juliana, A.H., Paridah, M.T., Rahim, S., Azowa, I.N. and Anwar, U.M.K., 2012. Properties of particleboard made from kenaf (Hibiscus cannabinus L.) as function of particle geometry. *Materials & Design*, *34*, 406-411.

Kawahara, K., Suzuki, K., Ohko, Y. and Tatsuma, T., 2005. Electron transport in silver-semiconductor nanocomposite films exhibiting multicolor photochromism. *Physical Chemistry Chemical Physics*, *7*(22), 3851-3855.

Kazeminezhad, I. and Sadollahkhani, A., 2016. Influence of pH on the photocatalytic activity of ZnO nanoparticles. *Journal of Materials Science: Materials in Electronics*, *27*(5), 4206-4215.

Keshavarzi, R., Mirkhani, V., Moghadam, M., Tangestaninejad, S., Mohammadpoor-Baltork, I., Fallah, H.R., Dastjerdi, M.J.V. and Modayemzadeh, H.R., 2011. Preparation and characterization of indium zinc oxide thin films by electron beam evaporation technique. *Materials Research Bulletin*, *46*(4), 615-620.

Kiriakidou, F., Kondarides, D.I. and Verykios, X.E., 1999. The effect of operational parameters and TiO_2-doping on the photocatalytic degradation of azo-dyes. *Catalysis Today*, *54*(1), 119-130.

Khalil, H.A., Yusra, A.I., Bhat, A.H. and Jawaid, M., 2010. Cell wall ultrastructure, anatomy, lignin distribution, and chemical composition of Malaysian cultivated kenaf fibre. *Industrial Crops and Products*, *31*(1), 113-121.

Khan, M.M., Adil, S.F. and Al-Mayouf, A., 2015. Metal oxides as photocatalysts. *Journal of Saudi Chemical Society*, *19* (5), 462–464.

Khan, M.M., Ansari, S.A., Pradhan, D., Ansari, M.O., Lee, J. and Cho, M.H., 2014. Band gap engineered TiO_2 nanoparticles for visible light induced photoelectrochemical and photocatalytic studies. *Journal of Materials Chemistry A*, *2*(3), 637-644.

Kim, H.M., Jung, S.K., Ahn, J.S., Kang, Y.J. and Je, K.C., 2003. Electrical and optical properties of In_2O_3–ZnO films deposited on polyethylene terephthalate substrates by radio frequency magnetron sputtering. *Japanese Journal of Applied Physics*, *42*(1R), 223.

Kim, H., Pique, A., Horwitz, J.S., Mattoussi, H., Murata, H., Kafafi, Z.H. and Chrisey, D.B., 1999. Indium tin oxide thin films for organic light-emitting devices. *Applied Physics Letters*, *74*(23), 3444-3446.

Kim, K., Park, S.Y., Lim, K.H., Shin, C., Myoung, J.M. and Kim, Y.S., 2012. Low temperature and solution-processed Na-doped zinc oxide transparent thin film transistors with reliable electrical performance using methanol developing and surface engineering. *Journal of Materials Chemistry*, *22*(43), 23120-23128.

Kim, S.M., Choi, H.W., Kim, K.H., Park, S.J. and Yoon, H.H., 2009. Preparation of ITO and IZO thin films by using the facing targets sputtering (FTS) method. *Journal of Korean Physic Society*, *55*(5), 1996-2001.

Krishnaprasad, R., Veena, N.R., Maria, H.J., Rajan, R., Skrifvars, M. and Joseph, K., 2009. Mechanical and thermal properties of bamboo microfibril reinforced polyhydroxybutyrate biocomposites. *Journal of Polymers and the Environment*, *17*(2), 109.

Kuo, C.C., Liu, C.C., He, S.C., Chang, J.T. and He, J.L., 2011. The influences of thickness on the optical and electrical properties of dual-ion-beam sputtering-deposited molybdenum-doped zinc oxide layer. *Journal of Nanomaterials*, *2011*, 60.

Lee, J., 2008. Effects of oxygen concentration on the properties of sputtered SnO_2: Sb films deposited at low temperature. *Thin Solid Films*, *516*(7), 1386-1390.

Lee, J.-H. and Park, B.-O., 2003. Transparent conducting ZnO:Al, In and Sn thin films deposited by the sol-gel method. *Thin Solid Films*, 426, 94–99.

Lee, S.H., Lee, S.Y. and Park, B.O., 2012. Effect of annealing temperature on amorphous indium zinc oxide thin films prepared by a sol-gel spin-coating method. *Journal of the Korean Crystal Growth and Crystal Technology*, *22*(1), 15-18.

Lee, S.H., Lee, S.Y. and Park, B.O., 2012. Effect of annealing temperature on amorphous indium zinc oxide thin films prepared by a sol-gel spin-coating method. *Journal of the Korean Crystal Growth and Crystal Technology*, *22*(1), 15-18.

Li, B., Wang, X., Yan, M. and Li, L., 2003. Preparation and characterization of nano-TiO_2 powder. *Materials Chemistry and Physic*, 78, 184–188.

Li, W., Ni, C., Lin, H., Huang, C.P. and Ismat, S.S., 2004. Size dependence of thermal stability of TiO_2 nanoparticles. *Journal of Applied Physic*, 96, 6663–6668.

Liu, L., Zhao, H., Andino, J.M. and Li, Y., 2012. Photocatalytic CO_2 reduction with H_2O on TiO_2 nanocrystals: Comparison of anatase, rutile, and brookite polymorphs and exploration of surface chemistry. *ACS Catalysis*, *2*(8), 1817-1828.

Liu, S.M., Gan, L.M., Liu, L.H., Zhang, W.D. and Zeng, H.C., 2002. Synthesis of single-crystalline TiO_2 nanotubes. *Chemistry of Materials, 14*(3), 1391-1397.

Liu, Y., Goebl, J. and Yin, Y., 2013. Templated synthesis of nanostructured materials. *Chemical Society Reiews,* 42, 2610–2653.

Liu, Y., Li, Y. and Zeng, H., 2013a. ZnO-based transparent conductive thin films: doping, performance, and processing. *Journal of Nanomaterials, 2013*.

Luttrell, T., Halpegamage, S., Tao, J., Kramer, A., Sutter, E. and Batzill, M., 2014. Why is anatase a better photocatalyst than rutile?–Model studies on epitaxial TiO_2 films. *Scientific Reports*, 4, 4043.

Macwan, D.P., Dave, P.N. and Chaturvedi, S., 2011. A review on nano-TiO_2 sol–gel type syntheses and its applications. *Journal of Material Science,* 46, 3669–3686.

Mahltig, B., Böttcher, H., Rauch, K., Dieckmann, U., Nitsche, R. and Fritz, T., 2005. Optimized UV protecting coatings by combination of organic and inorganic UV absorbers. *Thin Solid Films*, *485*(1-2), 108-114.

Mahshid, S., Askari, M., and Ghamsari, M.S., 2007. Synthesis of TiO_2 nanoparticles by hydrolysis and peptization of titanium isopropoxide solution. *Journal of Materials Processing Technology,* 189, 296–300.

Malato, S., Fernández-Ibáñez, P., Maldonado, M.I., Blanco, J. and Gernjak, W., 2009. Decontamination and disinfection of water by solar photocatalysis: recent overview and trends. *Catalysis Today*, *147*(1), 1-59.

Matsubara, K., Tampo, H., Shibata, H., Yamada, A., Fons, P., Iwata, K. and Niki, S., 2004. Band-gap modified Al-doped Zn 1− x Mg x O transparent conducting films deposited by pulsed laser deposition. *Applied Physics Letters*, *85*(8), 1374-1376.

Mazuki, A.A.M., Akil, H.M., Safiee, S., Ishak, Z.A.M. and Bakar, A.A., 2011. Degradation of dynamic mechanical properties of pultruded kenaf fibre reinforced composites after immersion in various solutions. *Composites Part B: Engineering*, *42*(1), 71-76.

Meng, L.J. and Dos Santos, M.P., 1997. Properties of indium tin oxide (ITO) films prepared by rf reactive magnetron sputtering at different pressures. *Thin Solid Films*, *303*(1-2), 151-155.

Miao, L., Tanemura, S., Toh, S., Kaneko, K. and Tanemura, M., 2004. Fabrication, characterization and Raman study of anatase-TiO2 nanorods by a heating-sol–gel template process. *Journal of Crystal Growth*, *264*(1-3), 246-252.

Mills, A., 2012. An overview of the methylene blue ISO test for assessing the activities of photocatalytic films. *Applied Catalysis B: Environmental*, *128*, 144-149.

Mohanty, A.K., Khan, M.A. and Hinrichsen, G., 2000. Surface modification of jute and its influence on performance of biodegradable jute-fabric/Biopol composites. *Composites Science Technology*, 60, 1115 – 1124.

Mohanty, A.K., Misra, M. and Drzal, L.T., 2001. Surface modifications of natural fibres and performance of the resulting biocomposites: an overview. *Composite Interfaces*, *8*(5), 313-343.

Mohanty, A.K., Misra, M. and Drzal, L.T. eds., 2005. Natural fibres, biopolymers, and biocomposites. *CRC press*.

Mossello, A.A., Harun, J., Tahir, P.M., Resalati, H., Ibrahim, R., Shamsi, S.R.F. and Mohmamed, A.Z., 2010. A review of literatures related of using kenaf for pulp production (beating, fractionation, and recycled fibre). *Modern Applied Science*, *4*(9), 21.

Nakata, K. and Fujishima, A., 2012. TiO_2 photocatalysis: Design and applications. *Journal of Photochemistry and Photobiology C: Photochemistry Reviews*, *13*(3), 169-189.

Namvar, F., Jawaid, M., Tahir, P.M., Mohamad, R., Azizi, S. and Khodavandi, A., 2014. Potential use of plant fibres and their composites for biomedical applications. *BioResources*, 9, 5688–5706.

Neppolian, B., Jung, H. and Choi, H., 2007. Photocatalytic degradation of 4-chlorophenol using TiO_2 and Pt-TiO_2 nanoparticles prepared by sol-gel method. *Journal of Advanced Oxidation Technologies*, 10, 369–374.

Neppolian, B., Choi, H.C., Sakthivel, S., Arabindoo, B. and Murugesan, V., 2002. Solar light induced and TiO_2 assisted degradation of textile dye reactive blue 4. *Chemosphere*, *46*(8), 1173-1181.

Nishino, T., Hirao, K., Kotera, M., Nakamae, K. and Inagaki, H., 2003. Kenaf reinforced biodegradable composite. *Composites Science and Technology*, *63*(9), 1281-1286.

Ohno, T., Sarukawa, K., Tokieda, K. and Matsumura, M., 2001. Morphology of a TiO_2 photocatalyst (Degussa, P-25) consisting of anatase and rutile crystalline phases. *Journal of Catalysis*, *203*(1), 82-86.

Ortiz, A., Sanchez, A., Falcony, C., Farias, M.H., Hirata, G.A. and Cota-Araiza, L., 1988. Lack of chemical interaction of hydrogenated amorphous silicon with indium-doped zinc oxide transparent conductive films. *Journal of Non-Crystalline Solids*, *103*(1), 9-13.

Oskam, G., Nellore, A., Lee, P.R. and Searson, P.C., 2003. The growth kinetics of TiO_2 nanoparticles from titanium (IV) alkoxide at high water/titanium ration. *Journal of Physic Chemistry. B.* 107, 1734–1738.

Pang, C., Shanks, R.A. and Daver, F., 2015. Characterization of kenaf fibre composites prepared with tributyl citrate plasticized cellulose acetate. *Composites Part A: Applied Science and Manufacturing*, *70*, 52-58.

Patil, P.S., 1999. Versatility of chemical spray pyrolysis technique. *Materials Chemistry and Physics*, *59*(3), 185-198.

Rajeshwar, K., Osugi, M.E., Chanmanee, W., Chenthamarakshan, C.R., Zanoni, M.V.B., Kajitvichyanukul, P. and Krishnan-Ayer, R., 2008. Heterogeneous photocatalytic treatment of organic dyes in air and aqueous media. *Journal of Photochemistry and Photobiology C: Photochemistry Reviews*, *9*(4), 171-192.

Raman, B. V. R, Vijaya, R.B. and Manoharan, N. 2015. Kenaf fibre reinforced composites: A review. *ARPN Journal of Engineering and Applied Sciences*, vol. 10 (13), 5483-5484.

Ramesh, M., 2016. Kenaf (Hibiscus cannabinus L.) fibre based bio-materials: A review on processing and properties. *Progress in Materials Science*, 78–79, 1–92.

Rao, T.P. and Santhoshkumar, M.C., 2009. Effect of thickness on structural, optical and electrical properties of nanostructured ZnO thin films by spray pyrolysis. *Applied Surface Science*, *255*(8), 4579-4584.

Ray, D., Sarkar, B.K., Das, S. and Rana, A.K., 2002. Dynamic mechanical and thermal analysis of vinylester-resin-matrix composites reinforced with untreated and alkali-treated jute fibres. *Composites Science Technology*. 62, 911–917.

Rehman, S., Ullah, R., Butt, A.M. and Gohar, N.D., 2009. Strategies of making TiO2 and ZnO visible light active. *Journal of Hazardous Materials*, *170*(2-3), 560-569.

Reza, K.M., Kurny, A.S.W. and Gulshan, F., 2017. Parameters affecting the photocatalytic degradation of dyes using TiO_2: a review. *Applied Water Science*, *7*(4), 1569-1578.

Rezaee Roknabadi, M., Behdani, M., Arabshahi, H. and Hodeini, N., 2009. Indium-doped zinc oxide thin films by sol–gel method. *International Review of Physics, 12*.

Rusop, M., 2012. Effect of film thickness on structural, electrical, and optical properties of sol-gel deposited layer-by-layer ZnO nanoparticles. *Transactions on Electrical and Electronic Materials*, *13*(2), 102-105.

Saravanan, R., Gracia, F. and Stephen, A., 2017. Basic Principles, Mechanism, and Challenges of Photocatalysis. In *Nanocomposites for Visible Light-induced Photocatalysis* (19-40). Springer, Cham.

Saravanan, R., Gupta, V.K., Narayanan, V. and Stephen, A., 2013. Comparative study on photocatalytic activity of ZnO prepared by different methods. *Journal of Molecular Liquids*, *181*, 133-141.

Saravanan, R., Shankar, H., Rajasudha, G., Stephen, A. and Narayanan, V., 2011. Photocatalytic degradation of organic dye using nano ZnO. *International Journal of Nanoscience*, *10*, 253-257.

Scanlon, D.O., Dunnill, C.W., Buckeridge, J., Shevlin, S.A., Logsdail, A.J., Woodley, S.M., Catlow, C.R.A., Powell, M.J., Palgrave, R.G., Parkin, I.P. and Watson, G.W., 2013. Band alignment of rutile and anatase TiO_2. *Nature Materials*, *12*(9), 798.

Schneller, T., Waser, R., Kosec, M. and Payne, D. eds., 2013. *Chemical solution deposition of functional oxide thin films* (233-261). London: Springer.

Seng, N. K., Ahmad, M. K., Jasmin, N. S., Zainal, N., Nayan, N., Fhong, S. C., Suriani, A. B. and Mohamed, A., 2016. Effect of annealing time on aluminium doped tin oxide (SnO_2) as a transparent conductive oxide, *ARPN Journal of Engineering and Applied Sciences.* vol. 11, 14.

Setvín, M., Aschauer, U., Scheiber, P., Li, Y.F., Hou, W., Schmid, M., Selloni, A. and Diebold, U., 2013. Reaction of O_2 with subsurface oxygen vacancies on TiO_2 anatase (101). *Science*, *341*(6149), 988-991.

Sgriccia, N., Hawley, M.C. and Misra, M., 2008. Characterization of natural fibre surfaces and natural fibre composites. *Composites Part A: Applied Science and Manufacturing 39 (10)*, 1632–1637.

Si, S.H., Fung, Y.S. and Zhu, D.R., 2005. Improvement of piezoelectric crystal sensor for the detection of organic vapors using nanocrystalline TiO_2 films. *Sensors and Actuators B: Chemical*, *108*(1-2), 165-171.

Sing, K.S.W., 1985. Reporting physisorption data for gas/solid systems with special reference to the determination of surface area and porosity. *Pure and Applied Chemistry*, 57, 603–619.

Sirghi, L., Aoki, T. and Hatanaka, Y., 2003. Friction force microscopy study of the hydrophilicity of TiO_2 thin films deposited by radio frequency magnetron sputtering. *Surface Review and Letters*, 10, 345-349

Song, P.K., Shigesato, Y., Kamei, M. and Yasui, I., 1999. Electrical and structural properties of tin-doped indium oxide films deposited by DC sputtering at room temperature. *Japanese Journal of Applied Physics*, 38, p.2921.

Sreekala, M.S., Kumaran, M.G. and Thomas, S., 1997. Oil palm fibres: Morphology, chemical composition, surface modification, and mechanical properties. *Journal of Applied Polymer Science*, *66*(5), 821-835.

Sugimoto, T., Zhou, X. and Muramatsu, A., 2003. Synthesis of uniform anatase TiO_2 nanoparticles by gel–sol method: 4. Shape control. *Journal of Colloid and Interface Science*, *259*(1), 53-61.

Sun, X., Liu, H., Dong, J., Wei, J. and Zhang, Y., 2010. Preparation and characterization of Ce/N-Codoped TiO_2 particles for production of H_2 by photocatalytic splitting water under visible light. *Catalyst Letters,* 135, 219–225.

Sydenstricker, T.H., Mochnaz, S. and Amico, S.C., 2003. Pull-out and other evaluations in sisal-reinforced polyester biocomposites. *Polymer Testing*, *22*(4), 375-380.

Takata, Y., Hidaka, S., Masuda, M. and Ito, T., 2003. Pool boiling on a superhydrophilic surface. *International Journal of Energy Research*, *27*(2), 111-119.

Tao, J. and Batzill, M., 2010. Role of surface structure on the charge trapping in TiO_2 photocatalysts. *The Journal of Physical Chemistry Letters*, *1*(21), 3200-3206.

Tao, J., Luttrell, T. and Batzill, M., 2011. A two-dimensional phase of TiO_2 with a reduced bandgap. *Nature Chemistry*, *3*(4), 296.

Thamarai S. P., Venkatachalam M., Saroja M., Gowthaman P., Ravikumar S. and Shankar S., 2014. Influence of Growth Time on Zinc Oxide Nano Rods Prepared by Dip Coating Method. *International Journal of Innovative Research Science, Engineering and Technology*, vol. 3, 16350-16354.

Toriz, G., Denes, F. and Young, R.A., 2002. Lignin-polypropylene composites. Part 1: Composites from unmodified lignin and polypropylene. *Polymer Composites*, *23*(5), 806-813.

Wang, X. and Caruso, R.A., 2011. Enhancing photocatalytic activity of titania materials by using porous structures and the addition of old nanoparticles. *Journal of Material Chemistry*. 21, 20–28.

Webber III, C.L. and Bledsoe, V.K., 2002. Kenaf yield components and plant composition. *Trends in New Crops and New Uses*, 348-357.

Wielage, B., Lampke, T., Marx, G., Nestler, K. and Starke, D., 1999. Thermogravimetric and differential scanning calorimetric analysis of natural fibres and polypropylene. *Thermochimica Acta*, 337, 169.

Xia, C., Shi, S.Q., Wu, Y. and Cai L., 2016. High pressure-assisted magnesium carbonate impregnated natural fibre-reinforced composites. *Industrial Crops and Products.* 86, 16-22.

Xu, M., Gao, Y., Moreno, E.M., Kunst, M., Muhler, M., Wang, Y., Idriss, H. and Wöll, C., 2011. Photocatalytic activity of bulk TiO_2 anatase and rutile single crystals using infrared absorption spectroscopy. *Physical Review Letters*, *106*(13).

Xu, X. and Asher, S.A., 2004. Synthesis and utilization of monodisperse hollow polymeric particles in photonic crystals. *Journal of the American Chemical Society*, *126*(25), 7940-7945.

Yang, H., Yan, R., Chen, H., Lee, D.H. and Zheng, C., 2007. Characteristics of hemicellulose, cellulose and lignin pyrolysis. *Fuel*, *86*(12-13), 1781-1788.

Yue, L., Pu, H., Li, H., Pang, S. and Zhang, Q., 2013. Dip-coated Al–In–Zn–O thin-film transistor with poly-methylmethacrylate gate dielectric. *Journal of Physics D: Applied Physics*, *46*(44).

Zhang, M.Y. and Cheng, G.J., 2011. Highly conductive and transparent alumina-doped ZnO films processed by direct pulsed laser recrystallization at room temperature. *Applied Physics Letters*, *99*(5).

Zhang, M.Y., Nian, Q. and Cheng, G.J., 2012. Room temperature deposition of alumina-doped zinc oxide on flexible substrates by direct pulsed laser recrystallization. *Applied Physics Letters*, *100*(15).

Zhu, K., Yang, Y., Wei, T., Tan, R., Cui, P., Song, W. and Choy, K.L., 2013. Room temperature DC magnetron sputtering deposition of hydrogenated aluminum doped zinc oxide thin films on polyethylene terephthalate substrates. *Materials Letters*, *106*, 363-365.